UNIVERSITY OF PARDUBICE

Faculty of Chemical Technology
Department of Inorganic Technology

J. Heyrovský Institute of Physical Chemistry of the CAS, v. v. i.
Departmet of Structure and Dynamics in Catalysis

Development of structured zeolitic catalysts for the process of hydroisomerization of *n*-hexane

Ing. Jana Pastvová

DOCTORAL THESIS
2018

Prohlašuji:

Tuto práci jsem vypracovala samostatně. Veškeré literární prameny a informace, které jsem v práci využila, jsou uvedeny v seznamu použité literatury.

Byla jsem seznámena s tím, že se na moji práci vztahují práva a povinnosti vyplývající ze zákona č. 121/2000 Sb., autorský zákon, zejména se skutečností, že Univerzita Pardubice má právo na uzavření licenční smlouvy o užití této práce jako školního díla podle § 60 odst. 1 autorského zákona, a s tím, že pokud dojde k užití této práce mnou nebo bude poskytnuta licence o užití jinému subjektu, je Univerzita Pardubice oprávněna ode mne požadovat přiměřený příspěvek na úhradu nákladů, které na vytvoření díla vynaložila, a to podle okolností až do jejich skutečné výše.

Souhlasím s prezenčním zpřístupněním své práce v Univerzitní knihovně.

V Praze dne 26. 11. 2018

Ing. Jana Pastvová

Poděkování:

Ráda bych poděkovala **Ing. Petrovi Sazamovi, Ph.D.** za jeho velkou pomoc, konzultaci a cenné rady při řešení experimentálních problémů, za jeho kladný přístup a vedení v průběhu mého doktorského studia, a za pomoc při publikační činnosti i se zpracováním mé dizertační práce.
Rovněž bych chtěla poděkovat celému kolektivu Oddělení struktury a dynamiky v katalýze ústavu J. Heyrovského AV ČR, zejména Ing. Galině Sádovské, Ph. D., Ing. Jaroslavě Morávkové, Ph.D., Ing. Aleně Vondrové a také Ing. Radimovi Pilařovi, Ph.D., kteří se vždy postarali o příjemnou a zábavnou atmosféru, a díky kterým se člověk rád vracel zpět do práce.
Své velké poděkovaní bych chtěla věnovat i své rodině, zejména tatínkovi, který mě přivedl k myšlence nad doktorským studiem uvažovat, a pak svému manželovi, jenž mě svým rýpavým způsobem dokázal naštvat a vyburcovat tak k mým nejlepším výkonům.

Všem moc ze srdce děkuji.

ANNOTATION

The hydroisomerization of linear or low branched alkanes through alkene intermediates is a significant process for the refining of C_5 and C_6 hydrocarbon fractions to increase the octane number of automotive fuels. The hydroisomerization leads to the conversion of linear alkanes with a low octane number to branched isomers with a sufficiently high octane number. The bifunctional heterogeneous catalysts are a combination of an acid catalyst consisting of oxides containing acidic active centers and a metal cluster, where the hydrogenation and dehydrogenation of hydrocarbon reactants take place. The zeolite-based catalysts are significant in petroleum industry for the hydroisomerization of alkanes, especially the MOR zeolite type. However, availability of active sites for the *n*-hexane molecule is restricted by slow diffusion in narrow channels of MOR zeolite, and overall efficiency of the catalytic process is thus limited by transport of molecules. Branched alkanes diffuse even more slowly than linear *n*-alkanes due to the higher kinetic diameter. The access of acidic active sites in current industrial catalysts is typically increased by partial dealumination of zeolites, where the aluminum atoms are extracted from the framework of zeolite resulting in positive textural changes in the channel structure of the zeolite but at the same time lowering the concentration of active acidic Brønsted centers. For these reasons, various post-synthesis methods of zeolites such as desilication, dealumination and fluoridation have been used in this work. The texture parameters of zeolites are adjusted by combination of these methods and allow easier transport of the hydrocarbon molecules to the active sites, therefore achieving a substantial increase in the rate of hydroisomerization reaction and shifting the reaction conditions to lower temperatures where the thermodynamic equilibrium is inclined to forming of multi-branched alkanes. Another important parameter for the hydroisomerization of C_6 is the amount of acidic centers contained in the zeolites. The analysis of the role of increased density of strongly acidic protons showed that the high density of non-interacting but close and strongly acidic structural hydroxylgroups significantly lowers the activation barrier in the isomerization reaction compared to far-distant acid sites and provides higher reaction rates compared to state-of-the-art Pt/H-zeolite catalysts.

KEYWORDS

hydroisomerization, *n*-hexane, dealumination, desilication, fluorination, shape selectivity, mordenite (MOR), beta zeolite (*BEA), hierarchical zeolite

NÁZEV PRÁCE

Vývoj strukturovaných zeolitických katalyzátorů pro proces hydroizomerizace *n*-hexanu

ANOTACE

Hydroizomerizace lineárních nebo málo větvených alkanů, prostřednictvím alkenů jako meziproduktů, je významným procesem pro rafinaci C_5 a C_6 uhlovodíkových frakcí pro zvyšování oktanového čísla automobilových paliv. Hydroizomerizace vede k transformaci lineárních alkanů s nízkým oktanovým číslem na větvené izomery s dostatečně vysokým oktanovým číslem. Pro hydroizomerizaci alkanů se osvědčilo použití bifunkčních heterogenních katalyzátorů, které jsou kombinací kyselého katalyzátoru složeného z oxidů obsahujících kyselá aktivní centra a klastrů kovu, kde probíhá hydrogenace a dehydrogenace uhlovodíkových reaktantů. V ropném průmyslu jsou pro hydroizomeraci alkanů významné katalyzátory na bázi zeolitu, zejména typu MOR. Nicméně, dostupnost aktivních center pro molekuly C_6 je omezena pomalou difuzí úzkým kanálem zeolitu a celková účinnost katalytického procesu je tak limitována transportními jevy. Větvené alkany vzhledem k vyššímu kinetickému průměru difundují ještě pomaleji než lineární *n*-alkany. Dostupnost kyselých aktivních center v současných průmyslových katalyzátorech je typicky zvyšována částečnou dealuminací zeolitů, kdy dochází k extrakci části atomů hliníku ze strukturní mřížky, což vede k pozitivním texturním změnám v kanálové struktuře zeolitu, ale zároveň ke snížení koncentrace aktivních kyselých Brønstedovských center, jejichž přítomnost v zeolitu je podmíněna přítomností hliníku ve strukturní mřížce zeolitu. Z těchto důvodů byly v této práci použity různé post-syntézní úpravy zeolitů jako je desilikace, dealuminace a fluoridace. Jejich kombinací se upravý texturní parametry zeolitů, což umožní snadnější transport molekul uhlovodíků k aktivním centrům, a tím se dosáhne podstatného zvýšení rychlosti hydroizomerizační reakce, a posunu reakčních podmínek k nižším teplotám, kde je termodynamická rovnováha nakloněna k tvorbě vícerozvětvených alkánů. Dalším důležitým parametrem pro hydroizomerizaci C_6 je množství kyselých center obsažených v zeolitech. Analýza role zvýšené hustoty silně kyselých protonů ukázala, že vysoká hustota neinteragujících, ale blízkých a silně kyselých strukturních hydroxylových skupin, významně snižuje aktivační bariéru v izomerizační reakci ve srovnání se vzdálenými aktivnímí místy, a může poskytnout vyšší reakční rychlost ve srovnání k nejmodernějšími Pt/H-zeolitovými katalyzátory.

KLÍČOVÁ SLOVA

hydroizomerizace, *n*-hexan, dealuminace, desilikace, fluoridace, tvarová selektivita, mordenit (MOR), beta zeolit (*BEA), hierarchické zeolity

CONTENTS

INTRUDUCTION

1.1 Hydroisomerization of linear C_6 alkane

The gasoline contains predominantly the hydrocarbons with 4 - 10 atoms of carbon, higher hydrocarbons are present only in a trace amount.

The C_6 alkanes are present in significant amount in the crude oil and form an important part of gasoline. However, these hexanes occur predominantly in the linear form characterised by very low octane number (only about 25) in contrast to branched C_6 isomers having high octane number (up to about 90). The basic processes how to increase the octane number are methods of the reforming, catalytic cracking, alkylation or hydroisomerization. The hydroisomerization of light gasoline fractions has recently become one of the most widely used processes in the petroleum industry due to its relevance to environmentally friendly and economical production of gasoline [1].

This hydroisomerization reaction is become a key reaction for the production of automotive fuels focusing to transform the linear C_6 alkanes with low octane number into the branched isomers: 2, 2-dimethylbutane, 2, 3-dimethylbutane, 3-methylpentane and 2-methylpentane with sufficiently high octane numbers.

This complex catalytic hydroisomerization reaction consists of several steps. Hydroisomerization of linear C_6 alkanes start with dehydrogenation of a linear alkane to an alkene on a noble metal, and followed by skeletal isomerization of the formed alkene via protonization and a cyclopropyl intermediate on a strongly acidic site and re-hydrogenation of the branched alkene to the alkane [2-7].

1.2 Hydroisomerization reaction over zeolites

Currently, the most used catalysts for hydroisomerization of C_5 and C_6 hydrocarbon fraction are based on chlorinated alumina, sulfated oxides or zeolites. Though low operating temperatures are highly important for isomerization catalysts, they are not the only criterion of their efficiency. The all process characteristics have to be consider, e.g. feed hourly space velocity (FHSV), the operating pressures, the composition of raw materials (the $C_5 : C_6$ ratio) and contents of naphthenes, benzene, sulfur and H_2O microadmixtures, etc.[1]

The chlorinated alumina has several disadvantages, since the chlorination occurs by reversible chemical exchange of the surface hydroxyl groups of the alumina support. That is the reason why the use of this catalyst is associated with constant supply and formation organochlorine compounds during the hydroisomerization reaction [1], which leads to serious questions about the environmental impact. Created organic chlorines have to be removed using scrubbers. The neutralization of fluegases and ellimination of environmentally harmful wastes raises the cost of operating[1]. Advantage of chlorinated alumina catalysts is their high activity at temperatures as low as 150 °C [8-9].

For the aforementioned reasons, the development is focused on enviromentaly friendly catalysts based on zeolites. Most of important acid-catalyzed industrial processes for production of fuels in oil processing, of chemical commodities, and fine chemicals in numerous organic syntheses are catalyzed by zeolite-based catalysts. Zeolites are used primarily as catalysts for catalytic cracking and hydrocracking in the petrochemical industry, for the production of chemicals (e.g. ethylbenzene, cumene, cyclohexanone) or fuels, for the oligomerization of olefins, xylene synthesis and isomerisation, production of gasoline and synthesis of light olefins from methanol. The 95% of the synthetic zeolites is applicated in catalytic cracking (FCC) and hydrocracking (HDC). These catalytic applications are based on the Y type zeolite of the FAU family. Other zeolites are used in petroleum industry such as based on the MOR zeolite applied in hydroisomeriztaion of C_5-C_7, the BEA zeolites used in alkylation reactions, or ZSM-5 zeolites applied for oligomerization of light olefins and hydrocracking of heavy aromatics into light oleffins [10].

Aluminosilicate crystaline framework of zeolites forms define micropores of large inner surface area and dimensions similar to kinetic diameters of organic molecules determining the space for the formation of reaction intermediates and products. Structure of thermally stable zeolites has the unique catalytic properties governed by the concentration and distribution of strongly acidic protons, and shape selectivity of inner micropores.

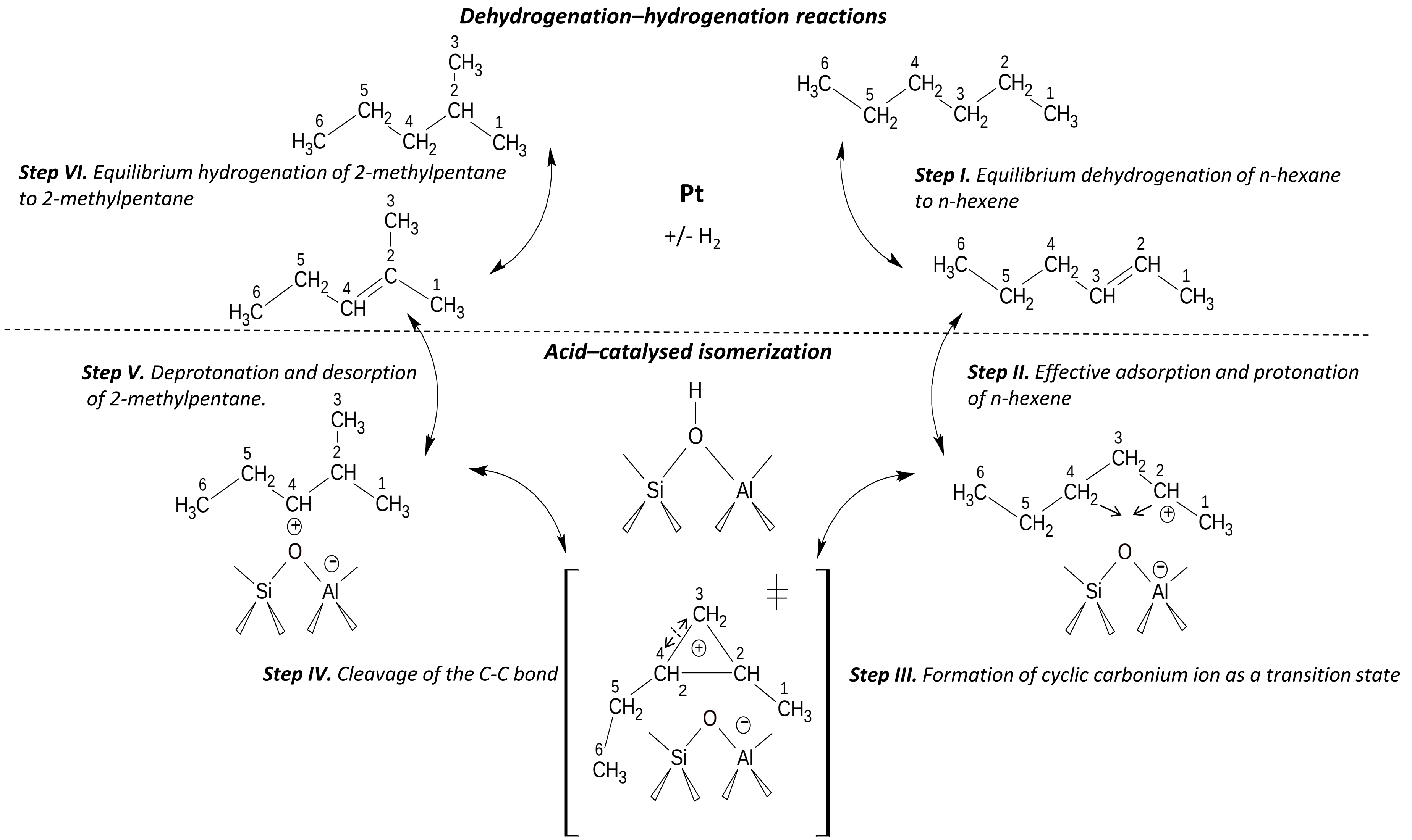

Figure 1. Illustration of complex reaction mechanism for *n*-hexane hydroisomerization on bifunctional Pt/H-zeolite catalysts.

For hydroisomerization are used bifunctional Pt/H-zeolite catalysts. The acid active sites in zeolites catalyse the skeletal isomerization reaction and Pt particles have dehydrogenation/hydrogenation functions. The reaction scheme of the hydriozomerization of C_6 alkanes using H/Pt zeolites is shown in Figure 1. The first step of hydroisomerization reaction is dehydrogenation of the linear *n*-hexane to *n*-hexene on the Pt particles. This dehydrogenation reaction provides a low and stable concentration of *n*-hexene. From the *n*-hexene, the branched isomers are formed on strongly acidic active sites in the zeolite via cyclic carbocation intermediate. The presence of hydrogen gas blocks the formation of carbon deposits on catalysts [1]. Dehydrogenation is a very fast reaction and do not limit overall reaction rate of the process at proper dispersity and concentration of platinum. The reaction rate of the process is controlled by acid catalysed reaction steps.

1.3 Zeolites as heterogenous catalysts in hydroisomerization of *n*-hexane

More than 150 commercial catalysts based on zeolites were proposed for refining processes (e.g. isomerization of paraffins and aromatics, hydro-cracking, aromatization reactions). The high activity and selectivity of zeolites and lower coke formation relative to the previous generation of catalysts (amorphous silica–alumina's) allowed refiners to increase gasoline output [10]. The success of zeolites in the industrial catalytic reactions is due to their relatively high acidity or mild basicity, stable structure at high temperatures (>400–800 °C) allowing use in the very harsh conditions, their channels pore system for optimum management of the molecular transport, their shaping (extrudates, spheres, microspheres) making them easy to handle and to separate in various catalytic reactor configurations, their non-corrosive and non-toxic character, their versatile composition (Si/Al ratio) and properties adaptable using the ion-exchange [10].

The unique catalytic properties of zeolites are based on the concurrent interaction of a hydrocarbon molecule with the acidic site [11] and adsorption in the confined reaction space of zeolitic channels [12-13]. The acidic sites in zeolitic channels of similar dimensions to hydrocarbon molecules provide high activity and selectivity in a wide range of relevant acid-catalysed reactions not available in other non-zeolitic catalysts [14-15].

1.3.1 Structure of zeolites

Zeolites are crystalline microporous aluminosilicates and their frameworks are built from TO_4 tetrahedra (T= Si or Al atoms), where every oxygen atom is shared between two T atoms. The chemical composition of a zeolite framework can be therefore expressed as a combination of the SiO_2 and AlO_2 units. SiO_2 units are neutral, but every AlO_2 unit has one negative charge which is normally compensated by a cation, e.g. Na^+ or K^+. These metal cations can be exchanged by other cations, including protons forming the Brønsted acid centers. Lewis acid centers are associated with the presence of coordinated unsaturated metal cations, e.g., aluminum cations or network defects [16]. These acid centers of zeolite play a dominant role in the catalysis. The strength of the centers depends on the structure of the zeolites, but it is known that the strongest centers are isolated centers. The creation of the acidic centers in the zeolite structure and incorporation of precious metals into the zeolites led to the forming the classical catalysts with dehydrogenation and hydrogenation functions and the formation of bifunctional catalysts. These catalysts are used for technological processes such as hydrocracking or hydroisomerization of *n*-alkanes.

Aluminosilicate crystalline structure of channels in zeolites forming defined micropores system determining the space for the formation of reaction intermediates and reactant transport allows the use of these materials as shape-selective catalysts. This phenomenon was first described by Weisz at al. [17] based on the determinant influence of the shape and size of zeolite micropores on the type of products created as a result of the catalytic reaction. On the zeolites was observed that the selectivity of the substrate, intermediate or final product can be based not only on particle blocking larger than the zeolite channels but also on the difference of diffusion coefficients in pores [17].

The structural formula of zeolites based on the crystallographic unit cell is:

$$\mathbf{M_{x/n}\,[(AlO_2)_x\,(SiO_2)_y]\,\cdot w\,H_2O}$$

where ***M*** represents the exchangeable cation of a valence ***n, y/x*** is the framework Si/Al molar ratio and **w** is water content inside of the zeolite channels.

Very important parameter of the zeolites is Si/Al ratio. From this parameter is unfolding properties of zeolites, such as their thermal stability, strength of acid centers, and ion exchange capacity for ammonium or other metal ions. In depending on the Si/Al ratio, zeolites have different affinities for polar molecules. Low silicon zeolites (LTA, FAU, MOR, natural zeolites) are hydrophilic and strongly interact with other polar molecules, while high silicon zeolites (ZSM-5) are hydrophobic. The smallest and possible Si/Al ratio according to Lowenstein´s rule is 1, the Al-O-Al bonding is not allowed [18].

1.3.2 Types of zeolites

The strong development of zeolite chemistry has led to the fact that currently 235 unique structures can be distinguished (for the IZA Structural Committee, April 2018). In spite of this large amount, it is important to realize that only a few types of zeolites are used in the industrial scale. The most important types of zeolites include FAU, *BEA, ZSM-5, MOR and FER [19].

Mordenite zeolite (MOR) is one of the most industrially important catalyst based on zeolites for hydroisomerization of C_6 alkanes working at temperature about 220-290°C [1]. This zeolite has the two types of channels: large 12-memberedd-ring (12-MR) channels (7.0×6.7 Å) and small 8-MR side pockets located between 12-MR channels (Figure 2A and Figure 3). The hydroisomerization of C_6 alkanes was suggested to be controlled by the concentration of acid sites in the channels of MOR zeolite. It has been proved that the active sites located in the 8-MR channels provide five times higher catalytic activity compared to the active sites located in the 12-MR channels [20]. However, the accessibility of these 8-MR side pockets compared to 12-MR channels is limited. Diffusion limitations due to restricted access for *n*-hexane (cf. the size of the channel openings and kinetic diameters of the hexane isomers in Figure 2) [21-24] and slow transport to/from the active site decrease catalyst efficiency and support further transformations of desired products [21, 25].

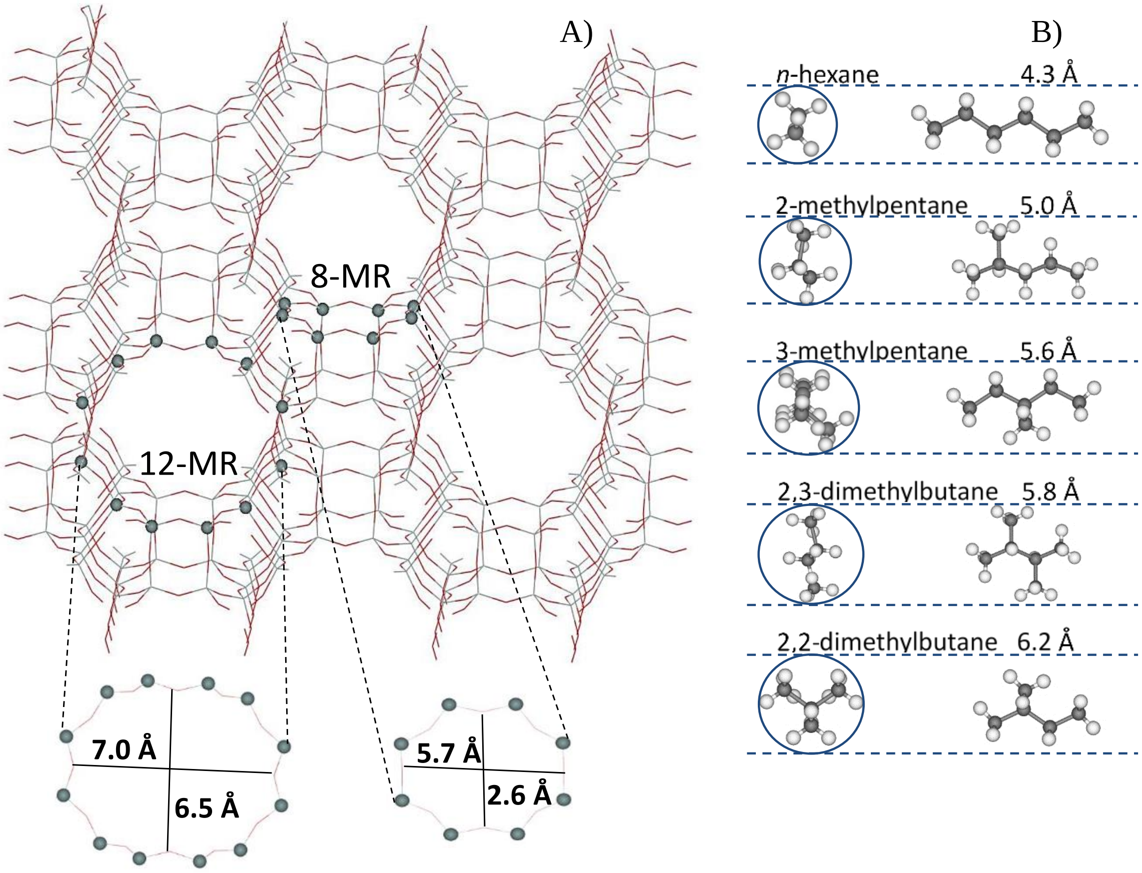

Figure 2. Illustration of the size-restriction of 8-ring compared to 12-ring channels in skeletal isomerization of *n*-hexane over mordenite zeolite. A) Topology of microporous mordenite zeolite consisting 12-ring (7.0 Å x 6.5 Å) channel and 8-ring (5.7 Å x 2.6 Å) side-pockets, B) kinetic diameters of hexane isomers [24].

Beta zeolite (BEA) is ranked between industrially catalyst based on zeolites used usually for alkylation of aromatics or hydrocracking [10]. But, in this work we wanted shown the potencial of this zeolite for the hydroisomerization of *n*-hexanes. The BEA network is crystallized in a tetragonal system and its elementary unit consists of 64 tetrahedral atoms. This zeolite has 3D structure containing the large 12-MR channels with size of opening window 7.6 x 6.4 Å (Figure 3).

Zeolite ZSM-5 (Zeolity Socony Mobil 5) was first synthesized in Mobil Oil laboratories in 1972. The unit cell of ZSM-5 zeolite consists of the 96 tetrahedrons. The three-dimensional zeolite pores system consists of two types of channels that lead into the 10- section windows (Figure 3). The channels have a straight section of 5.3 x 5.6 Å parallel to the direction [010], and channels elliptical 5.1x 5.5 Å elongation in the direction [100]. The wide range of ZSM-5 zeolite in catalytic applications includes the reforming of gasoline, the MTG process (methanol to gasoline) as well as isomerization or separation of the aromatic compounds [10].

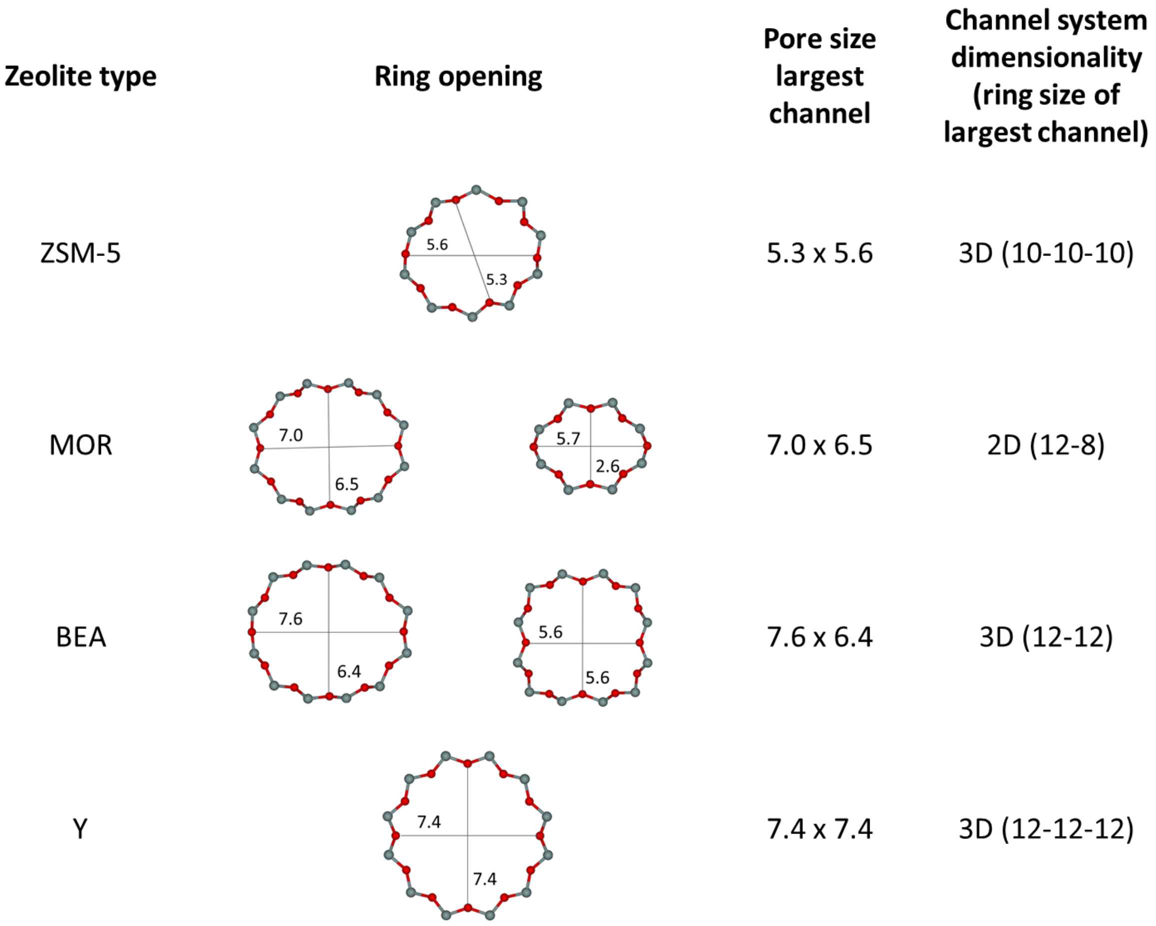

Figure 3. Schematic illustration of types of zeolite and their size of channels system.

The synthetic zeolites X and Y were first synthesized in the years 1949-1954 in the Linde Laboratories of Union Carbide Corporation. They have a FAU structure consists of 192 tetrahedral TO_4 atoms. The FAU zeolites have high microporous volume availability ~ 50%. At the beginning of 50 years of last century, the zeolite Y was used in cracking heavy petroleum fractions and was led as the most important commercially used zeolites. Zeolites X and Y have the same structure but different Si/Al ratio (Si/Al 1.0-1.5 for X and 1.5-3.0 for Y). Because of the difficulty of directly obtaining the stable zeolite FAU structure with Si / Al ration more than 3 which would have the sufficient acidity required in reactions involving hydrocarbons, the post-synthesis modifications are used. The first of them is the removal of aluminum atoms from the zeolite structure leading to an increase in the framework Si/Al ratio. The dealumination is carried out using steam at high temperatures leading to the stabilized zeolite USY. In the first step, the aluminum is separated from zeolite framework under the influence of water vapor. In the second phase, the resulting free positions from aluminum are replaced by silicon originating from the locally collapsed zeolite matrix. The choice of suitable dealuminated conditions allows control of the modification of the zeolite matrix because too harsh conditions could resulted in a loss of the crystalline structure of the zeolite [26-27]. The first stabilized Y zeolite (USY = ultrastabilized Y) was described by McDaniel and Maher in 1968 [28]. Appropriate acidity and hydrothermal stability in the resulting zeolite USY has enabled its use on an industrial scale.

1.4 Hierarchical zeolites

In recent years, considerable efforts have been devoted to improve pore accessibility and molecular transport of reactants to active sites in micropores, namely in ZSM-5 zeolites, to enhance the activity to desired products in major chemical processes. Diffusion limitations due to restricted acces and slow transport to/from the active sites decrease catalyst efficiency and support further transformation of desired products. These facts represent a major drawback in most indrustrial reactions catalysed by zeolites in hydrocarbon cracking, hydroisomerization, alkylation, transalkylation and esterification.

Several approaches to minimize diffusion limitations and enhance the catalyst effectiveness were developed. Synthesis of zeolites by using nanosheets [29], methods creating larger micropores [30] and the synthesis of zeolite prepared by confined crystal growth [31-32] or with using polymers as mesoporogens [33] were suggested . These strategies can overcome some diffusional limitations.

Nevertheless, the most of these methods are not really applied in the industry due to of demanding technical and synthetic operations. Therefore, we tried find such the synthesis of hierarchical zeolites which will be easier, cheaper, enviromentaly friendlier and can be really used in the industry.

The potentially suitable strategy to obtain resulted products is to synthesize hierarchical zeolites that combine the primary micropore and a secondary system which is consisted of mesopores (2–50 nm) inside the microporous zeolite crystals, through using post-synthesis desilication and dealumination processes[23, 34-38]. The advantage of the presence of mesopores in the zeolite crystals for reaction rate is accompanied by the formation of the non-shape selective enviroment of the acid sites in the mesopores. These are easily accessed by reactants but behave like non-selective sites on open surfaces.

The current industrial catalysts use acid-treated partially dealuminated MOR of improved textural properties. But the dealumination leads to a loss in the concentration of Brosted sites, formation of Lewis sites and small changes of micropores. The intruduction of secondary mesoporosity into MOR provides opportunity for much dramatic enhancement of accessibility of active sites with preservation of a vast amount of acid sites.

1.4.1 Hierachical structure trough desilication and dealumination methods

As already mentioned, it is possible to create zeolites with micromesoporous structure using special dealumination or desilication leaching procedures leading to the enhanced access to the active sites located in the inner part of zeolites with secondary mesoporous structure and thus eliminate the problem with diffusion of reactants and products to these active sites.

1.4.1.1 Desilication of zeolites

The principles of desilication of zeolites were described by Groen at al. with H-ZSM-5 zeolite crystals by their treatment in alkaline solution. Their group stressed the importance of Si/Al ratio in the zeolites and that the presence of Al atoms in zeolite framework is important for stabilization a neighbouring siliceous parts of the crystal zeolite [34].

It was found that the optimal Si/Al ratio for development of mesoporosity with preserved Al centers inside zeolite framework is 25-50. Lower Si/Al ratios (Si/Al<20) enable limited formation of mesopores becouse the desilication is restricted by higher concentration of aluminum atoms (the negatively charged AlO_4^- tetrahedra were found to prevent the Si extraction). On the other side, Si/Al ratios > 50 lead to the excessive and unselective Si dissolution which can lead to formation of relative large pores but also to destruction or completly dissolution of zeolite structure. For these reasons, conditions of desilication have to be optimized carefully for each type of zeolite [23].

1.4.1.2 Dealumination of zeolites

It has also been found that for the preparing hierarchical zeolites with using dealumination is better applied to zeolites with a higher Si/Al ratio. The higher Si/Al ratio is beneficial for stability during dealumination of zeolite and forming acid sites with higher strength [40].

Dealumination can be done with using hydrolysis at steamtreatment or by direct application of acids of a proper concetration. Special dealumination with adding water steam is used for syntehsis of zeolite Y with higher Si/Al ratio (USY zeolite). In this process, aluminum from the framework of zeolite can be removed during calcination, thus the defect sites and Al extra-framework species in the zeolite are formed. These Al extra-framework species are washed with diluted acid and removed. As a result of this process the mesopores with size distribution about 2-50 nm are created [28, 40]. Dealumination can be applied on the other zeolites such as mordenite, *BEA, ZSM-5 zeolite or ferrierite. However, the mesopores are created by direct acid treatment with strong acid such as acetic, oxalic, tartaric acid or nitric, sulfuric or hydrochloric acid at different concentrations. Their concentration is highly dependent on the nature a types of zeolite. For examples, in a comparison of several zeolite structures, *BEA zeolite is easier for dealumination than mordenite, while ZSM-5 is nearly unaffected under similar conditions [40]. On the other side, the strong concentration of used acid can lead to loss of crystallinity or destruction of zeolitic structure. The removing of aluminum atoms from the zeolite framework during the formation of mesopores leads to a change in Si/Al ratio and as follows the acidity. In contrast to the dealumination which preferentially removes Al framework atoms, the alkaline leaching selectively extractes Si framework atoms. The SiO_2 atoms are present in significantly higher amount than Al atoms in the zeolite structure and therefore the desilication does not cause so dramatic changes in Si/Al ration. It was also shown that mesopore structures are preferentially created at edges or defect sites of the zeolite crystals.

Sazama at al. [38] demonstrated the feasibility of creation of micromesoporous structure in the zeolites with protonic sites located in the shape-selective environment of micropores through the mesopores. It was suggested and approved that post-sythesis procedures involving controlled desilication and subsequent partial dealumination, provide hierarchical zeolites with such located protons.

Due to the high potential of hierarchical zeolites for industrial application, the research in this study deals with economically viable and scalable post-synthesis desilikation method. In contrast to dealumination, the controlled desilication of zeolite framework using alkaline treatment followed by tailored acid leaching of Al-sites predominantly from the mesopores leads to a preservation of the concetration of Bronsted sites and formation of well developed secondary mesoporosity. Hierarchical zeolite with enhanced access to the active sites located in the shape-selective environment of micropores and accessible through mesopores has high potentional for partical application in the hydroisomerization of linear C_5-C_6 alkanes into the branched ones with high octane number [41-43]. Synthesis of these zeolites with tailored hierarchical structure create an unique opportunity to advance in the new direction of the efficient use of zeolitic catalysts based on commercially produced types of zeolites.

1.4.2 Post-synthesis modification of zeolites by fluorination

A fairly young method of achieving the hierarchical structure of zeolite is a combination of a desiccation and fluoridation method which allows the controlled extraction of Al and Si from the zeolite to form a micromesoporous structure. This method was described for the ZSM-5 zeolite by Yu at el. [44] using the NaOH leaching and impregnation by NH_4F solution. The insertion of the fluorination as step prior to desilication allows the creation of secondary mesoporous structure formed by the extraction of both Si and Al atoms at the same time. The process allows the formation of interconnected opened channel structures with accessible acidic active sites of zeolites without large decrease in their concentration. This post-synthesed modification is optimal for different types of zeolites for creation of secondary mesoporosity [41] (in the case of Si rich zeolites) and forming of supermicroporosity [42] (in the case of Al-rich zeolite). It is expected that modified zeolites prepared by the combination of desilication, dealumination and fluorination methods can provide the hierarchical structure more accessible for reactants and with high concentration and availability of Brønsted active sites, thus providing a significantly higher catalytic activity in the hydroisomerization of C_6 alkanes [41-43].

2 AIM OF THE THESIS

The aim of this dissertation thesis is to understand relations between the local arrangement of active sites in microporous and micromesoporous zeolites and skeletal isomerization of *n*-hexane in order to adapt the structure of zeolite catalysts to increase their activity and selectivity for branched C_6 alkanes. The major objective was rational design of isomerization zeolite catalysts providing superior activity and shifting the window of operating temperatures to the thermodynamically more suitable area for the formation of di-branched isomers.

Two approaches were employed for this purpose in these studies focusing on enhancement of the concentration and/or the accessibility of active sites. The studies attempted to enhance the accessibility of the active sites by introducing secondary mesoporosity into mordenite zeolites coupled while attempting to preserve a large number of acid sites. The objective was attainment of the enhanced accessibility of acid sites using post-synthesis methods which are easy for application and really usable in industry. The aim was to explore potential for effective formation of secondary mesoporosity through postsynthesis alkaline, alkaline−acid, acid−alkaline−acid, and fluorination−alkaline leaching procedures of conventional microporous mordenite zeolites. The aim was also the modification of the structure of mordenite zeolite to provide an increase in the dimensions of the microporous channel openings, enlargement of the micropores and 3D interconnection of the micropores by postsynthesis concurrent extraction of Si and Al atoms from the framework using fluorination-alkaline-acid treatments. The objective of this paper was also analysis of the effect of a micromesoporous structure on the shape selectivity. A synthesis of zeolites of *BEA structural topology with unique density and distribution of strongly acid sites was exploited to increase the concentration of active sites. This approach was used with the aim to examine of the extent to which the isomerization reaction is affected by high density and close proximity of strongly acidic centers.

3 EXPERIMENTAL PART

3.1 Preparation of hierarchical zeolites using post-synthesis treatment

The several types of parent zeolites were used in this work (Table 1). Two parent zeolites of the MOR structure (Table 2), designated as MOR/A/12 and MOR/B/5.8, and four parent zeolite of ZSM-5 structure (Table 3), designated as ZSM-5/A/25, ZSM-5/B/25, ZSM-5/C/15 and ZSM-5/D/22.5 were used for preparation of their hierarchical structure using postsynthesis treatment. Two zeolite of *BEA structure, designated as *BEA/A/11.3, Al-rich *BEA sturucture, designated as *BEA/B/4.2 and one zeolite of faujasite structure, designated as USY/6 were used for analysis and comparing of the catalytic properties (Table 1).

Table 1. List of parent microporous zeolites

Sample	Synthesis
ZSM-5/A/15	Microporous ZSM-5 (Zeolyst Int., CBV 3020, Si/Al = 15)
ZSM-5/B/25	Microporous ZSM-5 (Zeolyst Int., CBV 5524G, Si/Al = 25)
ZSM-5/C/25	Microporous ZSM-5 (Zeolyst Int., CBV 5020, Si/Al = 25)
ZSM-5/D/22.5	Microporous ZSM-5 (Alsi Penta, SM-55, Si/Al = 22.5)
MOR/A/12	Microporous MOR (Zeolyst Int., CBV 20A, Si/Al 12.1)
MOR/B/5.8	Microporous MOR (Zeolyst Int., CBV 10A, Si/Al 5.8)
***BEA/A/4.2**	Microporous Al-rich *BEA (synthesised, Si/Al 4.2)
***BEA/B/11**	Microporous *BEA (Zeolyst Int., CP814B-25, Si/Al 11.3)
USY/6	Microporous USY (Zeolyst Int., CBV 712, Si/Al = 6)

Schema of preparation of micro-mesoporous mordenite zeolites using postsynthesis alkaline-acid (Series I), acid-alkaline-acid (Series II), and fluorination-alkaline-acid (Series III) leaching procedures is illustrated in Figure 4. One of the parent MOR zeolite, denoted as MOR/A/12 (Figure 4 and Table 2) was used for preparation of micromesoporous mordenites using postsynthesis treatment: alkaline-acid leaching (Series I), acid-alkaline-acid leaching (Series II), and fluorination-alkaline-acid leaching (Series III) procedures [41]. The Ist series (Figure 4), micromesoporous mordenites were prepared using alkaline-acid treatments by leaching MOR/A/12 in an alkaline solution (30 ml 0.2 M NaOH per 1 g mordenite stirred in a beaker at 85 °C for 2 h, sample mm-MOR/A/8) and subsequent leaching in acid solutions

(30 ml 0.1 M oxalic acid per 1 g alkaline treated zeolite stirred in a beaker at 85 °C for 20 h, sample deAl-mm-MOR/A/9, or 40 ml 0.1 M HNO_3 per 1 g alkaline treated zeolite stirred in a beaker at 50 °C for 15 min, sample deAl-mm-MOR/A/9.5). The IInd series (Figure 4) was prepared using acid-alkaline-acid treatments with dealumination of MOR/A/12 (30 ml 3 M HNO_3 per g mordenite stirred and heated under reflux at 80 °C for 40 min, sample deAl-MOR/A/16), subsequent desilication (30 ml 0.2 M NaOH per 1 g dealuminated zeolite stirred in a beaker at 85 °C for 2 h, sample mm-deAl-MOR/A/9.1), and finally mild dealumination (30 ml 0.1 M HNO_3 per 1 g zeolite at 50 °C for 15 min, sample deAl-mm-deAl-MOR/A/13; or 30 ml 0.1 M $(COOH)_2$ per 1 g zeolite at 85 °C for 20 h, sample deAl-mm-deAl-MOR/A/30). The IIIrd series (Figure 4) was prepared by fluorination of MOR/A/12 (5 g mordenite were impregnated by 15 ml 0.36 M NH_4F at room temperature, stored at RT for 8 h, and subsequently dried at 120 °C for 12 h), subsequent desilication (30 ml 0.2 M NaOH per 1 g fluorinated mordenite stirred in a beaker at 85 °C for 30 min) and calcination at 550 °C for 3 h (sample mm-MOR/A-0.36F/9.4), with subsequent leaching in acid solutions (30 ml 0.1 M HNO_3 per 1 g zeolite at 50 °C for 15 min, sample deAl-mm-MOR/A-0.36F/13.6) [41].

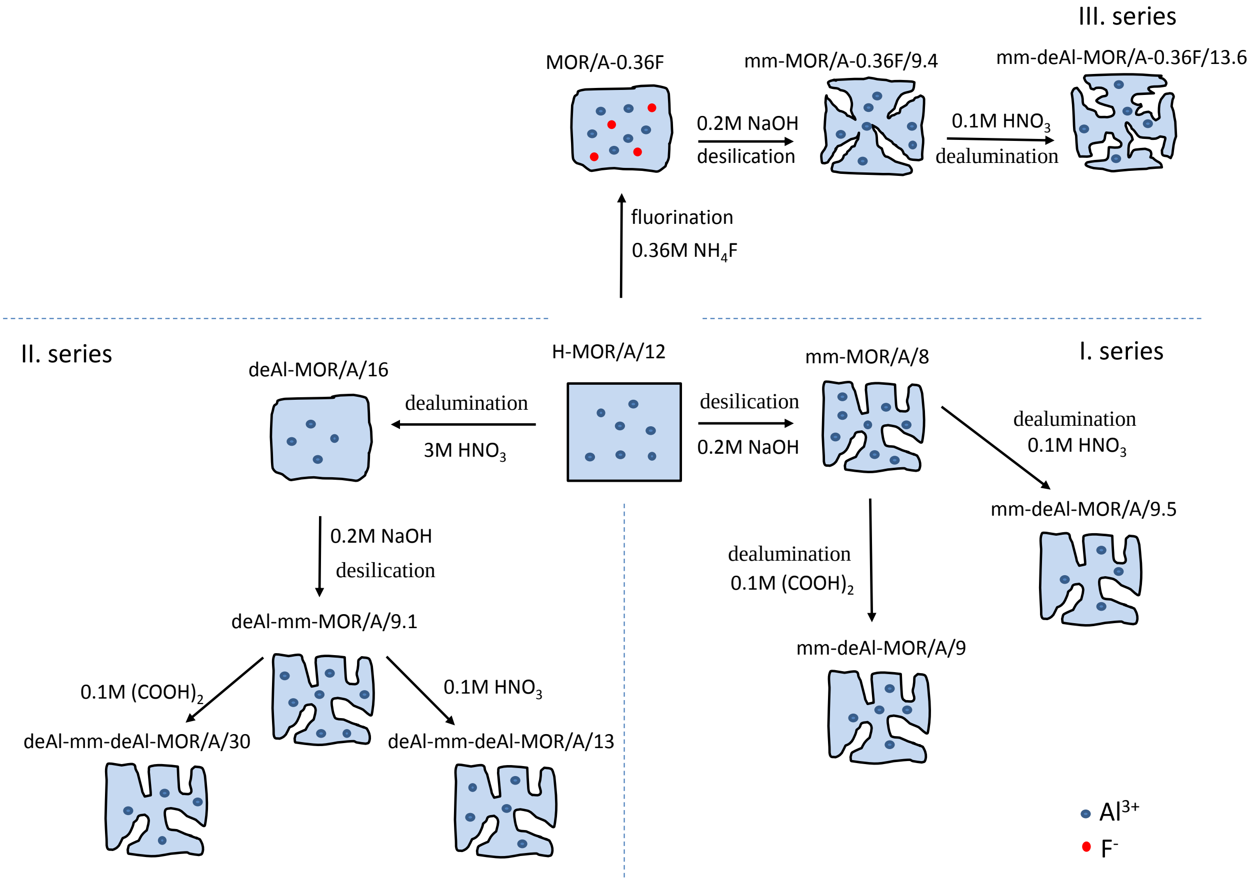

Figure 4. Schema of preparation of micro-mesoporous mordenite zeolites using postsynthesis alkaline-acid (Series I), acid-alkaline-acid (Series II), and fluorination-alkaline-acid (Series III) leaching procedures.

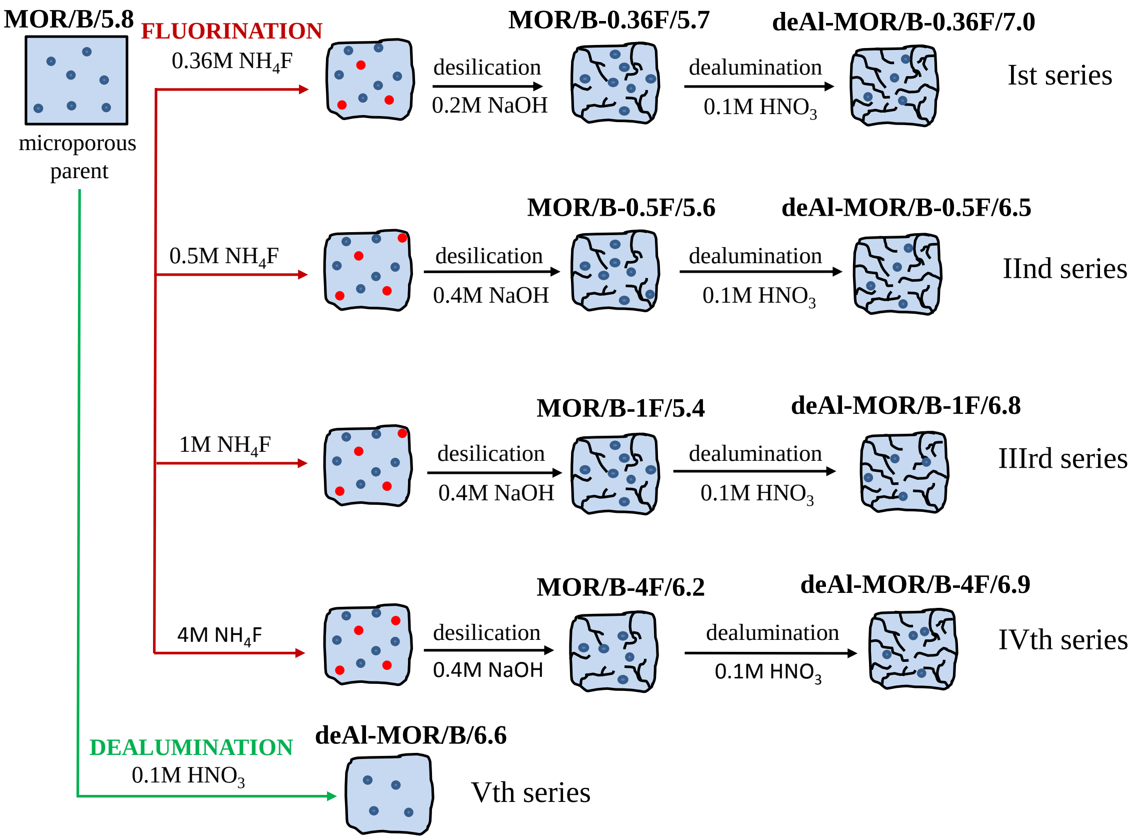

Figure 5. Scheme of the preparation of the supermicroporous mordenites using postsynthesis fluorination-alkaline-acid (Series I-IV), and acid (Series V) treatments.

The second parent MOR zeolite (Table 2 and Figure 5), denoted as MOR/B/5.8, was used for preparation of mordenites with enhanced accessibility of micropores using postsynthesis fluorination-alkaline-acid leaching procedures (Figure 5). The MOR/B/5.8 was treated by fluorination-alkaline leaching with various concentrations of NH_4F and NaOH and subsequently by mild dealumination [42]. Typically, 5 g of MOR zeolite was impregnated with 15 ml aqueous solutions of NH_4F at room temperature, kept at RT for 8 h and was then dried at 120 °C for 12 h and calcined at 550 °C for 3 h. The alkaline treatments were applied on the fluorinated zeolites (1 g of fluorinated MOR per 30 ml NaOH solution stirred in a beaker at a temperature of 85 °C for 30 min). In the Ist series (Figure 5) concentrations of 0.36 M NH_4F and 0.2 M NaOH solutions were used and the sample was denoted as MOR/B-0.36F/5.7. The IInd series was prepared using 0.5 M NH_4F and 0.4 M NaOH solutions and the sample denoted as MOR/B-0.5F/5.6. For the preparation of the IIIrd series (Figure 5), 1 M NH_4F and 0.4 M NaOH solutions were used and the sample was denoted as MOR/B-1F/5.4. The IVth series was prepared using 4 M NH_4F and 0.4 M NaOH solutions and the sample was designated as MOR/B-4F/6.2. Finally, after fluorination and alkaline treatment, the samples were mildly dealuminated by adding 30 ml of 0.1 M HNO_3 per 1 g prepared MOR at 50 °C for 15 min and the samples were designated as deAl-MOR/B-0.36F/7.0, deAl-MOR/B-0.5F/6.5, deAl-MOR/B-1F/6.8 andBdeAl-MOR/B-4F/6.9 (Table 2). For the Vth series, the parent MOR zeolite was treated only by dealumination with HNO_3 (1 g parent MOR zeolite was added to 30 ml 0.1 M HNO_3 at 50 °C for 15 min) and the sample was denoted as deAl-MOR/B/6.6 [42].

Table 2. List of prepared micromesoporous MOR zeolites using postsynthesis treatment

Sample	Synthesis
MOR/A/12	**Microporous parent MOR**
mm-MOR/A/8	+ 0.2M NaOH
deAl-mm-MOR/A/9	+ 0.2M NaOH + 0.1M $(COOH)_2$
deAl-mm-MOR/A/9.5	+ 0.2M NaOH + 0.1M HNO_3
deAl-MOR/A/16	+ 3M HNO_3
mm-deAl-MOR/A/9.1	+ 3M HNO_3+0.2M NaOH
deAl-mm-deAl-MOR/A/13	+ 3M HNO_3 + 0.2M NaOH + 0.1M HNO_3
deAl-mm-deAl-MOR/A/30	+ 3M HNO_3 + 0.2M NaOH + 0.1M $(COOH)_2$
mm-MOR/A-0.36F/9.4	+ 0.36 M NH_4F + 0.2M NaOH
deAl-mm-MOR/A-0.36F/13.6	+ 0.36 M NH_4F + 0.2M NaOH + 0.1M HNO_3
MOR/B/5.8	**Microporous parent MOR**
MOR/B-0.36F/5.8	+ 0.36 M NH_4F + 0.2 M NaOH
deAl-MOR/B-0.36F/7.0	+ 0.36 M NH_4F + 0.2 M NaOH + 0.1 M HNO_3
MOR/B-0.5F/5.6	+ 0.5 M NH_4F + 0.4 M NaOH
deAl-MOR/B-0.5F/5.6	+ 0.5 M NH_4F + 0.4 M NaOH + 0.1 M HNO_3
MOR/B-1F/5.4	+ 1M NH_4F + 0.4 M NaOH
deAl-MOR/B-1F/6.8	+ 1 M NH_4F + 0.4 M NaOH + 0.1 M HNO_3
MOR/B-4F/6.2	+ 4 M NH_4F + 0.4 M NaOH
deAl-MOR/B-4F/6.9	+ 4 M NH_4F + 0.4 M NaOH + 0.1 M HNO_3
deAl-MOR/B/6.6	+ 0.1 M HNO_3

Several types of parent ZSM-5 zeolites (Table 3) were used for preparation of their micromesoporous analogues using fluorination−alkaline leaching procedures according to procedures reported by Yu et al. [44]. 5 g of ZSM-5 zeolite was impregnated with 15 ml of aqueous solution of 0.36 M NH_4F at room temperature, stored at RT for 8 h, then dried at 120 °C for 12 h, and subsequently calcined at 550 °C for 3 h. The calcined zeolite was than leached in an alkaline solution (30 ml 0.2 M NaOH per 1 g of fluorinated ZSM-5 stirred in a beaker at 85 °C for 30 min). The obtained samples were denoted as mm-ZSM-5/A-F/10.2, mm-ZSM-5/B-F/15.9, mm-ZSM-5/C-F/15.1, and mm-ZSM-5/D-F/13.4 (Table 3). The synthesis steps of fluorination and alkaline treatments were subsequently repeated on modified micromesoporous ZSM-5 samples under the same conditions yielding samples designated as mm-ZSM-5/A-F/6.9 and mm-ZSM-5/B-F/12.9 (Table 3) [43].

All types of prepared zeolites were ion-exchanged with 0.5 mol.dm^{-3} NH_4NO_3 solutions at RT (1 g of a zeolite per 100 cm^3 of solution, three times over 12 h) to obtain the ammonium form of the zeolites. All parent zeolites of MOR, ZSM-5, *BEA and USY structure (Table 1) were used as a standard for comparing catalytic properties.

For the reaction of hydroisomerization of *n*-hexane, the Pt was introduced into the zeolites in the NH_4^+ forms by incipient wetness impregnation of pre-dried (105 °C/2 h) powdered material by H_2PtCl_6 solution to yield 1.5 wt. % of Pt. The amount of aqueous solution of H_2PtCl_6 and its concentration used for the impregnation were calculated based on the porous volume of each zeolite [41-43].

Table 3. List of prepared micromesoporous ZSM-5 zeolites using postsynthesis treatment

Sample	Synthesis
ZSM-5/A/15	Microporous parent ZSM-5
mm-ZSM-5/A-F/10.2	+ 0.36 M NH_4F + 0.2 M NaOH
mm-ZSM-5/A-F/6.9	+ 0.36 M NH_4F (2x) + 0.2 M NaOH (2x)
ZSM-5/B/25	Microporous parent ZSM-5
mm-ZSM-5/B-F/15.9	+ 0.36 M NH_4F + 0.2 M NaOH
mm-ZSM-5/B-F/12.9	+ 0.36 M NH_4F (2x) + 0.2 M NaOH (2x)
ZSM-5/C/25	Microporous parent H-ZSM-5
mm-ZSM-5/C-F/15.1	+ 0.36 M NH_4F + 0.2 M NaOH
ZSM-5/D/22.5	Microporous parent ZSM-5
mm-ZSM-5/D-F/13.4	+ 0.36 M NH_4F + 0.2 M NaOH

3.2 Characterization of prepared zeolites

3.2.1 FTIR

The FTIR spectra of the H-form of the zeolites were measured on a Nicolet nexus 670 FTIR spectrometer. Self-supporting wafers were made from the zeolite samples and inserted into the metal holder in the IR cell. The wafers of zeolite samples were evacuated at 450 °C kept over 3 h and then recorded at RT by collecting 256 scans at 2 cm^{-1} resolution for each spectrum.

The CD_3CN was used as a molecular probe for analysis of the concentration of Brønsted and Lewis acid sites. CD_3CN was adsorbed at a partial pressure of 10 Torr for 20 min at RT and subsequently desorbed for 15 min at RT. The resulting IR spectra of the stretching C≡N vibrations and the extinction coefficients $\varepsilon_B = 2.05$ cm.μmol^{-1} and $\varepsilon_L = 3.60$ cm.μmol^{-1} were used for calculations of the acidic Brønsted and Lewis sites concentrations [45].

The accessibility of the OH groups for *n*-hexane in the zeolites was measured using the adsorption of *n*-hexane. The *n*-hexane was adsorbed on the dehydrated samples at a vapour pressure of 1.4 Torr for 20 min at RT with gradual desorption to 0.005 Torr at RT. The accessibility of the OH groups in the zeolite samples was determined by subtracting in the intensity between the absorption bands of the dehydrated spectra of the zeolite and the spectra after adsorption of *n*-hexane [41].

Information on the oxidation and coordination states of Pt particles in the zeolite was obtained using the method of CO adsorption as a molecular probe in FTIR spectroscopy. Before adsorption of CO, the zeolite samples were heated at 450 °C for 1 h and then activated by reduction in H_2. Hydrogenation of the zeolite samples was performed by gradually heating of the sample from RT to 250 °C, which was maintained for 1 h. Subsequently, the samples of Pt/H-zeolite were evacuated and CO was applied for 30 min. Finally, the IR cell with the samples was degassed and the spectra were recorded at RT [41-43, 46].

The 2,6-diterbuttylpyridine (DTBPy), whose the kinetic diameter is too large to penetrate into the micropores with 10-MR ring openings (ZSM-5 zeolite) was adsorbed at a partial pressure of 1.4 Torr at 150 °C. The FTIR spectra of adsorbed (DTBPy) were used for relative comparison of the populations of acid sites on the external surface of microporous and micromesoporous ZSM-5 zeolites [43].

3.2.2 XRD

The crystalline structure of the zeolites was analysed by X-ray powder diffraction (XRD). The XRD patterns were obtained using a Bruker AXSD8 Advance diffractometer with CuKα radiation in Bragg–Brentano geometry and a position sensitive detector (Våntec-1) in a 2θ range 5-90°.

3.2.3 SEM, TEM

SEM and TEM microscopy was used to verify of maintaining of the shape and size of the crystal zeolite, the Pt particales in the zeolite, the formation of mesopores and the lattice fringes after post-synthesis treatment. SEM micrographs were obtained on a Hitachi S-4800 field emission scanning electron microscope. Sputter coating of samples with a noble metal was not necessary. High-resolution transmission electron microscopy (HR-TEM) measurement was carried out on a JEOL JEM 3010 microscope (cathode LaB_6, point resolution 1.7 Å), operated at 300 kV with samples of zeolites calcined at the temperature of 500 °C and subsequently reduced in a hydrogen atmosphere at 250 °C.

3.2.4 Nitrogen adsorption

The texture parameters of modified zeolitic materials were determined by analysis of the N_2 adsorption isotherms at the temperature of liquid nitrogen (77 K) in the ASAP 2010 apparatus (Micromeritics) and by the Ar adsorption isotherms at the boiling point of liquid nitrogen Ar/LN_2 in the Micromeritics 3Flex system. Prior to the adsorption measurements, desorption of the samples was performed at 240 °C for 24 hours. Broekhoff-de Boer t-plot fitting was used for determining the micropore volume; the total pore volume V_{tot} was obtained from the adsorption at a relative pressure of 0.8 and converted to the corresponding volume of liquid nitrogen. A relative pressure of 0.8 should ensure the complete filling of the pores by N_2 and, at the same time, this pressure is low enough to leave a substantial proportion in the interstitial space. The mesopore size distribution was calculated using DFT method based on a model for the adsorption of nitrogen on oxidic surfaces.

The Ar adsorption isotherms at the boiling point of liquid nitrogen were employed for analysis of the micropore size distribution, as the spherical and smaller molecule of Ar is more suitable for analysis of sub-nanometer microporous structure in a low pressure region.

Micropore size distribution was calculated by the Horwath-Kawazoe method used in the Saito-Foley extension to cylindrical pores applicable to studies of zeolites. The Cheng-Yang correction for the non-ideality of the two-dimensional behaviour of the adsorbed gas was taken into account. All the methods used were performed using Micromeritics software. In contrast, the numerical values of the micropore volume are influenced by the inaccuracy of the measurement at higher relative pressures due to working at a temperature below the temperature of liquid Ar. The adsorption isotherms of Ar are normalised accordingly to the Gurvich rule by multiplying the adsorption isotherm by $V_{tot\ N_2}/V_{tot\ Ar}$. The mesoporous volume V_{ME} and surface area were also calculated from the Ar adsorption isotherms.

3.2.5 NMR

The solid state ^{27}Al MAS NMR method was used for characterization of the Al species with different coordination in the zeolite. The experiments were performed on a Bruker Avance 500 MHz Wide-Bore spectrometer (11.7 T) equipped with a 4 mm double-resonance MAS NMR probe head. The ^{27}Al MAS NMR spectra of the fully hydrated samples were measured with a high-power decoupling pulse sequence with a p/12 (0.7 μs) excitation pulse, 1 s relaxation delay and rotation speed of 12 kHz. The chemical shifts were referred to an aqueous solution of $Al(NO_3)_3$. ^{29}Si MAS NMR single pulse spectra of hydrated zeolites were measured at a rotation speed of 7 kHz, with a $\pi/6$ (1.7 μs) excitation pulse and relaxation delay of 30 s for single pulse spectra. The framework aluminum content (Si/Al_{FR}) was estimated from the intensity of the ^{29}Si NMR resonances according the equation $Si/Al_{FR} = I/(0.25\ I_1 + 0.5\ I_2)$, where I, I_1, and I_2 correspond to the total, Si(3Si,1Al), and Si(2Si,2Al) intensity. The ^{1}H MAS NMR single pulse spectra were collected after 128 scans with a $\pi/2$ (4 μs) excitation pulse and 2s repetition delay at a rotation speed of 11 kHz. To obtain the protonic form *BEA samples were dehydrated in-situ in 4 mm ZrO_2 MAS NMR rotors at 450 °C (ramp 1 $°C.min^{-1}$) under dynamic vacuum of 5.10^{-1} Pa for 6 h.

3.2.6 UV-vis

The ability of Al-rich H-*BEA zeolite form carbenium ions was analyzed by UV-Vis spectroscopy using hexamethylbenzene (HMB) molecule [46]. The UV–Vis spectra of *BEA zeolites dehydrated at 500 °C in a vacuum after interaction with HMB at 200 °C for 1, 2 and 3 h and after subsequent interaction with NH_3 were measured in the range from 20 000 to

45 000 cm^{-1} using a Perkin-Elmer Lambda 950 spectrometer equipped with a Spectralon integration sphere. HMB was introduced into the dehydrated zeolite by mixing the powdered zeolite and HMB in a glovebox and the measurements were performed using a cell enabling collection of the spectra without exposure of the mixture to the air.

3.2.7 Hydroisomerization of *n*-hexane

The catalytic activity in hydroisomerization of linear n-hexane to the corresponding mono-branched (1-mehtyl- and 2-methyl-pentanes) and di-branched (2,2-dimethyl and 2,3-dimethyl-butanes) isomers was performed in U-shaped glass through-flow reactor with catalyst loading of 0.5 g on a porous glass septum. Preheating of the reactants was performed in spiral tubing in the inlet part of the reactor. Before each catalytic experiment, activation of the Pt/MOR-zeolite was performed in an oxygen stream at 450 °C for 3 h and then cleaned with pure nitrogen for 15 min. After calcination, the temperature was lowered to 250 °C and the catalyst was reduced in a mixture of 79 mol % H_2 + 20 mol % N_2 at 250 °C for 1 h. Then 1 mol % of *n*-hexane was fed into this mixture using a glass saturator kept at the selected temperature. The total gas flow was thus set at 66 $cm^3.min^{-1}$, and this corresponded to GHSV 5 000 and WSHV 0.25 h^{-1}. The reactor temperature was kept in the desired range of 125 – 325 °C, controlled by an inserted K-thermocouple. The final product containing: n-C_6, iso-C_6 and low molecular products (i.e.: C_1, C_2, C_3, C_4 and iso-C_4, C_5 and iso-C_5) was analysed by an on-line connected GC (Finnigan 9001), furnished with a capillary column (Al_2O_3/KCl) and a FID detector. A steady-state regime was typically attained during approx. 0.5 - 1 h of time-on-stream.

The conversions and yields of branched hexane isomers and lower molecular weight by-products were also analyzed under process-like conditions. These catalytic tests were performed using a stainless-steel gas flow tubular PID Eng&Tech Microactivity – Reference reactor at a pressure of 10 bar with a H_2 to hexane molar ratio of 6 and amount of catalyst equal to 2.5 g (5 ml) with a flow rate corresponding to WHSV 0.7 h^{-1} and GHSV 638 h^{-1}. The temperature was controlled by an internal thermocouple and kept at the desired temperature in the range 200 - 215 °C. Liquid *n*-hexane was continuously loaded by a Gilson 307 pressure pump and evaporated in the hot flow of hydrogen gas. The reaction products were analyzed using an on-line connected Perkin Elmer Clarus 580 gas chromatograph equipped with CP-Sil Pona CB column (100 m x 0.25 mm x 0.5 μm) and a FID detector.

4 RESULTS AND DISCUSSION

4.1 Enhancement of accessibility of acid sites in micromesoporous zeolites

This chapter describes the methods for effective formation of secondary mesoporosity through postsynthesis alkaline, alkaline-acid, acid-alkaline-acid and fluorination-alkaline leaching procedures of conventional mordenite zeolites. These syntheses attempted to enhance the accessibility of the active sites by introducing secondary mesoporosity into mordenite zeolites coupled while attempting to preserve a large number of acid sites. In contrast to dealumination, controlled alkaline-based treatments of the mordenite framework lead to better preservation of the concentration of Brønsted sites and formation of well-developed secondary mesoporosity. The process was followed in respect to the state of Al, the concentration and accessibility of Brønsted sites and Al-Lewis sites together with changes in the micro-meso texture and how these parameters are reflected in *n*-hexane hydroisomerization over H/Pt-MOR.

4.1.1 Structural analysis of micromesoporous mordenite zeolites

4.1.1.1 Effect of dealumination on zeolite structure, concentration, nature and accessibility of acid sites

The microporous MOR/A/12 parent zeolite is characterised by well-developed crystalline structure (Figure 6) with the microporous volume 0.19 $cm^3.g^{-1}$ (Table 4 and Figure 7) and the presence of the majority of the Al in the framework in tetrahedral coordination (Figure 8).

The FTIR spectra of the OH groups and adsorbed d_3-acetonitrile together indicate a slightly predominant concentration of Brønsted sites in the 12-ring compared to 8-ring channels, compensating the negative charge of regularly tetrahedrally coordinated Al in the framework, and a low concentration of Lewis acid sites (Table 5 and Figure 10).

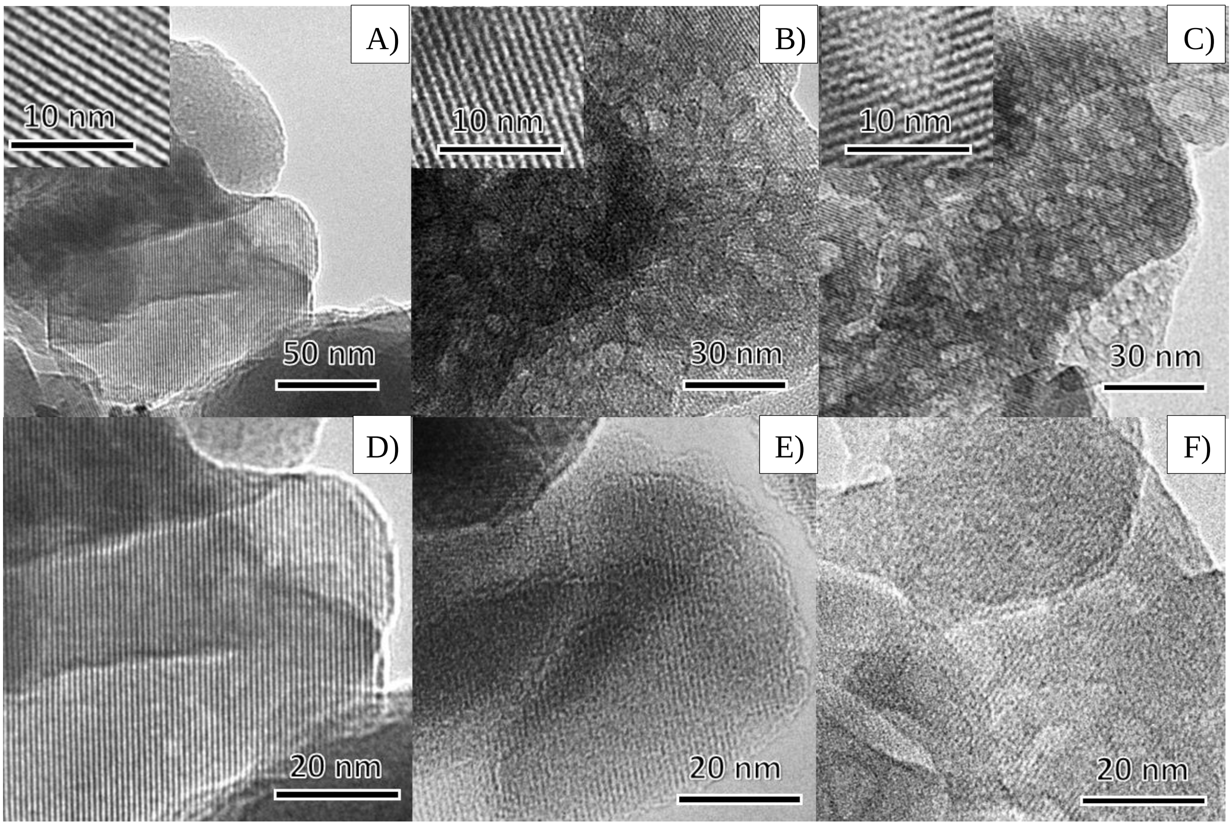

Figure 6. Representative HR-TEM images of A, D) microporous MOR (MOR/A/12), B) micro-mesoporous MOR (mm-MOR/A/8), C) dealuminated micro-mesoporous (deAl-mm-MOR/A/9.5), E) fluorinated MOR (MOR/A-0.36F) and F) fluorinated micro-mesoporous MOR (mm-MOR/A-0.36F/9.4).

Table 4. Preparation and textural properties of micro-mesoporous mordenite zeolites.

Sample	Si/Al[a]	Si/Al$_{FR}$[b]	V_{tot} (P/P_0~0.8)	V_{MI}[c]	V_{MESO}[d]	S_{EXT}[c]
				(cm^3. g^{-1})		(m^2. g^{-1})
MOR/A/12	12.1	12.5	0.24	0.19	0.05	42
mm-MOR/A/8	8.7	10.2	0.14	0.06	0.08	79
deAl-mm-MOR/A/9	9	11.2	0.24	0.13	0.11	107
deAl-mm-MOR/A/9.5	9.5	-	0.25	0.13	0.12	114
deAl-MOR/A/16	16.1	-	0.24	0.19	0.05	44
mm-deAl-MOR/A/9.1	9.1	-	0.26	0.15	0.11	102
deAl-mm-deAl-MOR/A/13	13.5	-	0.26	0.19	0.09	88
deAl-mm-deAl-MOR/A/30	30	-	0.30	0.20	0.10	95
mm-MOR/A-0.36F/9.4	9.4	-	0.23	0.14	0.09	104
deAl-mm-MOR/A-0.36F/13.6	13.6	-	0.22	0.14	0.08	104

[a] from chemical analysis [b] from ^{29}Si MAS NMR [c] estimated from BdB *t-plot* method [d] $V_{meso} = V_{total} - V_{micro}$

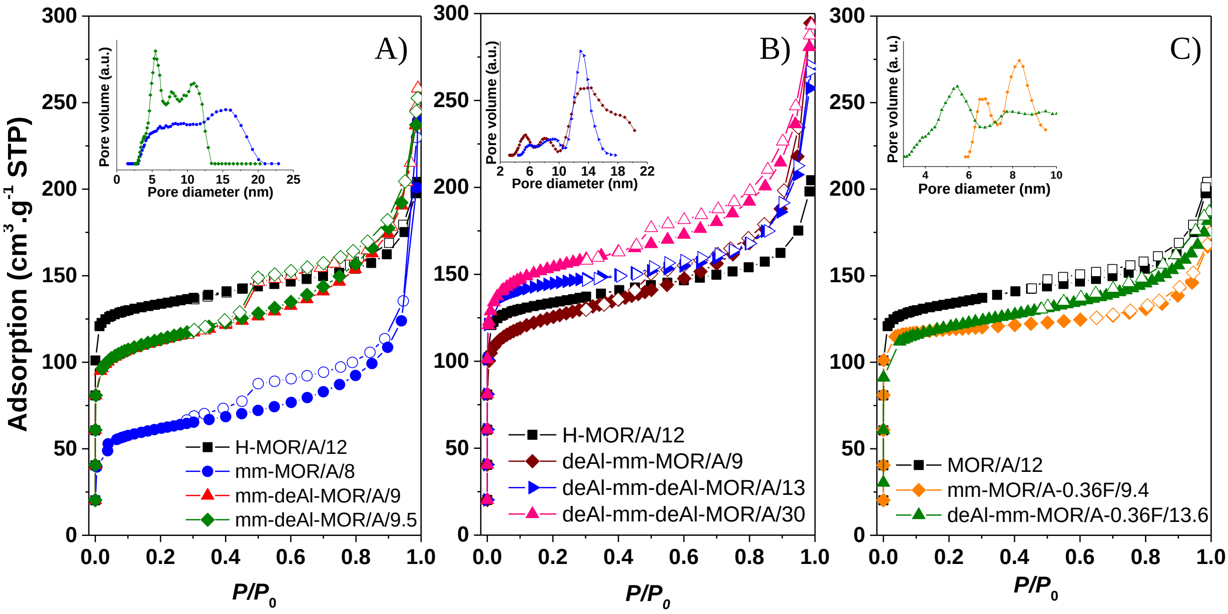

Figure 7. Nitrogen adsorption (solid symbols) and desorption (open symbols) at 77 K on microporous and micro-mesoporous mordenite zeolites prepared by sequential alkaline and acid leaching for A) Series I., B) Series II., C) Series III.

Observation of the intensity of the infrared bands corresponding to OH groups in 8-ring and 12-ring channels upon introduction of *n*-hexane (Table 5 and Figure 9) was used for estimation of the accessibility of OH groups located in the distinct channels. The band attributed to OH groups in the 8-ring channels of MOR was almost unperturbed after adsorption of *n*-hexane, indicating low accessibility of these OH groups for the probe molecule at RT. This is in accordance with the observation of very low accessibility of the acid sites located in 8-ring channels reported by Eder et al. [47]. Both the experimental [48-50] and theoretical studies [51] of mordenite zeolites showed approximately 1/3 of the Brønsted hydroxyl groups heading toward the centre of 8-ring and centre of the side pocket, which is non-accessible for larger molecules. This number seems to be independent of the Si/Al ratio [47] and is a result of the distribution of Al atoms in the four tetrahedral sites of mordenite [48]; this corresponds well to 64.1% the accessible OH groups for n-hexane in H-MOR/A/12 (Table 5).

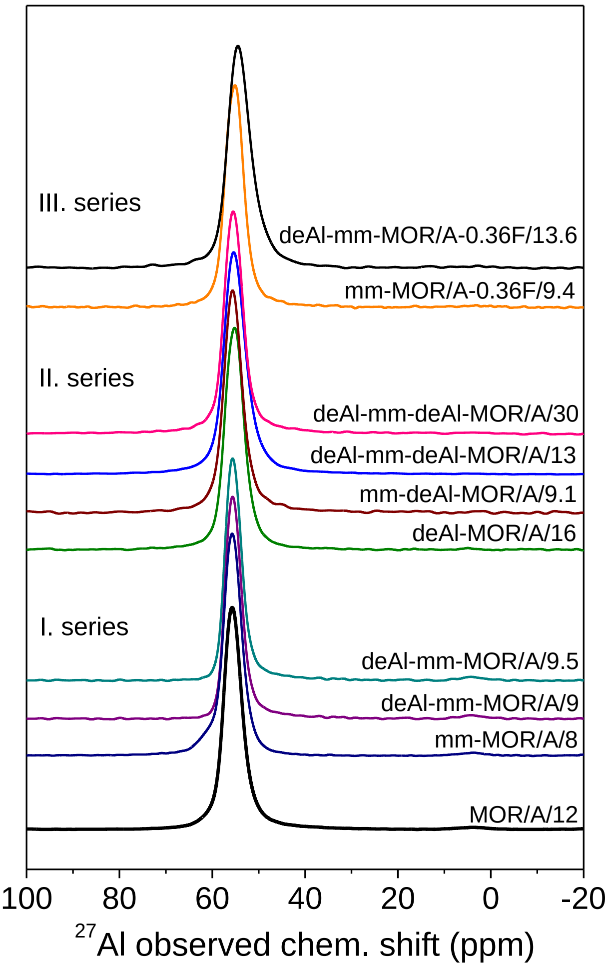

Figure 8. ^{27}Al MAS NMR spectra for microporous and micro-mesoporous MOR zeolites.

Table 5. The concentrations of bridging hydroxyls and Brønsted and Lewis sites in zeolite and accessibility of OH groups in micro-mesoporous mordenites.

Sample	Si/Al[a]	c_{Al} [a]	c_B [b]	c_L [c]	c_{B+2L} [d]	Accessibility of OH groups [e] (%)
			(mmol.g^{-1})			
MOR/A/12	12.1	1.23	1.06	0.12	1.30	64.1
mm-MOR/A/8	8.7	1.49	0.44	0.14	0.72	-
deAl-mm-MOR/A/9	9	1.67	0.81	0.35	1.51	68.7
deAl-mm-MOR/A/9.5	9.5	1.60	0.55	0.20	0.95	79.1
deAl-MOR/A/16	16.1	0.97	0.47	0.13	0.73	92.6
mm-deAl-MOR/A/9.1	9.1	1.65	0.44	0.22	0.88	-
deAl-mm-deAl-MOR/A/13	13.5	1.15	0.43	0.45	1.33	91.6
deAl-mm-deAl-MOR/A/30	30	0.53	0.27	0.20	0.67	74.4
mm-MOR/A-0.36F/9.4	9.4	1.61	0.60	0.24	1.09	90.0

[a] from chemical analysis
[b, c] concentrations of acid Brønsted and Lewis sites, respectively, from FTIR spectra of adsorbed *d*$_3$-acetonitrile
[d] concentration of Al estimated from the concentration of Brønsted and Lewis sites ($c_{Al} = c_B + 2c_L$)
[e] from FTIR spectra of the bridging OH groups after adsorption of *n*-hexane

After partial dealumination of the framework of the parent mordenite zeolite by 3 M HNO_3 (Figure 4), the Si/Al ratio was increased from 12 to 16 with a corresponding decrease in the concentration of the Brønsted sites, accompanied by an increase in the ratio of Lewis/Brønsted sites (Table 5) and a significant increase in the absorption bands at 3 727 cm^{-1}, corresponding to internal silanol groups (Figure 10). The decrease in the concentration of the Brønsted sites and the increase in the band of internal silanol groups are consistent with the removal of the tetrahedrally coordinated framework Al atoms and the formation of four internal SiOH groups terminating the framework oxygen atoms. The structural changes induced by dealumination of mordenite zeolites have been described well in the scientific literature [21, 25, 52].

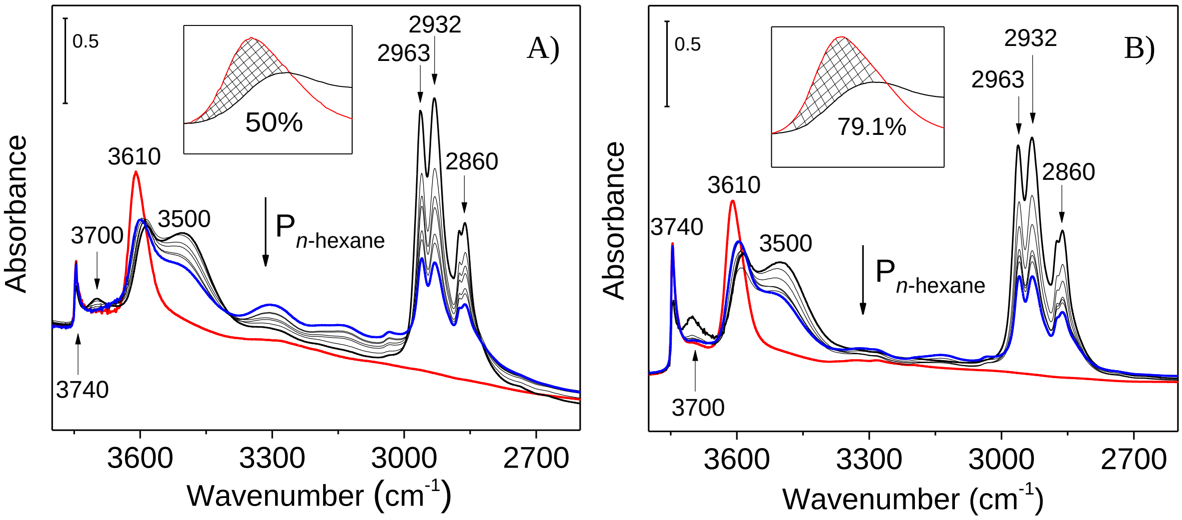

Figure 9. Illustration of analysis of the OH groups accessibility using FTIR spectra of adsorbed *n*-hexane from 1.4 Torr to 0.001 Torr, A) MOR/A/12 and B) deAl-mm-MOR/A/9.5.

Removal of the framework Al atoms by acid leaching with nitric acid has been reported to result in secondary micropores that are larger than the main channels [25, 52] or the formation of small mesopores [25], improving the accessibility of the Brønsted OH groups remaining after dealumination in the side pockets. The similar adsorption/desorption branches of N_2 sorption (Figure 7) without a hysteresis loop for both MOR/A/12 and deAl-MOR/A/16 indicate the absence of a significant volume in intra-crystalline mesopores. The adsorption of *n*-hexane on deAl-MOR/A/16 caused a dramatic decrease in the intensity of the absorption bands of OH groups that clearly show that the Brønsted acid sites remaining in the deAl-MOR/A/16 sample zeolite after dealumination are readily accessible for the *n*-hexane molecule (>90%), (Table 5).

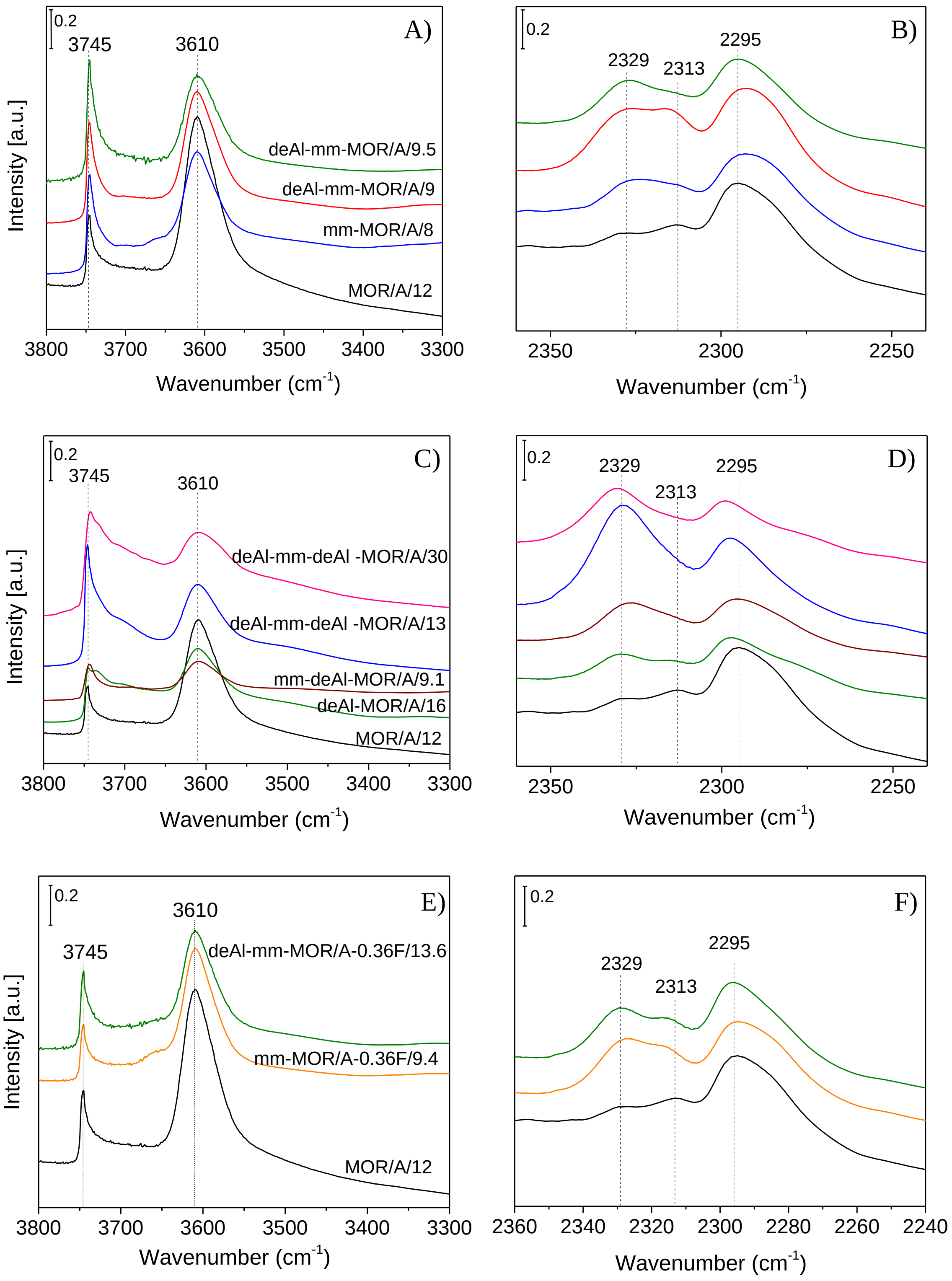

Figure 10. FTIR spektra of adsorbed d_3-acetonitrile (B, D, and F) and FTIR spectra in the OH stretching region (A, C, and F) for microporous and micro-mesoporous H-MOR/A zeolites. A, B) Series I.; C, D) Series II.; and E, F) Series III.

The absence of mesopores, the increased accessibility of the OH groups and the presence of internal silanol groups indicates that extraction of the framework Al atoms primarily induced changes in the distribution of the sizes and/or the connectivity of the microporous channels. However, in addition to appreciable textural changes, these structural changes caused a significant decrease in the concentration of the Brønsted acid sites to about half and an increase in the ratio of Lewis/Brønsted sites [41].

4.1.1.2 Effect of desilication on zeolite structure

TEM images of the alkaline-leached zeolite mm-MOR/A/8 (Figure 6) clearly show that the treatment resulted in extensive formation of a secondary mesoporous structure characterized by numerous cavities about 5-20 nm in size in the microporous crystals. The adsorption isotherms of desilicated mm-MOR/A/8 zeolite (Figure 7) exhibit a hysteresis loop typical for mesopores and adsorption in the zeolite micropores with a significant decrease in the volume of the micropores from 0.19 to 0.06 $cm^3.g^{-1}$ (Table 4). The preservation of the crystalline structure of mm-MOR/A/8, which is obvious from the X-ray diffraction patterns (Figure 11) and indirectly from the ^{29}Si MAS NMR spectrum (Table 4), and the lattice fringes in the HR-TEM images (Figure 6) indicate that the decrease in the microporous volume is not associated with collapse of the zeolitic structure but with blocking of the channel openings by AlO_x extraframework plugs formed in the mesopores after desilication [38]. The extraframework Al species (Al_{Ex}) formed in the mesopores during desilication by hydrolysis of perturbed or dislodged framework Al enrich the surface [53] and can easily block a significant part of the pseudo-monodimensional channel structure of mordenite [38]. The presence of Al_{Ex} in mm-MOR/A/8 is obvious from i) the broadening and decreasing of the symmetry of the signal at 55 ppm in the ^{27}Al MAS NMR spectra (Figure 8) characteristic of variously perturbed Al species in the less-ordered environment compared to ideal tetrahedral coordination of Al atoms in the zeolite Framework [38, 54-59], ii) the additional spectral component around 3650 – 3670 cm^{-1} (Figure 10A) due to OH groups bound to extra-framework and/or perturbed framework Al atoms [60-62], iii) a higher framework Si/Al ratio estimated from the ^{29}Si MAS NMR spectra compared to the value obtained from chemical analysis (Table 4) and iv) a significant decrease in the concentration of Brønsted OH groups from 1.06 to 0.44 $mmol.g^{-1}$ determined from the FTIR spectra of adsorbed d_3-acetonitrile.

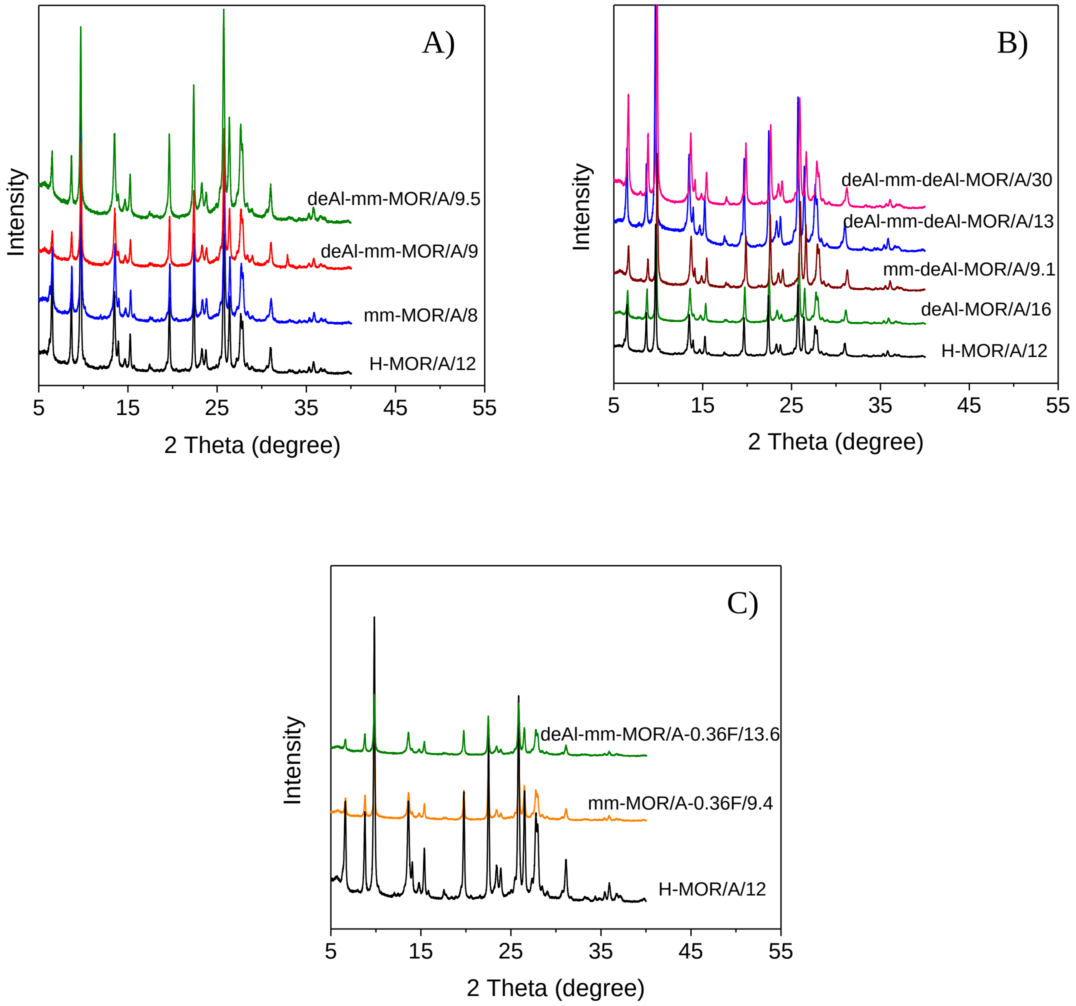

Figure 11. X-ray diffraction patterns of the micro-mesoporous mordenite zeolites prepared using post-synthesis A) alkaline-acid (Series I), B) acid-alkaline-acid (Series II), and C) fluorination-alkaline (Series III) leaching procedures.

Desilication of the partially dealuminated mordenite (deAl-MOR/A/16) (Figure 4) resulted in better developed secondary mesoporous structure compared to desilication of the parent mordenite, as indicated by higher and continuously increasing adsorption of N_2 at the relative pressures 0.1 – 0.8 and a hysteresis loop in the adsorption/desorption branches of the isotherm (Figure 7B). After the alkaline treatments, the mesoporous volume increased to 0.08 and 0.11 $cm^3.g^{-1}$ for mm-MOR/A/9 and mm-deAl-MOR/A/9.1, respectively (Table 4). It is well established that the presence of framework Al atoms stabilizes a neighbouring siliceous part of the crystal and the extraction of Si is hindered for low Si/Al ratios [34, 63]. Consequently, the lower content of Al in the framework of deAl-MOR/A/16 increased the susceptibility towards leaching of the framework Si atoms [41]. Desilication is also preferred more along crystal defects [64], which were densely created during the partial dealumination of the parent zeolite, and which are reflected in the FTIR spectrum of deAl-MOR/A/16 in the absorption bands at 3727 cm^{-1} of the internal silanol groups (Figure 10C). The preferred desilication in the internal Si-related defects is manifested in a decrease in the intensity of the absorption at 3727 cm^{-1} in the spectra of mm-deAl-MOR/A/9.1 compared to deAl-MOR/A/16. Thus, desilication is clearly enhanced upon prior partial dealumination of the microporous zeolite as a result of the higher susceptibility of the zeolite towards leaching at lower concentrations of framework Al atoms as well in the presence of the framework defect sites [41]. The analysis of N_2-sorption isotherms by the Broekhoff-de Boer *t*-plot shows a decrease in the micropore volume after desilication from 0.19 $cm^3.g^{-1}$ in the parent zeolite to 0.06 and 0.15 $cm^3.g^{-1}$ for mm-MOR/A/9 and mm-deAl-MOR/A/9.1, respectively (Table 4 and Figure 7). It is probable that a lower concentration of Al in the parent zeolite and/or more developed mesoporosity providing a larger number of openings of the pseudo-monodimensional channels lead to lesser blocking of the micropores in the mm-deAl-MOR/A/9.1 sample [41].

4.1.1.3 Effect of mild dealumination on zeolite structure and accessibility of acid sites

Our recent study [38] on the formation of secondary mesoporosity through postsynthesis sequential leaching procedures demonstrated that the Brønsted active sites located in the environment of non-restricted micropores and accessible through mesopores can be obtained by alkaline and subsequent mild-acid leaching. Treatment of mm-MOR/A/8 using 0.1 M oxalic acid (Figure 4, I. series) under mild conditions (deAl-mm MOR/A/9) resulted a very slight increase in the molar Si/Al ratio, a significant increase in the micropore volume from 0.06 to 0.13 $cm^3.g^{-1}$ and further extended the volume of mesopores (Table 4), a significant increase in the concentration of Brønsted sites from 0.44 to 0.81 $mmol.g^{-1}$ and Levis sites from 0.14 to 0.35 $mmol.g^{-1}$ (Table 5), disappearance of the lowering symmetry of the signal at 55 ppm in the ^{27}Al MAS NMR spectra (Figure 8), and elimination of the absorption band at 3650 – 3670 cm^{-1} due to Al-OH groups (Figure 10). These findings clearly indicate that the extra-framework and/or perturbed framework Al species formed in mesopores after desilication and blocking part of the micropores were removed by acid leaching. The increase in the concentrations of the acid sites indicates that the leaching selectively removed the extraframework tetrahedrally coordinated $AlO_x/(OH)_y$ species blocking the micropores, whereas the framework Al atoms associated with bridging OH groups were barely affected [41].

Acid leaching of mm-MOR/A/8 using 0.1 M nitric acid (Figure 4, I. series) resulted in slightly more pronounced structural changes compared to the treatment using oxalic acid. Nitric acid, as a stronger dealumination agent [65], caused a moderately greater increase in the molar Si/Al ratio, the same increase in the micropore volume from 0.06 to 0.13 $cm^3.g^{-1}$ and further extension of the mesoporous volume to 0.12 $cm^3.g^{-1}$ (Table 4). A lower concentration of Brønsted sites 0.55 $mmol.g^{-1}$ indicates that part of the framework Al atoms was extracted from the framework and/or perturbed by the treatment in nitric acid. The removal of extraframework Al in the deAl-mm-MOR/A/9 sample by oxalic acid (Figure 4, I. series) caused only minor changes in the availability of OH groups compared to the parent zeolite (Table 5). A significant increase in the accessibility of the OH groups (~80%) occurred after slight dealumination of the zeolite framework in the deAl-mm-MOR/A/9.5 sample by nitric acid (Figure 9). It seems that desilication with subsequent removal of extraframework Al can lead to shortening of the main 12-ring channels, but the number of new channel openings created in mesopores is not large enough for significant enhancement of the accessibility of the OH groups in 8-ring side pockets. Partial dealumination of mm-deAl-MOR/A/9.1 using 0.1 M nitric acid (Figure 4, II. series) caused similar changes to the dealumination of mm-MOR/A/8; however, they are less pronounced, i.e. opening of restricted micropores with an increase in the volume of micropores from 0.15 to 0.19 $cm^3.g^{-1}$ (Table 4) and increase in the concentration of Lewis sites from 0.22 to 0.45 $mmol.g^{-1}$ (Table 5). The concentration (0.43 $mmol.g^{-1}$) and accessibility of Brønsted acid sites (~ 92%) are very comparable with deAl-MOR/A/16. Thus the desilication of deAl-MOR/A/16 (Figure 4, II. series) with subsequent removal of Al_{Ex} by mild acid leaching resulted in deAl-mm-deAl-MOR/A/13 with well-developed mesoporous structure and with similar concentration and accessibility of OH groups for *n*-hexane as the starting deAl-MOR/A/16 before the subsequent alkaline-acid treatments [41].

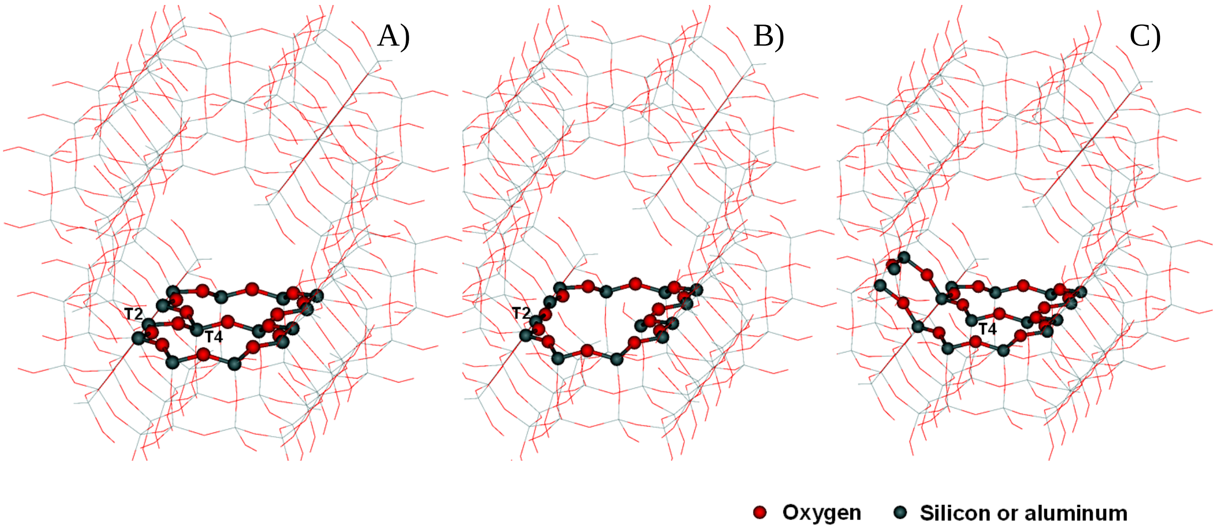

Figure 12. Schematic illustration of the effect of the extraction of one T atom from 8-ring on the local structure of the openings of the side-pockets in MOR zeolite. A) Two neighbouring 8-rings and the same structure with removed B) T4 atom and C) T2 atom.

The hydrolysis of Al-O and Si-O bonds in the 8-ring (formed by T2 and T4 atoms) during acid and alkaline treatments results in dislodgement of the T atom from the framework position and dramatic changes in the local arrangement [41]. Figure 12 illustrates how the openings of two neighbouring side-pockets in MOR zeolite can be altered by the removal of one T atom in the T2 or T4 sites. The extraction of the T4 atom leads to a merging of the two 8-ring providing a large void space enabling a diffusion of large molecules, e.g. benzene [66]. The extraction of the T2 atom could possibly provide a large deformed elongated ring, however, previous reports indicate that the extraction is site specific and the dealumination of T4 is strongly favoured [66-68]. The creation of these open connections by the preferable extraction of Al atoms from the T4 sites explains the dramatic increase in the accessibility of the bridging of OH for hexane even after very mild dealumination of the mordenite framework.

4.1.1.4 Effect of fluorination-alkaline treatment on zeolite structure and accessibility of acid sites

Recently, Yu et al. [44] showed that impregnation of microporous ZSM-5 zeolite with an aqueous solution of NH_4F prior leaching by a solution of NaOH increases the susceptibility of the zeolite towards leaching of framework Al atoms and provides controlled extraction of both Al and Si atoms. We modified the procedure for alkaline treatment of fluorinated mordenites and obtained the mordenite zeolite mm-MOR/A-0.36F/9.4 (Figure 4, III. series) with the mesopore volume increased to 0.09 $cm^3.g^{-1}$ and the volume of the micropores concurrently slightly decreased to 0.14 $cm^3.g^{-1}$ (Table 4) indicating the formation of secondary mesoporosity and opening of non-restricted channel openings of the preserved microporous structure [41]. In addition to the small near circular bright areas reflecting formation of intracrystalline mesoporosity, HR-TEM images (Figure 6) also show mesopores formed along boundaries and intergrowths. The dissolution or etching along boundaries and intergrowths and the indiscriminate dissolution of Al and Si are characteristic of chemical etching with fluoride ions in NH_4F-HF [44] and Al-directed dissolution of siliceous areas is typical for alkaline treatment [44]. Two modes of the formation of the mesoporous structure were also reported by Svelle et al. [64] for standard desilication. They demonstrated the creation of mesopores both as a consequence of Al-directed dissolution of siliceous areas and selective dissolution or etching along boundaries, intergrowths, and defects within each particle. HR-TEM images of mm-MOR/A-0.36F/9.4 (Figure 6F) show concomitant contribution of both modes of mesopores formation. The slight shift of the maximum of peak at about 55 ppm in the ^{27}Al MAS NMR spectra (Figure 8) reflects changes in the coordination and local surroundings of the Al sites and/or a site specific dealumination of the individual T sites [66-68]. The concentration of Brønsted and Lewis sites, 0.6 and 0.24 $mmol.g^{-1}$, respectively, determined by adsorption of d_3-acetonitrile, and high accessibility (>90%) of bridging OH groups for *n*-hexane molecule (Table 5) for the mm-MOR/A-0.36F/9.4 sample show that the desilication of fluorinated mordenite zeolite yields a micro-mesoporous structure with high concentration of readily accessible acid sites. The development of secondary mesoporosity and preservation of microporosity via concurrent extraction of SiO_2 and smaller amount of Al is enabled by transformation of a fraction of Si-O-Al into the framework as F-bearing tetrahedral Al entities after fluorination [44]. The presence of F-bearing tetrahedral Al species which are readily dislodged in alkaline medium [44] and Al sites in Si-O-Al entities with persistent resistance to alkaline treatment enabled controlled Al and Si extraction during the alkaline treatment. The finding that this treatment significantly improved the accessibility of OH groups for *n*-hexane is of great importance. The simultaneous removal of Si and Al atoms and smaller size of part of the formed mesopores with possibly a larger number of new channel openings results in a large increase in the accessibility of the OH groups for *n*-hexane [41].

4.1.1.5 *Effect of mesoporosity on pore length*

In order to illustrate the effect of mesoporosity on the reactant transport a model showing the shortening of the main 12-ring channels was made, and the desorption of *n*-hexane was analysed for the microporous and a representative micro-mesoporous mordenite (Figure 13).

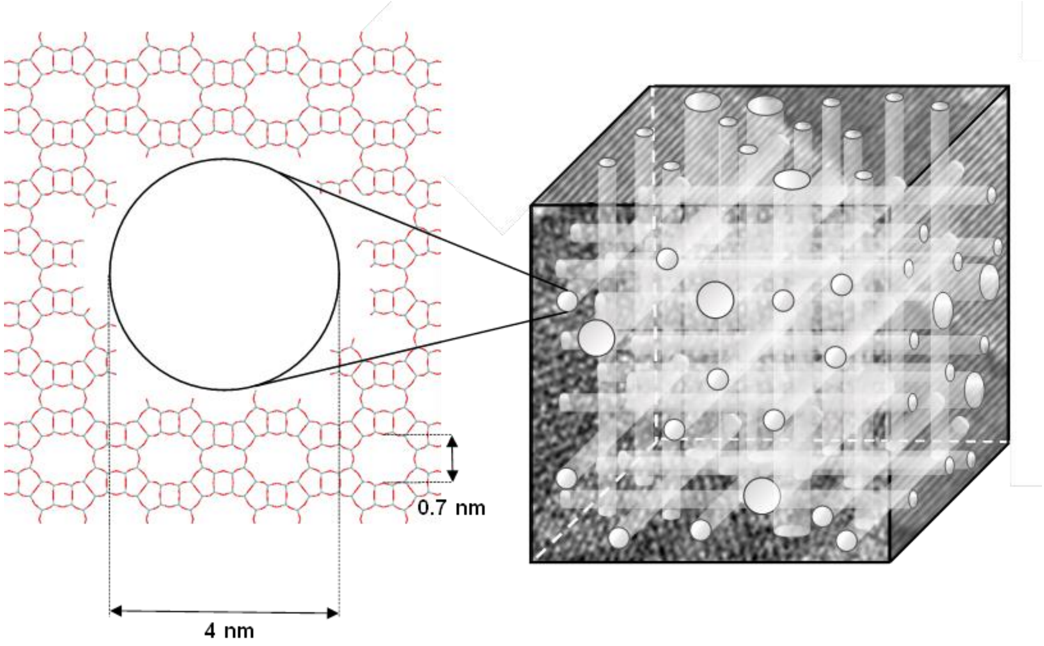

Figure 13. Analysis of the effect of the presence of mesopores on the length of zeolite channels and diffusion of *n*-hexane. Model determining the length of diffusion path through the mordenite channel, where 4 and 8 nm channels oriented along the axes and internal mesopore volume 0.09 $cm^3.g^{-1}$ were considered.

The model is based on the obtained SEM, HR-TEM and N_2 adsorption data considering the mesoporous volume 0.09 $cm^3.g^{-1}$, which is approximately 15% of the total volume of the crystal and the crystal size 80 nm. Two cases were modeled with randomly positioned mesopores of diameter 4 or 8 nm oriented along one of the crystal axes and connected to the external surface of the crystal. The mesopores that communicate with the external surface of the mordenite crystal are observed in the high resolution TEM images and the spatial arrangement of the mesopores in the entire void volume of the crystal was demonstrated by Milina et al. [69] using the positron annihilation lifetime spectroscopy for micro-mesoporous zeolites prepared by desilication using the same amount and the concentration of NaOH solution.

Three cases of the diffusion paths were considered: the mordenite channel connects (i) one mesopore with the external surface of the crystal, (ii) two mesopores, (iii) two external surfaces (i.e. the diffusion path 80 nm) if there is no mesopore present [41]. One million simulations using a pseudo-random number generator yielded the diffusion paths of 42 and 39 nm for the mesopores of the 8 and 4 nm diameters, respectively. The diffusion path depends only slightly on the diameter of the mesopores since only approximately 15% of the crystal is removed and a majority of the crystal is not influenced by the mesopores.

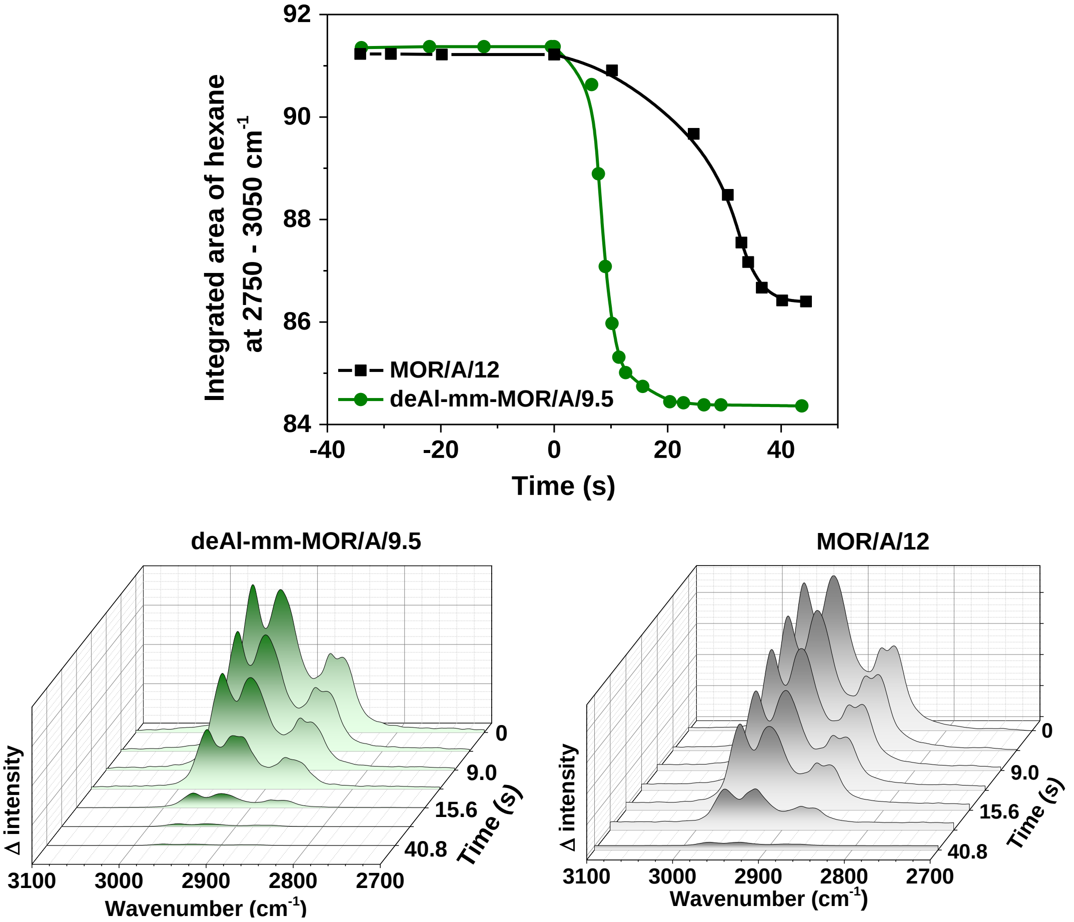

Figure 14. Desorption of *n*-hexane initiated by changes in the *n*-hexane partial pressure from 2.5 to 1.5 Torr analysed by FTIR spectroscopy.

The series of FTIR spectra recorded during transient desorption of *n*-hexane induced by a very fast decrease in the partial pressure of *n*-hexane from 2.5 to 1.5 Torr are shown for MOR/A/12 and deAl-mm-MOR/A/9.5 in Figure 14. The partial pressure 1.5 Torr provides the loading of one *n*-hexane molecule per acid site while *n*-hexane molecules weakly interacting with the inert channel walls are also present at the partial pressure 2.5 Torr. Under such decrease in the partial pressure, the changes in transport can be associated with the alterations of the pore structure rather than with desorption of *n*-hexane from the acid sites [41]. The higher desorption rate observed for the micro-mesoporous deAl-mm-MOR/A/9.5 compared to microporous MOR/A/12 is thus consistent with the effective reduction of the crystal domain by the introduction of the mesopores communicating with both the micropores and connected with the external surface. The enhanced transport in the micro-mesoporous zeolite can be, however, also affected by a contribution from a complex interplay of changes in the local structure of microporous channels and the channel openings [70].

4.1.2 Hydroisomerization of *n*-hexane using micromesoporous mordenite zeolite

Figure 15 depicts the yields of branched hexane isomers (2-methylpentane, 3-methylpentane, 2,2-dimethylbutane and 2,3-dimethylbutane) and C_1-C_5 by-products (methane, ethane, propane, butanes and pentanes) as a function of the reaction temperature in the hydroisomerization of *n*-hexane over the microporous and micro-mesoporous Pt/H-MOR zeolites. The yields of the individual products at 225 and 250 °C are listed in Table 6. With microporous MOR/A/12, the conversion first started to increase at a temperature of approximately 150 °C and reached a maximum of 58% at approximately 275 °C before declining again due to non-selective cracking reactions, as is indicated by the steadily increasing conversion of *n*-hexane and yield of C_1-C_5 by-products.

4.1.2.1 Hydroisomerization over desilicated and partially dealuminated-desilicated mordenites (series I)

The desilication of the parent sample (Figure 4) resulted in little improvement in conversions over the entire temperature range, passing through a maximum at 250 °C with the yields increasing from 53.0 to 59.2% and from 9.6 to 11.5% for all the branched and di-branched hexanes (Table 6), respectively, then declining due to non-selective cracking at higher temperatures. The catalytic behaviour of the mm-MOR/A/8 sample is in accordance with the findings of Monteiro et al. [71], showing that the desilication of mordenite zeolite does not significantly improve the catalytic efficiency of the mordenite zeolites.

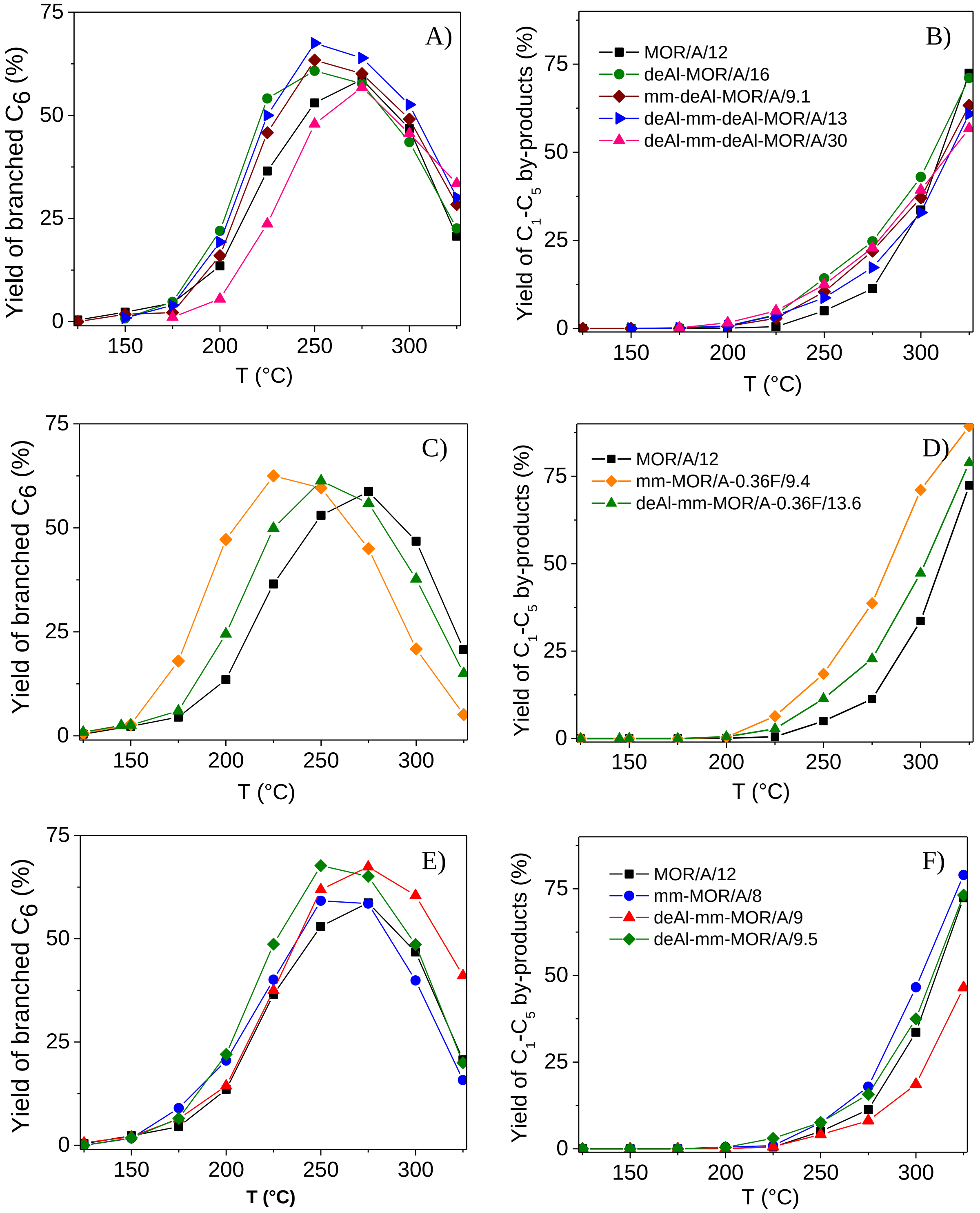

Figure 15. The yields of branched C_6 isomers and C_1-C_5 by-products in the hydroisomerization of *n*-hexane over Pt/H-MOR zeolites. A, B) Series I.; C, D) Series II.; and E, F) Series III.

With the deAl-mm-MOR/A/9 sample obtained by the removal of extraframework Al from mm-MOR/A/8 using oxalic acid (Figure 4, I. series), the formation of by-products at high temperatures was significantly reduced compared to mm-MOR/A/8 or microporous MOR/A/12 samples and was accompanied by a corresponding increase in the yield of the desired branched isomers, reaching a maximum of 67.4% at 275 °C. The deAl-mm-MOR/A/9 sample is characterised by shortened 12-ring channels due to well-developed secondary mesoporous structure, but without significantly enhanced accessibility of the OH groups compared to the parent zeolite (Table 5).

It seems that the shortening of the main channel and a larger number of channel openings provide only a slight increase in activity, but lead to a significant increase in selectivity limiting the non-selective subsequent cracking reactions and consequently increasing the yield of desired products at higher temperatures [41].

The deAl-mm-MOR/A/9.5 sample dealuminated by nitric acid (Figure 4, I. series) provides higher yields of branched isomers compared to MOR/A/12 and mm-MOR/A/8 zeolites with similar yields of by-products (Figure 14). As the difference between deAl-mm-MOR/A/9.5 and deAl-mm-MOR/A/9 lies mainly in significantly higher accessibility of the OH groups (Table 5), the improvements in the yields of branched isomers at lower temperatures, e.g. from 53% to 67.7% at 250 °C, can be associated with greater accessibility of the acid sites, and the improvements in the yield at higher temperatures, e.g. from 58.7 to 67.4% at 275 °C, also with the shortened main channels and larger number of channel openings. Thus the use of the deAl-mm-MOR/A/9.5 sample had a positive effect on the yield of branched isomers in the whole temperature region. The improvements in the catalytic properties are minor, however, clearly indicating a potential for improvements in the functionality of hydroisomerization mordenite catalysts via enhanced accessibility of active sites and transport of reactants in the micro-mesoporous structure.

The durability and stability of the catalytic activity for the deAl-mm-MOR/A/9.5 as a representative micro-mesoporous Pt/H-MOR zeolite were analysed under the reaction conditions. Stable values of the yields of mono- and di-branched isomers ∼55% and ∼9%, respectively, and by-products ∼1% as a function of time-on-stream were obtained over deAl-mm-MOR/A/9.5 at 235 °C for 72 h indicating a sufficient structural stability and no deactivation of the micro-mesoporous Pt/H-MOR (Figure 16).

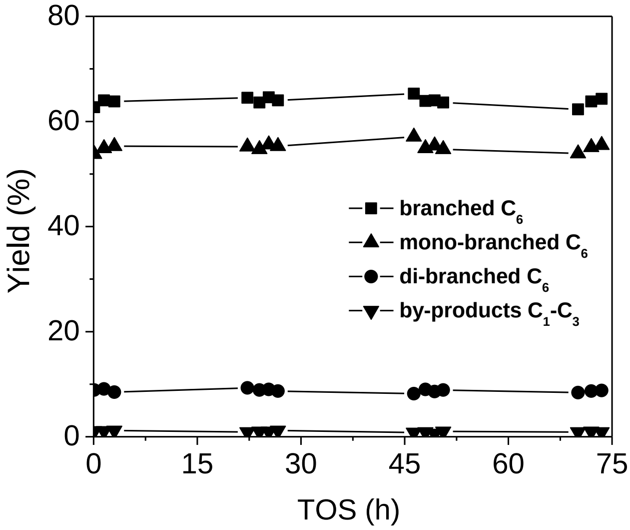

Figure 16. Dependence of the yield of branched hexane isomers and C_1-C_3 by-products on time-on-stream (TOS) in hydroisomerization of *n*-hexane over deAl-mm-MOR/A/9.5 at 235 °C.

4.1.2.2 Hydroisomerization over partially dealuminated and acid-alkaline-acid treated mordenites (Series II)

Figure 15C shows the yields of branched isomers as a function of temperature obtained over dealuminated deAl-MOR/A/16 and zeolites prepared by subsequent desilication and desilication/dealumination of the deAl-MOR/A/16 sample. Although the dealumination of mordenite (deAl-MOR/A/16) leads to a decrease in the concentration of Brønsted sites from 1.06 to 0.47 mmol.g^{-1}, the accessibility of the remaining acid sites was significantly enhanced, with ~ 92% Brønsted sites accessible for *n*-hexane (Table 5). Less than half the concentration of Brønsted sites in deAl-MOR/A/16 provided yields of branched hexanes which outperform the microporous MOR/A/12, cf. e.g. the yields of branched hexanes 36.5% and 54.1% at 225 °C for MOR/A/12 and deAl-MOR/A/16, respectively. The higher specific activity of acid-treated partially dealuminated mordenites has been well documented in the literature [72] and explained by the beneficial effects on the textural properties of extraction of part of the framework Al atoms by acid treatment, leading to improved accessibility of highly active acid sites located in the 8-ring side pockets [25, 73]. Desilication of the deAl-MOR/A/16 sample yielded micro-mesoporous mm-deAl-MOR/A/9 (Figure 4), which showed no significant changes in the yields of the branched isomers, nor by-products. The positive impact of the development of the mesoporous volume (0.11 cm^3.g^{-1}) was probably offset by the negative impact of the decline in the microporous volume because of its partial blockage [41]. The subsequent partial dealumination of mm-deAl-MOR/A/9 provided the deAl-mm-deAl-

MOR/A/13 sample with well-developed mesoporous structure and with similar concentration and accessibility of the OH groups for *n*-hexane as the deAl-MOR/A/16 sample. The similar concentrations and accessibility of the OH groups for *n*-hexane in the deAl-MOR/A/16 and deAl-mm-deAl-MOR/A/13 samples (Table 5) resulted in similar yields of branched hexane isomers at ≤ 225 °C (Table 6). The presence of mesoporous structures in deAl-mm-deAl-MOR/A/13 caused a slightly lower formation of cracking products and a corresponding increase in the yield of branched hexanes at higher temperatures ≥ 250 °C.

4.1.2.3 Hydroisomerization over fluorinated-alkaline treated mordenites (Series III)

The yields of branched C_6 isomers in the hydroisomerization with microporous MOR/A/12 without postsynthesis treatment were very low at temperatures ≤ 200 °C (Figure 17). The yields were increased considerably over the mm-MOR/A-0.36F/9.4 sample, e.g. from 13.5% to 47.2% at 200 °C, showing that the desilication of fluorinated mordenite zeolite markedly increased the catalytic activity (Figure 15E). This was accompanied by higher yields of di-branched isomers (Table 6) and high selectivity without the detectable formation of C_1-C_4 by-products at ≤ 200 °C (Figure 15F). In comparison with other micro-mesoporous Pt/H-MOR, the mm-MOR/A-0.36F/9.4 sample provides the greatest enhancement of the yields of branched C_6 isomers achieved at low temperatures (Figure 17). The chemical analysis showed the absence of fluorine in the mm-MOR/A-0.36F/9.4 treated after fluorination by desilication, triple ion-exchange with large excess of NH_4NO_3 solution and calcination in the air and subsequently in a hydrogen atmosphere. The enhancement in the activity is thus associated with the micro-mesoporous structure providing high concentration of Brønsted sites (c_B 0.6 mmol.g^{-1}) readily accessible for n-hexane molecules (> 90%), (Table 5).

To exclude a possible effect of traces of fluoride not detectable by the chemical analysis on the increase in activity, a fluorinated sample of Pt/H-F-ZSM-5 zeolite with small crystals was prepared and its activity was compared with Pt/H-ZSM-5. The intra-crystalline diffusion does not affect the overall reaction rates for ZSM-5 for both the *n*-hexane hydroisomerization [74] and cracking [75]. Accordingly, we observed very comparable yields of branched C_6 isomers over Pt/H-ZSM-5 and its fluorinated analogue Pt/H-ZSM-5-F in the entire temperature region (Figure 18). Thus, the high concentration of the Brønsted sites located in non-restricted micropores highly accessible via new channel openings in small mesopores formed by the simultaneous removal of Si and Al atoms results in significantly improved catalytic properties enabling the reaction at lower temperatures [41].

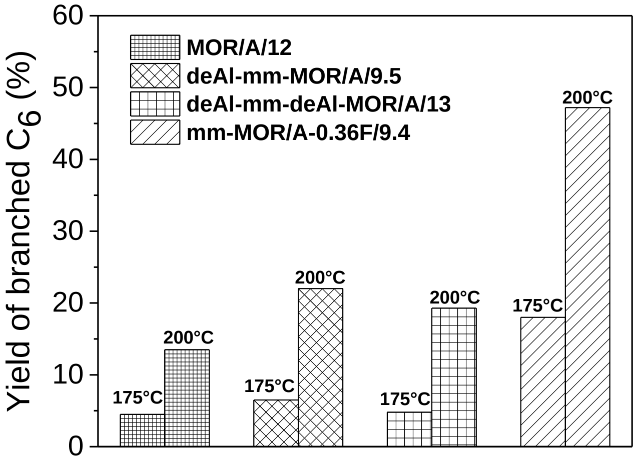

Figure 17. Comparison of the effects of the postsynthesis alkaline-acid (Pt/H-deAl-mm-MOR/A/9.5), acid-alkaline-acid (Pt/H-deAl-mm-deAl-MOR/A/13), and fluorination-alkaline (Pt/H-mm-MOR/A-0.36F/9.4) treatments on the yields of branched hexanes at 175 and 200 °C.

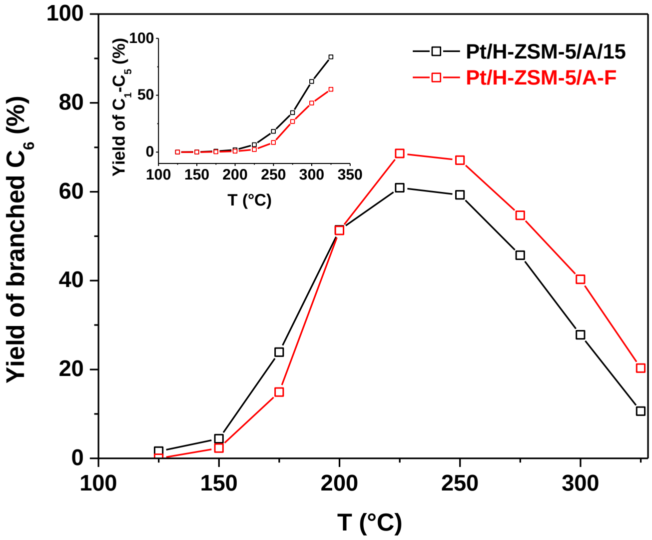

Figure 18. The yields of branched C_6 isomers and C_1-C_5 by-products in the hydroisomerization of *n*-hexane over Pt/H-ZSM-5/A/15 and its fluorinated analogue Pt/H-ZSM-5/A-F.

Table 6. The yields of branched hexane isomers and lower molecular weight by-products for hydroisomerization of *n*-hexane over microporous and micro-mesoporous Pt/H-MOR at 225 °C and 250 °C.

Sample	$\Sigma y_{iso\text{-}C6}$ (%)		2,2-dimetyl-		2,3-dimetyl-		2-metyl-		3-metyl-		C_1-C_5 (%)	
	225 °C	250 °C	225 °C	250 °C	225 °C	250 °C	225 °C	250 °C	225 °C	250 °C	225 °C	250 °C
Pt/H-MOR/A/12	36.5	53.0	1.6	3.6	6.0	6.0	7.3	8.4	21.6	35	0.5	5.3
Pt/H-mm-MOR/A/8	40.1	59.2	2.5	5.2	5.2	6.3	7.9	8.6	24.5	39.1	0.9	7.5
Pt/H-deAl-mm-MOR/A/9	37.5	61.9	2.1	5.4	4.7	6.7	8.7	8.7	22.0	41.1	0.6	4.1
Pt/H-deAl-mm-MOR/A/9.5	48.7	67.7	1.8	5.7	6.1	7.3	8.8	10.5	32.0	44.2	3.0	7.6
Pt/H-deAl-MOR/A/16	54.1	60.8	2.9	4.9	6.1	6.8	11.2	11.3	33.9	37.8	3.9	16
Pt/H-mm-deAl-MOR/A/9.1	45.8	63.4	2.8	8.1	4.5	6.5	8.6	8.6	29.9	40.2	2.9	10.4
Pt/H-deAl-mm-deAl-MOR/A/13	50.0	67.5	2.4	6.3	5.0	7.4	8.2	10.0	34.4	43.8	3.7	8.7
Pt/H-deAl-mm-deAl-MOR/A/30	23.7	47.9	0.6	3.5	1.3	4.2	7.3	8.4	14.5	31.8	5.0	12.4
Pt/H-mm-MOR/A-0.36F/9.4	62.5	59.6	4.9	7.4	7.4	6.2	8.6	8.4	41.6	37.6	6.4	18.5

4.2 Enhancement of accessibility of acid sites in supermicroporous zeolite

In this study, the mordenite zeolites (Figure 5) with enhanced activity for hydroisomerization of *n*-hexane containing a high concentration of aluminium and corresponding concentration of acid sites readily accessible for the hexane molecules were prepared. For this purpose, structure of mordenite zeolite with a high content of lattice aluminium (Si/Al 5.8) (Table 2) was modified by postsynthesis concurrent extraction of Si and Al atoms from the framework using fluorination-alkaline-acid treatments (Figure 20). This modification provides an increase in the dimensions of the channel openings, enlargement of the micropores, 3D interconnection of the micropores as well as the formation of acidic sites with enhanced activity. The combination of the supermesoporosity and the occurrence of highly active acidic sites dramatically increases the activity of mordenite zeolites in the hydroisomerization of *n*-hexane to the branched isomers. The high activity shifts the window of operating temperatures to the thermodynamically more suitable area for the formation of di-branched isomers [42].

4.2.1 Structural analysis of supermicroporous structure in mordenite zeolites

4.2.1.1 Formation of supermicroporous structure in mordenite zeolites

The well-developed crystalline structure of parent MOR/B/5.8 is manifested by smooth lattice fringes in a representative HR-TEM image (Figure 19), high intensities of the characteristic lines in the X-ray diffractogram (Figure 22), a micropore volume of 0.16 $cm^3.g^{-1}$ (Table 7) and size distribution of the micropores corresponding to the mordenite structure (Figure 21).

Fluorination-alkaline treatment (Figure 20) resulted in slight decrease in the intensity of the diffraction lines associated with reducing the density of the structural framework and slight roughness of the lattice fringes of the crystalline structure in the HR-TEM images. Use of fluorination-alkaline treatment with concentrations of 0.36 M NH_4F in the Ist and 0.5 M NH_4F in the IInd series resulted in an increase in the micropore volume (Table 7) to about 0.2 $cm^3.g^{-1}$, with a further increase after mild dealumination to 0.23 and 0.24 $cm^3.g^{-1}$, respectively, with only a minor creation of mesopores with a volume of 0.05 and 0.06 $cm^3.g^{-1}$, respectively, also visible at the HR-TEM images.

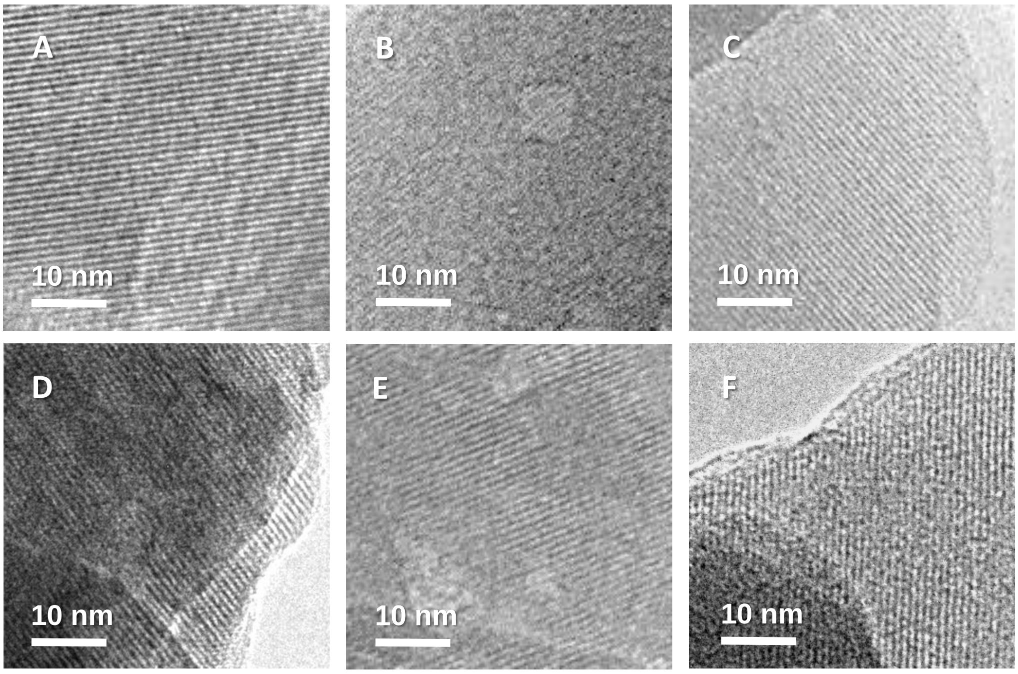

Figure 19. Representative HR-TEM images of A) parent MOR/B/5.8 mordenite, B) MOR/B-0.36F/5.8, C) deAl-MOR/B-0.36F/7.0, D) MOR/B-1F/5.4, E) deAl-MOR/B-1F/6.8, and F) deAl-MOR/B/6.6.

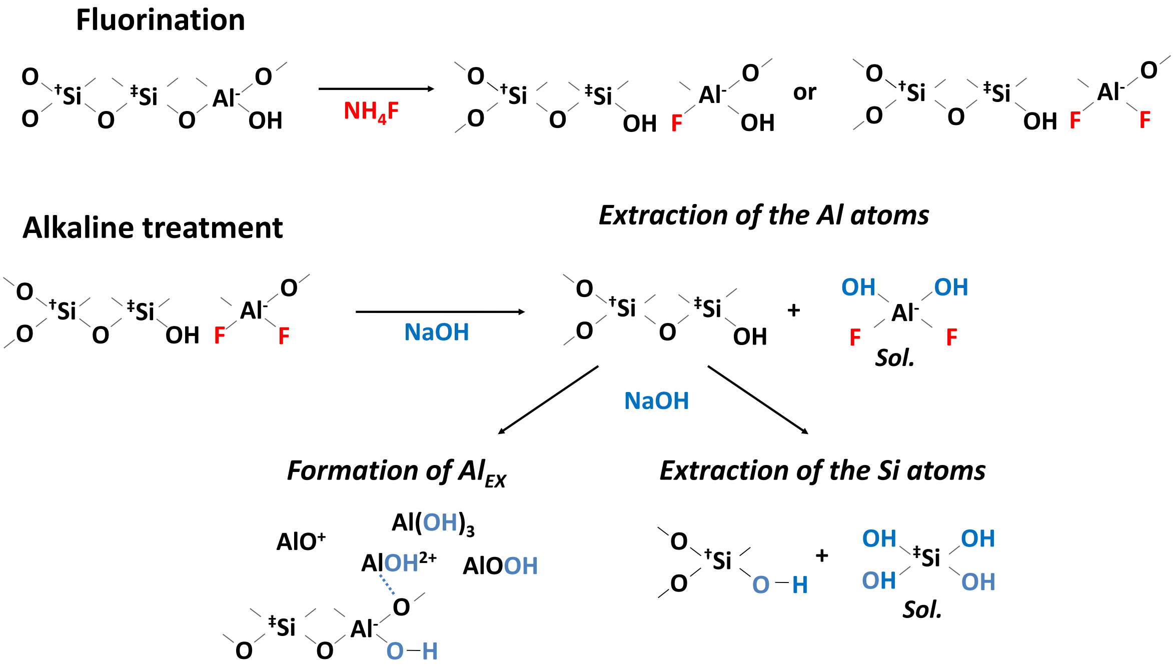

Figure 20. Illustration of mechanism of the simultaneous extraction of Al^{3+} and Si^{4+} atoms and formation of the extraframework Al species by alkaline treatment of fluorinated Al-rich mordenites.

In the first series (Figure 5), the micropore volume is increased mainly by an increase in the number of micropores with dimensions of about 0.7 nm. This enhancement could be ascribed to enlargement of the narrow openings of the 8-ring channels [42]. It is also reflected in an increase in the accessibility of the OH groups in the 8-ring channels for the *n*-hexane molecule in the originally inaccessible pores (see FTIR analysis par. 4.2.1.2). In the IInd series, the mean pore diameter of the micropores is also increased. The procedure using the fluorination-alkaline treatment was developed by Yu et al.[44] to form a micro-mesoporous structure in the ZSM-5 zeolite with relatively high content of Al in the framework Si/Al ~ 15. The introduction of NH_4F into microporous ZSM-5 zeolite leads to the formation of F-bearing tetrahedral Al species which are readily dislodged in the subsequent alkaline treatment [44] leading to concurrent extraction of Al and Si. We demonstrated the development of secondary mesoporosity and preservation of microporosity via concurrent extraction of SiO_2 and a smaller amount of Al using the fluorination-alkaline treatment of MOR zeolite Si/Al ~ 12 in our study [46].

Table 7. Preparation and textural properties of fluorinated Al-rich mordenites determined by adsorption of N_2 and Ar at the temperature of liquid nitrogen.

Sample	Si/Al[a]	V_{MI}^{b} $(cm^3.g^1)$	V_{ME}^{c} $(cm^3.g^1)$	S_{EXT}^{b} $(m^2.g^{-1})$
MOR/B/5.8	5.8	0.16	0.02	23
MOR/B-0.36F/5.8	5.7	0.21	0.04	40
deAl-MOR/B-0.36F/7.0	7.2	0.21	0.05	51
MOR/B-0.5F/5.6	5.6	0.20	0.05	63
deAl-MOR/B-0.5F/5.6	6.5	0.23	0.06	57
MOR/B-1F/5.4	5.4	0.12	0.06	65
deAl-MOR/B-1F/6.8	6.8	0.24	0.06	68
MOR/B-4F/6.2	6.2	0	-	-
deAl-MOR/B-4F/6.9	6.9	0.12	-	18
deAl-MOR/B/6.6	6.6	0.15	0.04	44

[a] *from chemical analysis*

[b] *estimated from BdB t-plot method*

[e] *Vmeso = Vtotal - Vmicro*

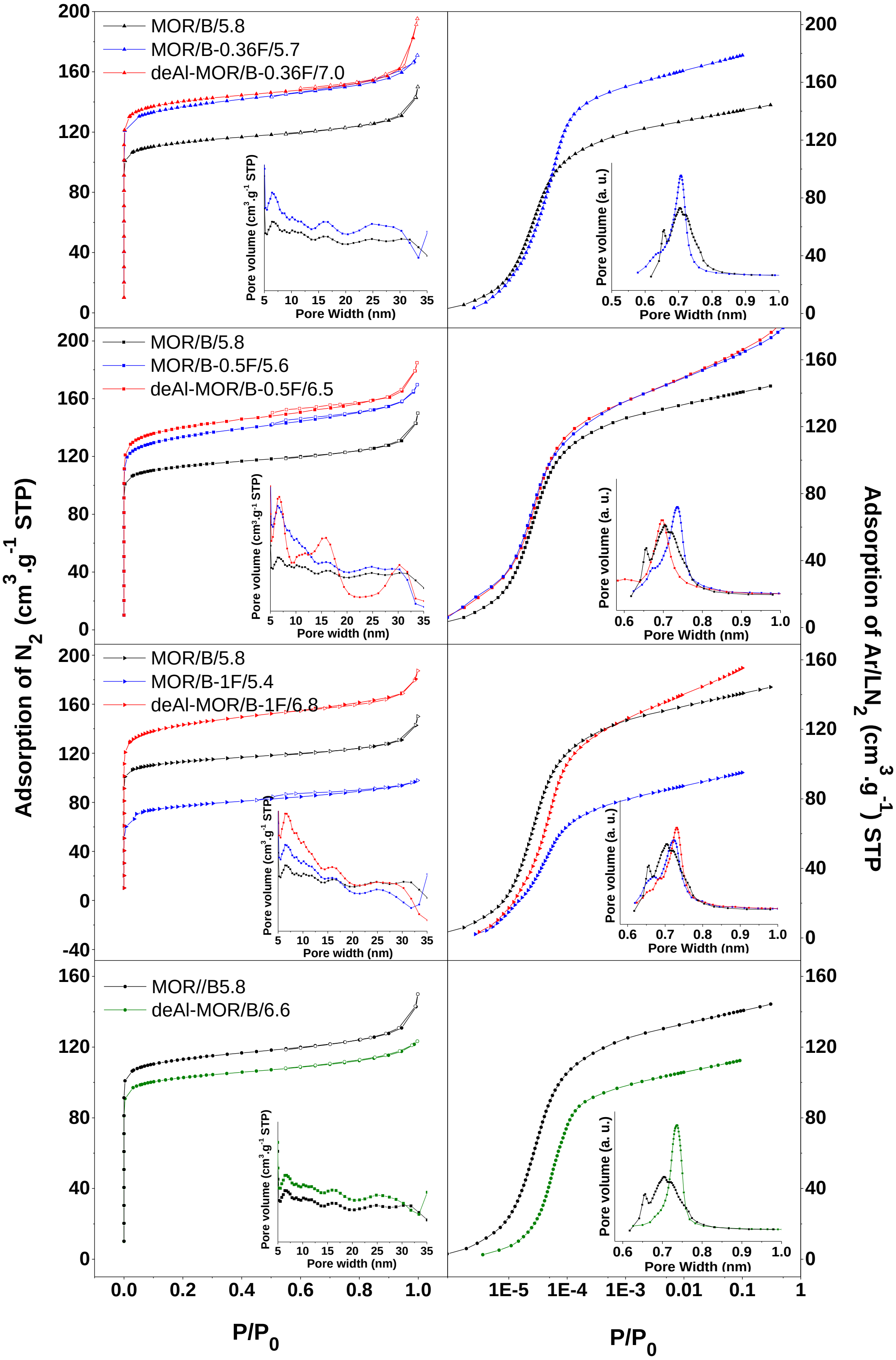

Figure 21. Adsorption of N_2 and Ar/LN$_2$ at 77 K and detail of distribution of microporous and mesoporous structure before and after fluorination-alkaline-acid treatments (Series I - III), and also simple acid (Series V) treatment.

The significant increase in the micropore volume, the increase in the size of some micropores and only minor formation of mesopores observed for the samples in series I and II prepared from Al-rich MOR (Si/Al ~ 5.8) (Table 7) show that the high concentration of Si-O-Al in the framework increases the resistance to alkaline treatment, as also reported for ZSM-5 [76]. The degree of susceptibility of the parent MOR/B/5.8 zeolite towards alkaline leaching after fluorination results in controlled concurrent extraction of both Al and Si atoms, indicated by comparable Si/Al composition before and after leaching (Table 7), leading to desirable development of microporosity without excessive formation of mesopores. The effect of the extraction of two neighbouring Al and Si atoms from the walls of the zeolite channels of MOR zeolite on the micropore structure is illustrated in Figure 23A (for analysis of the local changes in the structure, see par. 4.2.1.2). It is obvious that the simultaneous extraction of Al and Si pairs from the MOR framework leads to enlargement and interconnection of the micropores (Figure 5 and Figure 19). The fluorination-alkaline treatment with a concentration of 1M NH_4F resulted in a decrease in the micropore volume compared to the parent zeolite, but the subsequent mild acid leaching increased the micropore volume to 0.24 $cm^3.g^{-1}$. The preserved lattice fringes in the HR-TEM images and the intensity of X-ray diffraction pattern of the zeolite after the fluorination-alkaline treatment are indicative of the preservation of the crystalline structure (Figure 22). Previous studies showed that hydrolysis of framework Al at harshened conditions of desilication lead to formation of extraframework Al species which can easily block the openings the pseudo-monodimensional channel structure of MOR [38, 46]. A slight increase in the molar Si/Al ratio (Table 7) and the significant increase in the micropore volume after the mild acid leaching indicate that the extraframework Al blocking part of the micropores was removed. The size distribution of micropores shows a further increase in their dimensions associated with supermicroporosity and 3D interconnection of the monodimensional mordenite channels [25, 41, 52, 77-78].

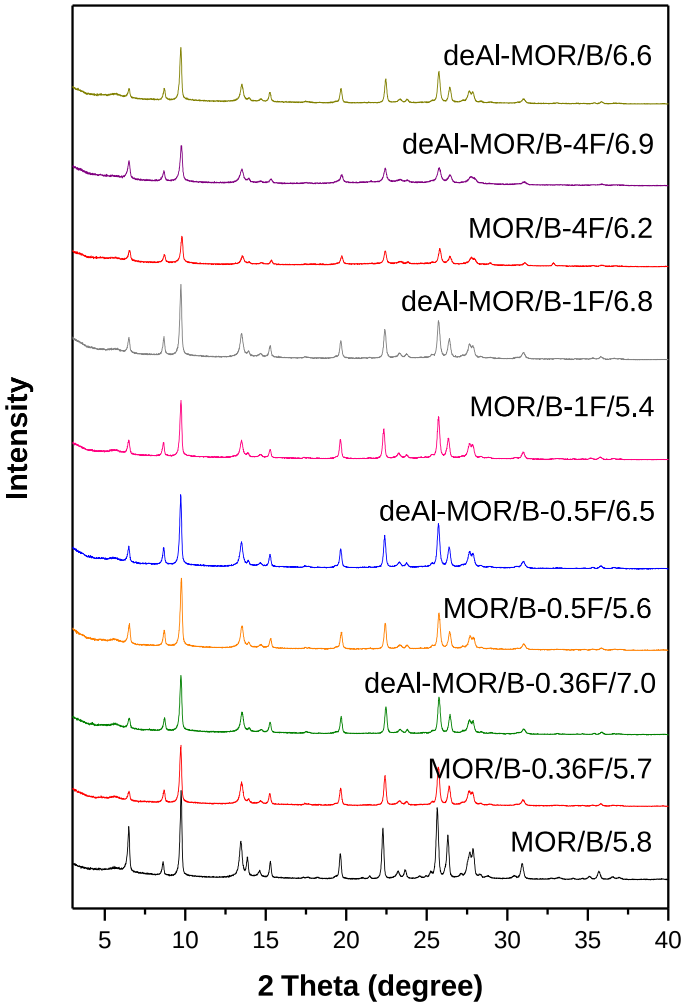

Figure 22. XRD patterns of prepared MOR samples.

The harshest fluorination treatment by 4 M NH_4F in the IVth series (Figure 5) has led to partial destruction of crystalline structure displayed by a significant decrease in XRD intensity, negligibly low adsorption of N_2 in fluorination-alkaline treated sample MOR/B-4F/6.2 and only partial restoration of the micropore volume of deAl-MOR/B-4F/6.9 after mild acid treatment (Table 7). The V. series was prepared by acid treatment of MOR/B/5.8 providing mildly dealuminated deAl-MOR/B/6.6 (Figure 5). The size distribution of micropores determined by Ar adsorption (Figure 21) clearly show their enlargement compared to MOR/B/5.8. The increase in the sizes and improvement of the connectivity of the micropore channels given by the extraction of Al from the framework have been described in the literature [21, 25, 52]. An addition to these desirable structural changes, a small decrease in the micropore volume could indicate a partial blockage of some micropores [42].

The adsorption measurements supplemented by the HR-TEM images (Figure 19) and the X-ray diffractograms (Figure 22) show the concurrent extraction of Al and Si by fluorination-alkaline-acid treatment of Al-rich MOR essentially alters the monodimensional structure with low accessible side pockets into supermicropore channel structure (Figure 23) characterised by high micropore volume (up to 0.25 ml .g^{-1}) formed by accessible internal voids with mean diameter about 7.5 Å.

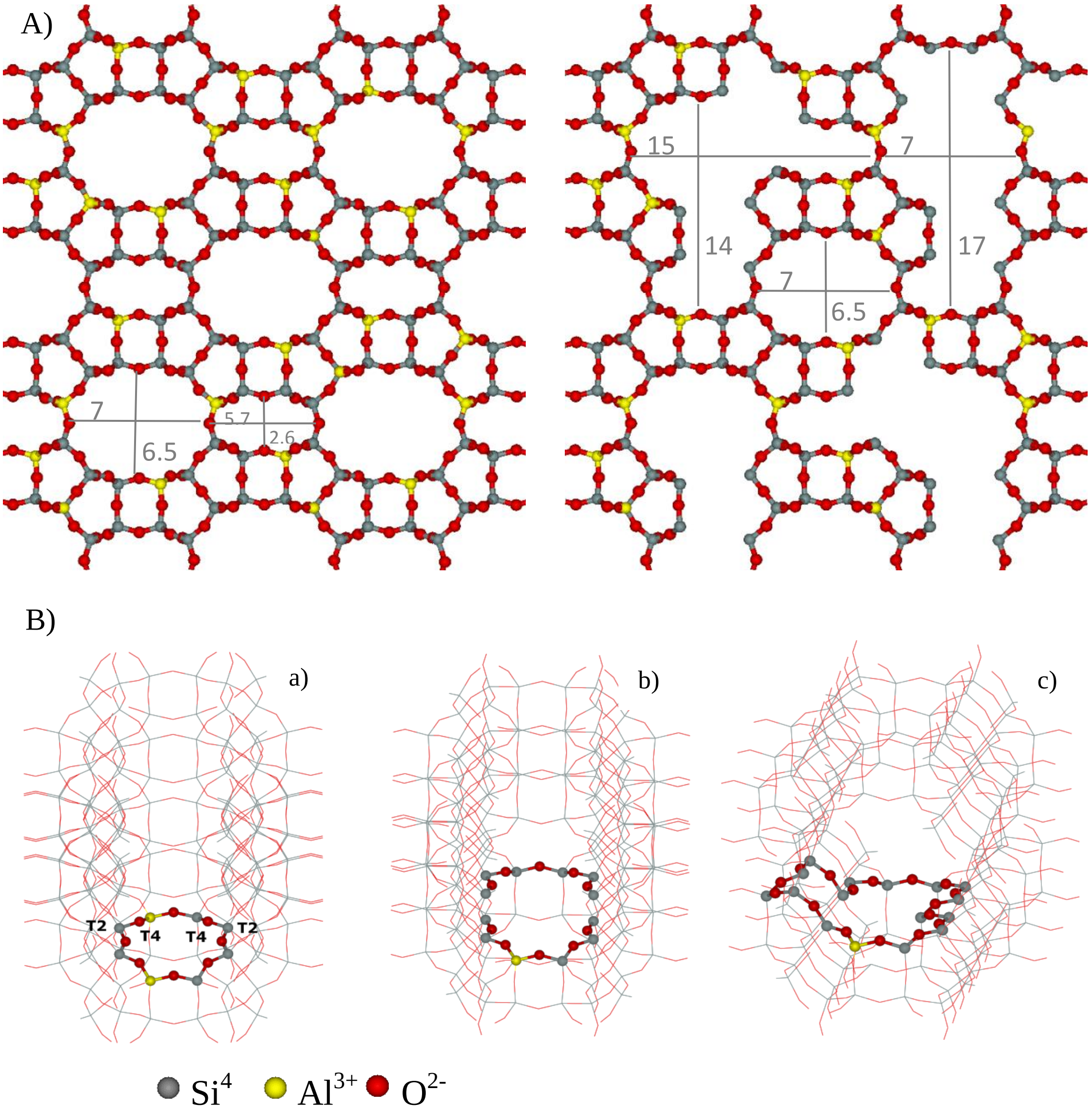

Figure 23. Schematic illustration of mordenite openings before and after extraction of Si and Al by fluorination-alkaline-acid treatments. A) Illustration of pore size changes and B) structure of the 8-ring a) before the treatment and an illustration of the changes in local arrangements after extraction of Al from the T4 site and a neighbouring Si atom from b) the T2 or c) the T4 site.

4.2.1.2 Concentration, nature and accessibility of acid sites in supermicroporous mordenites

Figure 24 compares the ^{27}Al MAS NMR spectra of MOR zeolites (Table 7) before and after fluorination-alkaline-acid (Series I - III) and acid (Series V) treatments. A symmetric signal at 56 ppm associated with tetrahedrally coordinated aluminium (Al_{Td}) in the zeolite framework is observed in the ^{27}Al MAS NMR spectrum of the parent MOR/B/5.8 sample. The high symmetry of the signal is a result of the symmetric local environment of the tetrahedral framework Al sites in the hydrated zeolite mitigating the quadrupolar couplings. The postsynthesis fluorination-alkaline and acid leaching lead to broadening and a shift of the maxima of the main signal to approx. 54 ppm, the formation of an asymmetric signal of high intensity at about 40 ppm, a barely visible signal of weak intensity at 30 ppm, and the appearance of a signal at 0 ppm. The shift in the maximum of the signal of the Td coordinated Al is an indication of the preferable extraction of Al atoms located in specific T sites. This interpretation is consistent with previous studies of the acid leaching of MOR zeolites, which exhibited preferential dealumination of the T4 site [66-68]. In the literature [38, 46, 55, 57, 59, 79-82] the signal at about 40 ppm is ascribed to perturbed Al in the framework in a less ordered environment and/or Al species partly removed from the framework. The combination of ^{27}Al {^{1}H} REDOR (3Q) MAS NMR and ^{27}Al {^{1}H} CP (3Q) MAS NMR experiments and DFT/Molecular computations in previous study [80] showed that the shoulder at 40 ppm is associated with a perturbed framework Al in the $(SiO)_3AlOH$ groups ($\delta i = 59 – 62$ ppm, CQ = 5 MHz, and $\eta = 0.3 – 0.4$). A low local symmetry of the group results in the appearance of a highly asymmetric signal visible as a shoulder of the main signal. The weak signal observed around 30 ppm was assigned to traces of penta-coordinated extra-framework Al species [83]. The signal at 0 ppm is associated with octahedrally coordinated extra-framework Al. The perturbed framework tetrahedrally coordinated Al, the penta-coordinated and tetrahedral extra-framework Al manifested in the shoulder at 40 ppm and the signals at 30 and 0 ppm, respectively, were often observed in faujasite or high-silica zeolites after steaming [54-59]. The penta-coordinated and octahedral extra-framework Al could be present in the form of positively charged oxo/hydroxo moieties ($AlO^+ \cdot nH_2O$, $AlOH^{2+} \cdot nH_2O$) compensating the negative charge of the MOR framework or $Al(OH)_3 \cdot nH2O$, $Al_2O_3 \cdot nH_2O$, $AlOOH \cdot nH_2O$ neutral species (Figure 5) [84]. The changes observed in the spectra after the fluorination-alkaline treatment are thus associated with partial extraction of Al from the framework preferentially from the T4 sites, the formation of a significant proportion of perturbed framework Al in the $(SiO)_3AlOH$ groups and the formation of a limited amount of extra-framework Al species of various structures. Comparison of the ^{27}Al MAS NMR spectra of the samples from the series I to series III, prepared with increasing concentrations of the agents used for fluorination-alkaline treatments (Figure 24), reveal a considerable increase in the intensity of the shoulder at about 40 ppm and broadening of the signal at 0 ppm with the harshness of the treatment, indicative of an increase in the proportion of the perturbed framework Al in the $(SiO)_3AlOH$ groups and higher distortion of the local environment of the extra-framework Al species, respectively [42].

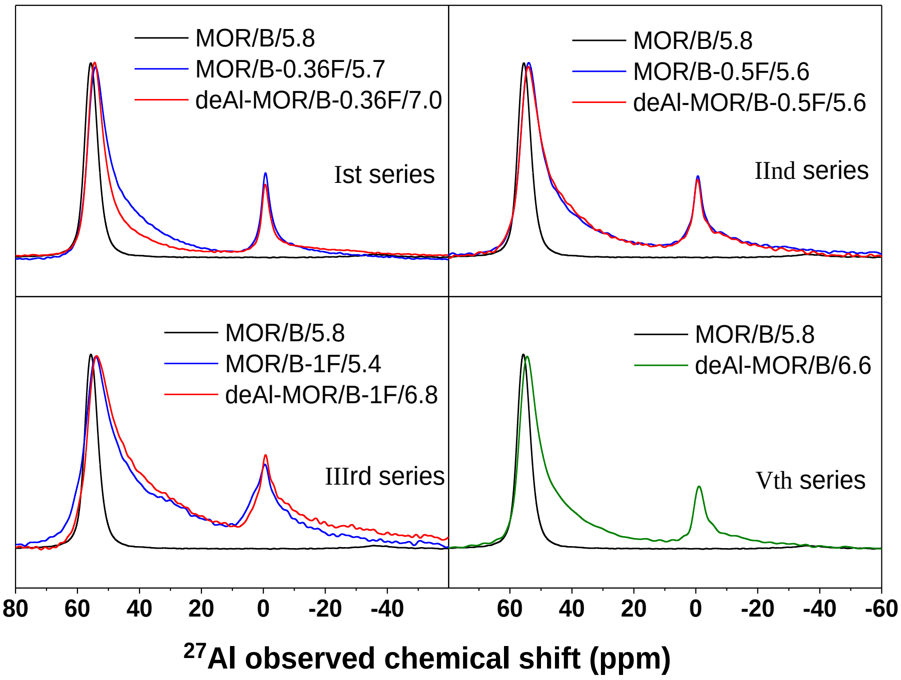

Figure 24. ^{27}Al MAS NMR spectra for hydrated mordenite zeolites after fluorination-alkaline-acid treatments (Series I - III), and also simple acid (Series V) treatment.

Similar changes in the ^{27}Al MAS NMR spectra of MOR/B/5.8 after acid leaching (deAl-MOR/B/6.6, Figure 5, Series V) and those observed after fluorination-alkaline treatments (Series I - III) indicate the formation of similar Al species after both the fluorination-alkaline treatment and the acid treatments. The decrease in the Al concentration (Table 7) and lowering in the intensity of the bands of the perturbed and extra-framework Al in the spectra of the acid-treated deAl-MOR/B-0.36F/7.0 sample compared to MOR/B-0.36F/5.7 (Figure 5, series I) clearly show that the acid leaching results in concurrent dislocation of the framework Al and extraction of all the defective forms of the Al species from the zeolite. The gradual dislocation and extraction of Al from the zeolite framework and related structural changes in MOR zeolites by acid treatment have been described in detail in the scientific literature [21, 25, 52].

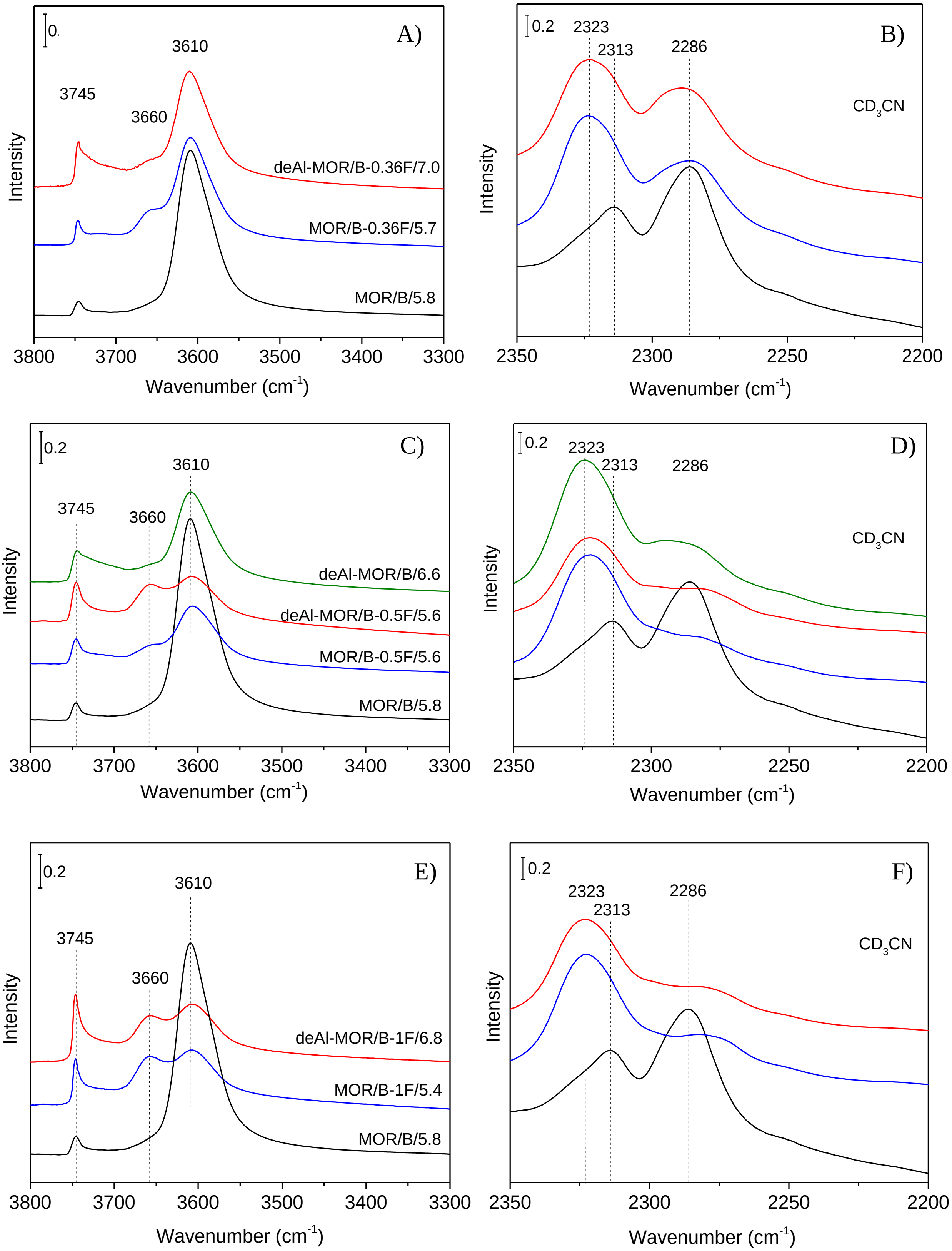

Figure 25. Comparison of FTIR spectra of adsorbed *d*$_3$-acetonitrile (B, D, and F) and the OH stretching region (A, C, and E) for mordenite zeolites after fluorination-alkaline-acid treatments (Series I - III), and acid (Series V) treatment. A), B) Series I; C, D) Series II and V, and E, F) Series III.

Figure 25 presents the FTIR spectra of MOR zeolites before and after fluorination-alkaline-acid treatment (Series I - III), and also simple acid (Series V) treatments, as manifested before and after *d*3-acetonitrile adsorption experiments. The spectra of the samples of all the series display a typical asymmetrical shape of the band in the OH region with a dominant band at 3610 cm^{-1} and a clearly defined sideband at lower wavenumbers. This shape of the spectra, characteristic for MOR, was already explained by Wakabayashi et al. [50] and Zholobenko et al. [48] and assigned to an OH bond located in the main 12-ring channels, and the low- frequency component near 3590 cm^{-1} was attributed to OH in the smaller side pockets with an 8-ring, and connected with the T3 site [50]. Further analysis proved this interpretation and some effort was devoted to use this analysis for semi-quantitative evaluation of both structures. Despite some controversies in this respect, we used the recommendation of Makarova [48] for the semi-quantitative evaluation, yielding a ratio of extinction coefficients of the 12 OH / 8 OH bands of about 1.5. Semi-quantitative analysis of the acidity of the analyzed samples was based on the results of the *d*3-acetonitrile adsorption experiments, using the extinction coefficient for *d*3-acetonitrile interacting with the Lewis acid sites as ε_L = 3.60 cm.µmol^{-1}, and ε_B = 2.05 cm.µmol^{-1} for *d*3-acetonitrile interacting with the OH [45].

The FTIR spectra of the parent MOR/B/5.8 sample represent typical spectra of well-developed MOR zeolites with relatively high-intensity bands in the region of the Brønsted OH, with a dominant band at 3610 cm^{-1}, i.e. at the position of OH situated in the 12-ring, and the relatively less intense side band at 3590 cm^{-1} of the OH in the 8-ring. Based on the quantitative analysis, the relative content of the two 12 OH / 8 OH structures in the parent zeolite was about 2. The small intensity of the band of the terminal OH (a band at about 3745 cm^{-1}) and negligible structure indicated at the position typical of AlOH with the band at 3660 cm^{-1} further demonstrated the regularity of the parent MOR. The results of the adsorption of *d*3-acetonitrile (Figure 25B, D, F) provided data for semi-quantitative evaluation of the Brønsted (a band at 2286 cm^{-1}) and two distinguished Al-related Lewis acid sites (with bands at 2313 and 2323 cm^{-1}). Analysis of the spectra in the OH region demonstrated that, after the *d*3-acetonitrile adsorption/partial desorption procedure, most of the terminal SiOH were free of the *d*3-acetonitrile while, at the same time, full interaction with both the OH groups located in the 12-ring and 8-ring was achieved. Accordingly, the *d*3-acetonitrile spectra could have been used for the semi-quantitative analysis of the concentration of both OH and the Lewis sites. The relatively intense additional band at 2280 cm^{-1} with a shoulder at about 2277 cm^{-1} was assigned to the *d*3-acetonitrile molecule interacting with structurally undefined defects in the MOR structure and a small part of the terminal SiOH, not fully reconstructed during the mild desorption of the d_3-acetonitrile. It should be noticed that the band at 2280 cm^{-1} was much less intense in the previous experiments over MOR (Si/Al ~ 12) with lower Al content in the previous study [41].

Generally, all the MOR samples after the postsynthesis fluorination-alkaline (Figure 20) and acid leaching displayed some uniform features with a decrease in the total OH bands and well-expressed change in the relative ratio of the 12/8-ring structures. For all samples, the treatments led to a steep increase in the intensity of the Lewis band at about 2323 cm^{-1}. It seemed significant that both the acid (Figure 5, Series V) and combined treatments (Figure 5, Series I-IV) induced elimination of the 2280 cm^{-1} band, assigned to unspecified defect structures present in the parent zeolite [42]. Some indication on the presence and relative concentration of the AlOH structures indicated by the IR band in the 3 660 cm^{-1} region could be gained, suggesting the formation of this structure after the combined treatment and not fully regularly decreasing again after acid treatment. These results are to some extent consistent with previous studies on the acid leaching of MOR zeolites, which indicated preferential dealumination of the T4 site connected to the 12-ring [66-68] and accordingly relatively higher stability of the 8-ring sites, connected with T3 site [85]. The same could be indicated for the formation of the perturbed Al species, connected either to the Al-related Lewis positions or to the AlOH structure. All these structures could be regarded as perturbed Al sites in the framework in a less ordered environment and/or Al species partly removed from the framework [42].

The changes in the FTIR spectra (Figure 25) observed either before or after the d_3-acetonitrile adsorption/desorption cycle of the samples exposed to fluorination-alkaline treatment thus indicate partial extraction of Al from the framework preferentially from the 12-ring sites, and, formation of perturbed framework Al groups and some amount of extra-framework Al species, including Al-related Lewis species. Increasing the concentrations of the agents used for fluorination-alkaline treatments (Figure 24) led to an increase in the Al elimination process going from Series I to III. The change in the spectra of the MOR in Series V were rather similar, indicating similar production of Al species after both fluorination-alkaline treatment and acid treatments but with much smaller formation of the $(SiO)_3AlOH$ groups after acid treatment.

Table 8. Concentrations of bridging hydroxyls and Brønsted and Lewis sites in zeolite and accessibility of OH groups in fluorinated Al-rich mordenites.

Sample	Si/Al[a]	c_{Al} [a]	c_B [b]	c_L [c]	c_{B+2L} [d]	Accessibility of OH groups [f]
				(mmol.g^{-1})		(%)
MOR/B/5.8	5.8	2.31	0.97	0.45	1.86	19
MOR/B-0.36F/5.8	5.7	2.51	0.37	0.81	1.99	48
deAl-MOR/B-0.36F/7.0	7.2	2.05	0.55	0.75	2.04	51
MOR/B-0.5F/5.6	5.6	2.55	0.22	0.81	1.85	54
deAl-MOR/B-0.5F/5.6	6.5	2.24	0.17	0.47	1.11	78
MOR/B-1F/5.4	5.4	2.65	0.22	0.71	1.64	64
deAl-MOR/B-1F/6.8	6.8	2.16	0.24	0.80	1.83	59
deAl-MOR/B/6.6	6.6	2.22	0.32	0.96	2.25	24

[a] from chemical analysis
[b, c] concentrations of acid Brønsted and Lewis sites, respectively, from FTIR spectra of adsorbed d_3-acetonitrile
[d] concentration of Al estimated from the concentration of Brønsted and Lewis sites ($c_{Al} = c_B + 2c_L$)
[e] from FTIR spectra of the bridging OH groups after adsorption of *n*-hexane

The structural changes in mordenites induced by a partial dealumination using mineral acids were described at a molecular level by Van Geem [66] and others [68]. Preferential removal of aluminium from the labile T4 site in the 4-ring forming the walls of the main 12-ring channels results in a widening of a part of the 8-ring channels and a creation of new interconnections between the main channels [41, 66, 68]. However, a small microporous volume (Table 7) and a low accessibility of the OH groups for *n*-hexane (Table 8) in the mildly dealuminated deAl-MOR/B/6.6 sample indicate that the desirable changes in the channel structure require a removal of larger proportions of Al from the framework. ^{27}Al MAS NMR analysis (Figure 24) and the adsorption measurements (Table 7) clearly showed that the acid treatment does not extract all the atoms removed from the framework and various extra-framework species partially block the pores. In contrast, the fluorination-alkaline-acid treatment (Figure 5, series I – III) provides much larger increase in the volume in supermicropores when a similar amount of Al is extracted from the zeolites (compare, e.g., V_{MI} 0.15 and 0.24 cm^3.g^{-1} for deAl-MOR/B/6.6 and deAl-MOR/B-1F/6.8, respectively). The chemism of the concurrent extraction of Al and Si atoms from the zeolite framework by fluorination-alkaline treatments, as described by Yu et al. [44], is shown in Figure 20. After fluorination, a fraction of Si-O-Al framework entities is cleaved by the incorporation of fluorides, but the attacked Al sites are still integrated within the framework as F-bearing tetrahedral Al species [44]. The F-bearing Al are extracted from the zeolite in the form of

$[AlF_2(OH)_2]^-Na^+$ together with the neighbouring Si atoms during the subsequent alkaline leaching (Figure 20). Figure 23B shows an illustration of the changes in local arrangements of the 8-ring after extraction of Al from the T4 site and a neighbouring Si atom from the T2 or T4 site. Although we do not have data showing the dislocation of specific T-atoms, the illustration is in a good agreement with the textural data (Table 7) and the extraction of Al from the framework preferentially from the 12-ring sites is confirmed by the FTIR spectra either before or after the d_3-acetonitrile adsorption.

The changes in the microporous volume, the micropore size and the accessibility of the acid with the chemical conditions of the fluorination-alkaline leaching (Table 7 and Table 8) indicate that the proportion of the extracted atoms is controlled by an interplay of the concentration/distribution of Al in zeolite and the conditions of the treatment. The high intensities in the signals at 30 and 0 ppm in the ^{27}Al MAS NMR spectra (Figure 24) reflect high content of the penta-coordinated and octahedral extraframework Al in samples prepared using the highest concentrations of the fluorination agent ($\geq$1 M NH_4F). Subsequent acid leaching of MOR/B-1F/5.4 using 0.1 M HNO_3 (deAl-MOR/B-1F/6.8) resulted in a slight increase in the molar Si/Al ratio and a significant increase in the microporous volume from 0.12 to 0.24 $cm^3.g^{-1}$ (Table 7) and a slight increase in the concentration of Brønsted sites from 0.22 to 0.24 $mmol.g^{-1}$ and Levis sites from 0.71 to 0.81 $mmol.g^{-1}$ (Table 8). These findings indicate that the extraframework Al species formed in channels after the fluorination-alkaline treatment and blocking part of the micropores were removed by acid leaching. The principle of the fluorination-alkaline-acid treatment is similar to the coupling of dealumination with desilication employed for flexible tailoring of the concentration of aluminum related acid sites in micromesoporous zeolites [38, 41, 79, 86]. The uniqueness of the fluorination-alkaline-acid procedure lies in the effective formation of 3D connected supermicroporous channels enhancing the accessibility of the acid sites without the formation of a significant proportion of the secondary mesoporosity (V_{MI} up to 0.25 $cm^3.g^{-1}$, the mean pore size ~ 7.5 Å).

4.2.2 Hydroisomerization of *n*-hexane using supermicroporous mordenite zeolite

Figure 26 shows hydroisomerization activity over the series of MOR zeolites after fluorination-alkaline and subsequent acid treatments. The catalytic activity is expressed as the yield of the branched C_6 species (the sum of all the di-branched 2,2- and 2,3-dimethylbutanes and mono-branched 2- and 3-methylpentanes) in dependence of the reaction temperature. The selectivity is reflected in the yields of all the C_1-C_5 cracking by-products as the cracking took place together in parallel with isomerization at higher temperatures. The yields of the individual branched hexane isomers and lower molecular weight by-products for hydroisomerization of *n*-hexane over all the prepared Pt/H-MOR at 225 °C and 250 °C are given in Table 9.

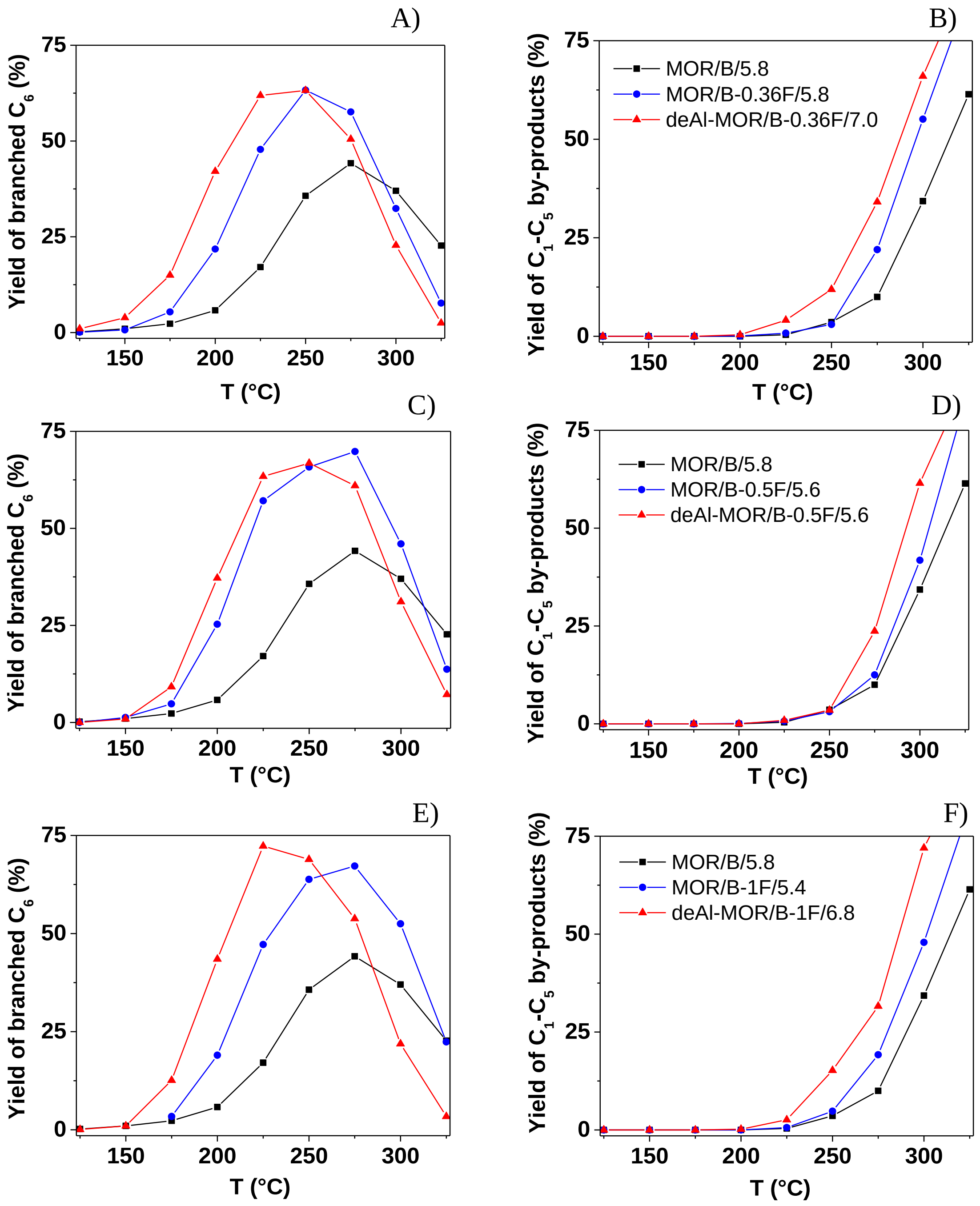

continue on the next page

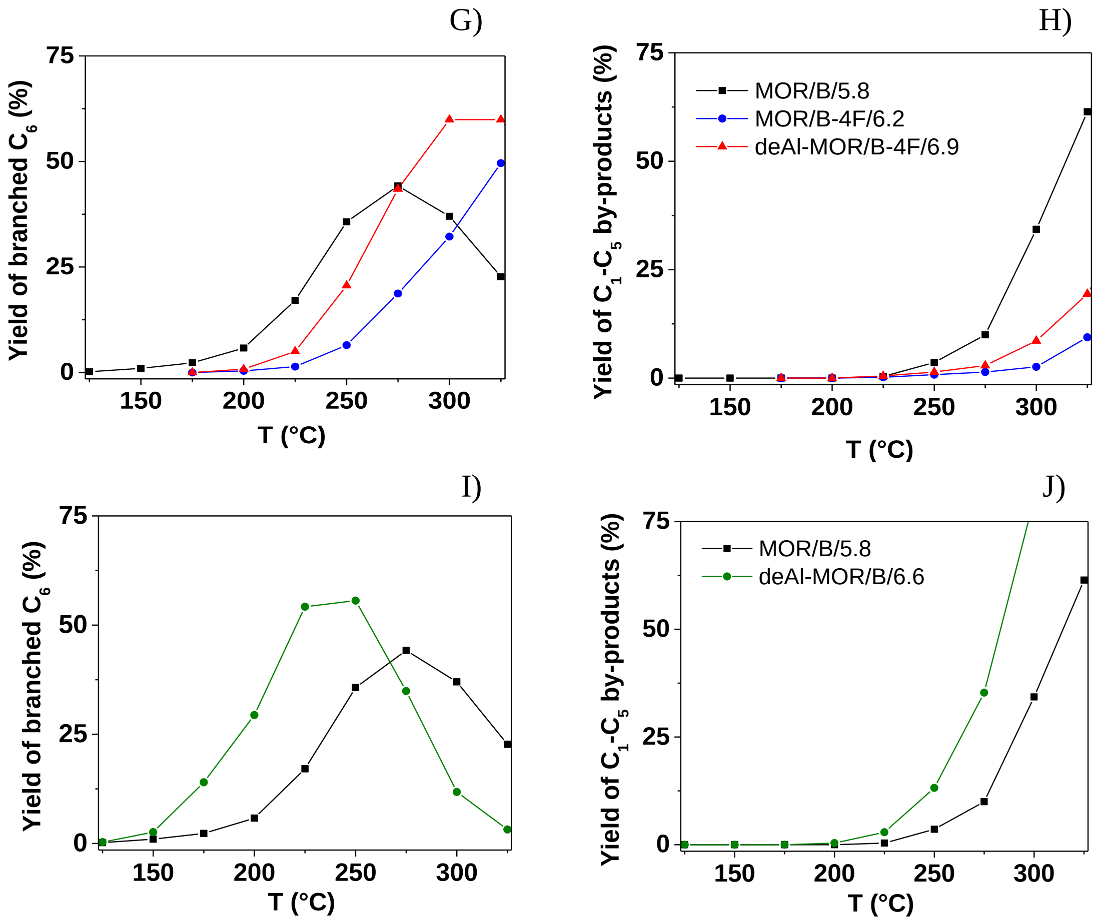

Figure 26. The yields of branched C_6 isomers and C_1-C_5 by-products in the hydroisomerization of *n*-hexane over Pt/H-MOR zeolites. A, B) Series I; C, D) Series II; E, F) Series III; G, H) Series IV and I), J) Series V.

Over the parent Pt/H-MOR/B/5.8, a very low yield of iso-C_6 isomers first appeared at 150 °C, (see Figure 26A), and then their yield continuously increased up to approximately 44% at 275 °C, and finally decreased again (as a result of unselective cracking reactions, which began to take place at 250 °C and then increased continuously to high temperatures, see Figure 26B). Thus the yield of iso-C_6 finally attained values below 23% at 325 °C. The fluorination-alkaline treatments of the parent MOR under mild conditions in Ist series resulted in a substantial increase in its activity, the isomer yield was improved by more than two-fold in the broad temperature range 175 - 250 °C (Table 9). Further, the subsequent mild dealumination led to a further increase and the resultant iso-C_6 yield exceeded 62 - 63% of branched isomers at temperatures of 225 - 250 °C. The corresponding cracking was analogously elevated at temperatures above 250 °C (Figure 26B). In IInd series (Figure 26C, D) the slightly stronger fluorination followed by stronger alkali treatment compared to

Series I and the mild acid dealumination of the MOR increased the catalyst activity even further and 66% iso-C_6 yield was obtained at T < 250°C, over both fluorination-alkaline-acid treated catalysts. Substantially stronger fluorination in series III (Figure 26E, F) followed by mild dealumination finally brought the highest isomer yield increase up to 72%, which was obtained at a temperature as low as 225 °C. All the improved isomer yields were also accompanied by increased cracking yields of C_1 - C_5 by-products, their values increased approximately 3 - 4 times compared to the parent/microporous MOR, e.g. the yield increased from approximately 4% to 15%, from the parent to the last fluorination-alkaline-acid treated MOR, respectively, at 250 °C and continued to predominate at the highest temperatures.

The strongest fluorination-alkaline treatment of 4M NH_4F in IVth series caused a dramatic drop in the yield of isomers (shown in Figure 26G, H), although a slight improvement with mild dealumination was found, nevertheless not achieving the original activity of the parent MOR. In this case, the formation of by-products was proportionately suppressed. Thus, using the optimal fluorination-alkaline-acid step sequence in series III, a resultant highest yield of C_6-isomers as high as 72% was achieved at a temperature of 225 °C, compared to 44% at 275 °C achieved on the parent MOR. For comparison, only a 55% yield at 250 °C was achieved on dealuminated deAl-MOR/B/6.6 (Series V) with a corresponding increase in the amount of by-products from 4% to 12% at 250 °C (shown in the Figure 26I, J).

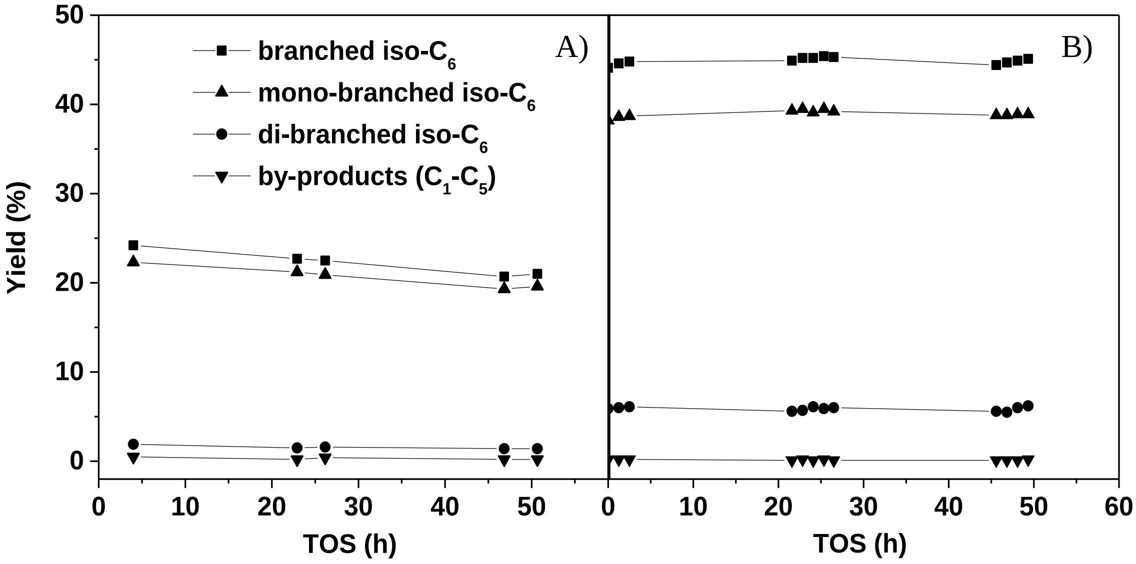

Figure 27. The test of catalytic stability over A) microporous zeolite MOR/B/5.8 and B) supermicroporous deAl-MOR/B-0.5F/5.6 as a dependence of yields of the individual branched hexane isomers and C_1-C_5 by-products on time-on-stream in hydroisomerization of *n*-hexane.

Table 9. Yields of branched hexane isomers and lower molecular weight by-products for hydroisomerization of *n*-hexane over Pt/H-MOR at 225 °C and 250 °C.

Sample	$\Sigma y_{\text{iso-C6}}$ (%)		2,2-DMB		2,3-DMB		2-MP		3-MP		C_1-C_5 (%)	
	225 °C	250 °C	225 °C	250 °C	225 °C	250 °C	225 °C	250 °C	225 °C	250 °C	225 °C	250 °C
MOR/B/5.8	17.5	36.5	0.1	0.7	2.2	3.8	6.6	8.0	8.6	24.0	0.4	2.6
MOR/B-0.36F/5.8	47.8	62.1	3.5	6.5	5.7	7.2	9.4	9.8	29.2	38.6	0.8	7.4
deAl-MOR/B-0.36F/7.0	63.7	65.8	3.0	5.6	7.2	6.9	12.5	11.4	41.0	41.9	2.8	10.9
MOR/B-0.5F/5.6	57.1	65.8	2.0	5.1	6.4	7.0	10.9	12.1	37.8	41.6	0.7	3.1
deAl-MOR/B-0.5F/5.6	63.4	66.8	2.5	5.1	6.8	6.6	12.8	12.3	41.3	42.8	0.9	3.5
MOR/B-1F/5.4	32.8	49.7	0.5	1.8	3.6	5.3	8.5	10.0	20.2	32.6	0.6	4.8
deAl-MOR/B-1F/6.8	72.3	68.9	3.9	9.1	7.9	6.7	13.6	12.0	46.9	41.1	2.6	15.2
deAl-MOR/B/6.6	54.2	55.6	2.2	4.3	5.8	5.9	9.7	9.0	36.5	36.4	2.9	13.2
MOR/B-4F/6.2	1.4	6.5	0.0	0.0	0.0	0.3	0.8	3.5	0.6	2.7	0.2	0.8
deAl-MOR/B-4F/6.9	5.0	20.6	0.0	0.1	0.0	1.2	2.7	6.8	2.3	12.5	0.5	1.4

Table 10. Yields of products for hydroisomerization of n-hexane. Reaction conditions: WHSV 0.25 h^{-1}, molar ratio H_2/n-C_6 79, atmospheric pressure.

Sample	$y_{\Sigma\text{iso-C6}}$ (%)			$y_{\text{2MP+3MP}}$ (%)			$y_{\text{2,2DMB}}$ (%)			$y_{\text{2,3DMB}}$ (%)			$y_{\text{by-products}}$ (%)		
	175 °C	200 °C	225 °C	175 °C	200 °C	225 °C	175 °C	200 °C	225 °C	175 °C	200 °C	225 °C	175 °C	200 °C	225 °C
BEA/A/4.2	35.8	62.6	77.3	30.0	51.2	54.6	3.2	6.4	15.8	2.6	5.0	6.9	0.2	0.5	1.9
BEA/B/11	5.9	31.5	58.6	5.9	27.2	45.9	0.0	2.1	8.2	0.0	2.2	4.5	1.2	4.8	15.5
MOR/A/12	4.5	13.5	36.5	4.5	11.6	28.9	0.0	0.0	1.6	0.0	1.9	6.0	0.0	0.1	0.5
deAl-mm-MOR/A/9.5	6.5	22.0	48.7	4.6	17.4	40.8	0.1	0.8	1.8	1.8	3.8	6.1	0.0	0.4	3.0

The stability of the yields (Figure 27) and selectivity as a function of time-on-stream was analysed over the parent MOR/B/5.8 and over the resultant fluorination-alkaline-acid treated deAl-MOR/B-0.5F/5.6 from Series II (Figure 5) as a typical supermicroporous MOR zeolite. The yield of the all isomers decreased slightly over the parent MOR/B/5.8, from 24% of the initial value to 21% after 48 h of continuous C_6-feeding at a reaction temperature of 235 °C. It was observed to be nearly constant, i.e. 44 - 46%, over deAl-MOR/B-0.5F/5.6 and the yields of the individual mono-branched (38 - 40%) and di-branched isomers (~ 6%) were also constant within > 48 h of time-on-stream. The amount of (C_1 - C_5) by-products was below ~ 1% during both reaction runs. All these observations indicate sufficient structural stability and the absence of any substantial structural damage to the supermicroporous Pt/H-MOR under the reaction conditions [42]; moreover, it also demonstrated some improvement in the time-on-stream stability when compared with the untreated parent MOR/B/5.8.

4.3 Enhancement of concentration of acid sites in microporous zeolite

In pursuing the present work on the isomerization of linear alkanes over zeolites, we wanted to specify the role of an increase in the density of the strongly acidic protons countering the negative charge of the framework in the H-forms of zeolites in relation to the occurrence of Al-Si-Al sequences, inevitably formed at high concentration of Al in the zeolite framework. We wanted to determine the effect of variations in the distribution of aluminum providing charge balance for the corresponding high concentration protons located in the close vicinity on the reaction rate and selectivity. We therefore employed zeolite *BEA topology (Table 1 and Table 11), which can be prepared in a broad range of Al concentrations and which offers fast intra-crystalline diffusion of reactants and products through channels with three-dimensional architecture and 12-MR openings. We exploited recent progress in the synthesis of the beta zeolite that opened a new potential to manipulate the framework aluminum content in a very broad range and employed Al-rich beta zeolites with very high concentration of aluminum (Si/Al ≥ 4) with highly predominant tetrahedrally coordinated Al in the framework [81, 87-98]. This approach enabled us to examine the extent to which the isomerization reaction is affected by close proximity of strongly acidic centers. We found that the high density of non-interacting strongly acidic sites facilitates extraordinarily high reaction rates due to a synergetic effect significantly decreasing the activation barrier of the reaction. This enabled more rational design of isomerization zeolite catalysts providing superior activity.

4.3.1 Structural analysis of Al-rich zeolites

4.3.1.1 Concentration, nature and local arrangement of acid sites in Al-rich zeolite

The pair of samples H-*BEA/A/4.2 (Al-rich *BEA) and H-*BEA/B/11 (Si-rich *BEA) zeolites, exhibiting different concentration of the framework Al atoms corresponding to molar Si/Al_{FR} 4.7 and 11.5, respectively (Table 1 and Table 11), was analyzed for the concentration and strength of the Brønsted sites, the concentration of Lewis acid sites and the presence of structural defects using ^1H MAS NMR spectroscopy, FTIR spectroscopy of the OH groups and adsorbed d_3-acetonitrile, and UV-VIS-NIR spectroscopy of carbocations formed by protonization upon adsorption of hexamethylbenzene (HMB).

Table 11. Characteristics of the beta (*BEA) and mordenite (MOR) zeolites.

Sample	Si/Al^a	$Si/Al_{FR}{}^b$	$c_{Al}{}^a$ mmol.g^{-1}	$c_B{}^c$ mmol.g^{-1}	$c_L{}^c$ mmol.g^{-1}	Crystal size µm	S m^2.g^{-1}
*BEA/A/4.2	4.2	4.7	3.0	1.80	0.22	~0.4	510
*BEA/B/11	11.3	11.5	1.4	0.63	0.32	~0.05	617
MOR/A/12	12.1	12.5	1.3	1.06	0.11	~0.15	454
deAl-mm-MOR/A/9.5	9.5	11.2	1.6	0.77	0.35	~0.15	405[d]

[a] From chemical analysis of the Na^+ form of zeolites.
[b] From ^{29}Si MAS NMR spectra of the Na^+ form of zeolites.
[c] Concentration of Brønsted and Al-Lewis sites from FTIR spectra of adsorbed d_3-acetonitrile.
[d] External surface area 110 m^2.g^{-1}.

The ^1H MAS NMR spectra of the dehydrated H-*BEA/A/4.2 and H-*BEA/B/11 zeolites (Figure 28) exhibit bands with maxima at 1.6, 2.0, 2.4-2.5, and 3.6-3.8 ppm characteristic of terminal and internal SiOH, extra-framework AlOH and bridging Si(OH)Al groups, respectively [99-100]. The main difference in the spectra of H-*BEA/A/4.2 and H-*BEA/B/11 is in the intensity of the signal characteristic of bridging Si(OH)Al groups. The 3 times higher intensity of the signal of the Brønsted sites for H-*BEA/A/4.2 corresponds to the increase in the concentration of Al in the zeolite with Al atoms incorporated predominantly in the regular T_d coordination in the framework. The close positions of the band maxima at 3.6 and 3.8 ppm for Si- and Al-rich *BEA, respectively, can indicate that the acid strength does not greatly differ. The maxima of the signals of the OH groups in the zeolites are not unambiguously connected with their acid strengths; however, the shift matches the changes in properties for a single zeolitic structure [101-102]. The signal of silanol groups forming a surface termination of the crystalline structure is weak for H-*BEA/A/4.2 due to the low external surface of well-developed crystallites compared to high intensity of the band for *BEA/B/11 characteristic of small crystallites. It is obvious that the signal of the internal silanol groups reflecting structural defects associated with removal of the T-atoms or intergrowth structure also exhibits barely distinguishable intensity for the Al-rich *BEA sample compared to the Si-rich *BEA. As the intensities of the ^{1}H MAS NMR bands do not depend on the band positions, they accurately reflect the ratio between the concentrations of the individual hydroxyls. Thus the low intensity signal of the internal silanol groups and the low signal of the OH groups bound to extra-framework and/or perturbed framework Al atoms indicate that the Al-rich *BEA/A/4.2 sample has a well-developed low-defective crystalline structure.

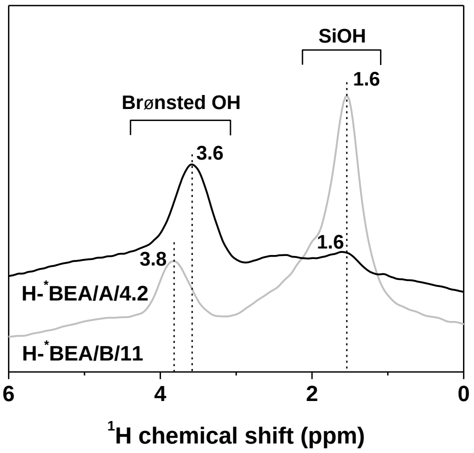

Figure 28. Analysis of acid sites in H-*BEA zeolites dehydrated at 500 °C using ^{1}H MAS NMR spectroscopy.

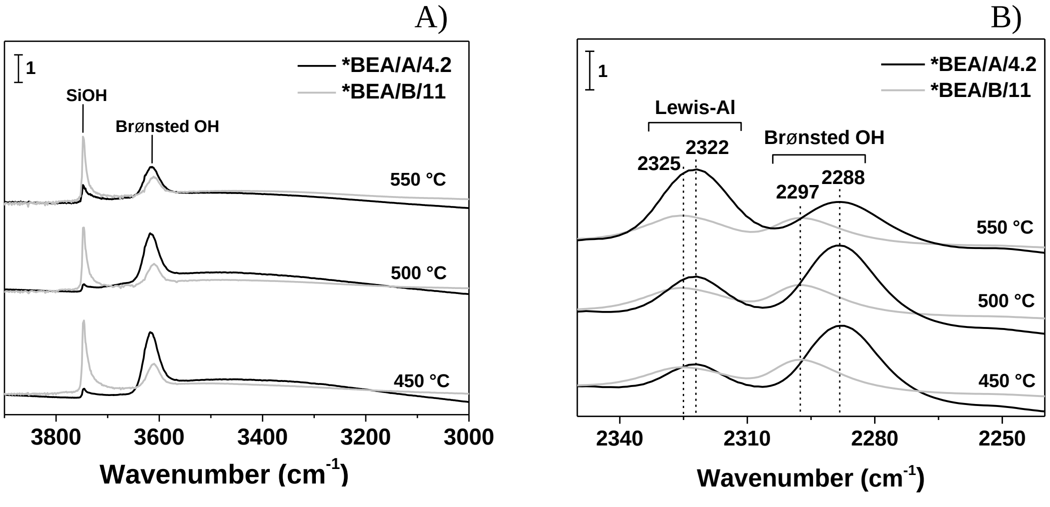

Figure 29. Analysis of acid sites in dehydrated H-*BEA zeolites using FTIR spectroscopy A) the region of the $\nu_{0\rightarrow1}$OH vibration and B) in the region of the $\nu_{0\rightarrow1}$C≡N vibration after adsorption of d_3-acetonitrile.

Figure 29A and 29B shows the FTIR spectra in the region of hydroxyl group vibrations of H-*BEA/A/4.2 and H-*BEA/B/11 evacuated at temperatures from 450 up to 550 °C and after adsorption of d_3-acetonitrile, respectively. The FTIR spectra in the region of the hydroxyl group exhibit approximately 3 times higher intensity of the bands with maxima at about 3610 - 3613 cm^{-1} of the stretching vibration of the bridging hydroxyls, negligible intensity of the bands at 3650 - 3660 cm^{-1} of perturbed framework or extra-framework AlOH [79-80, 103] and low intensity of the band at 3727 - 3745 cm^{-1} of silanols for the H-*BEA/A/4.2 sample compared to H-*BEA/B/11 in good agreement with the ^{1}H MAS NMR results (Figure 28). Only evacuation at 550 °C produced a considerable loss of the intensity for the bridging hydroxyls. This indicates sufficient structural stability of Al-rich H-*BEA zeolite at temperatures relevant for the isomerization reactions. Adsorption of d_3-acetonitrile resulted in the appearance of the bands at 2325 and 2297 cm^{-1} corresponding to the stretching mode of v(C≡N) of d_3-acetonitrile adsorbed on Lewis and Brønsted sites, respectively [45]. Quantitative analysis of the acid sites using the integral intensities of the IR bands and the extinction coefficients for the C ≡N group interacting with the Brønsted and Lewis sites[45] indicated a slightly predominant concentration of Brønsted sites compared to concentration of Lewis sites in the H-*BEA/A/4.2 sample (Table 11). The formation of a significant concentration of Lewis sites is connected with a reversible change in the coordination of the framework Al atoms characteristic of the structure of the *BEA zeolite[98, 104-109] and also observed for Al-rich *BEA[82]. Thus the ^{1}H MAS NMR (Figure 28) and FTIR spectra (Figure 29) and OH groups and adsorbed d_3-acetonitrile together show that the increase in the concentration of the aluminum content does not led to significantly increased dehydroxylation and formation of Lewis acid sites and the concentration of Brønsted hydroxyls in Al-rich beta zeolite is proportional to the increase in the concentration of Al in the zeolite framework [46].

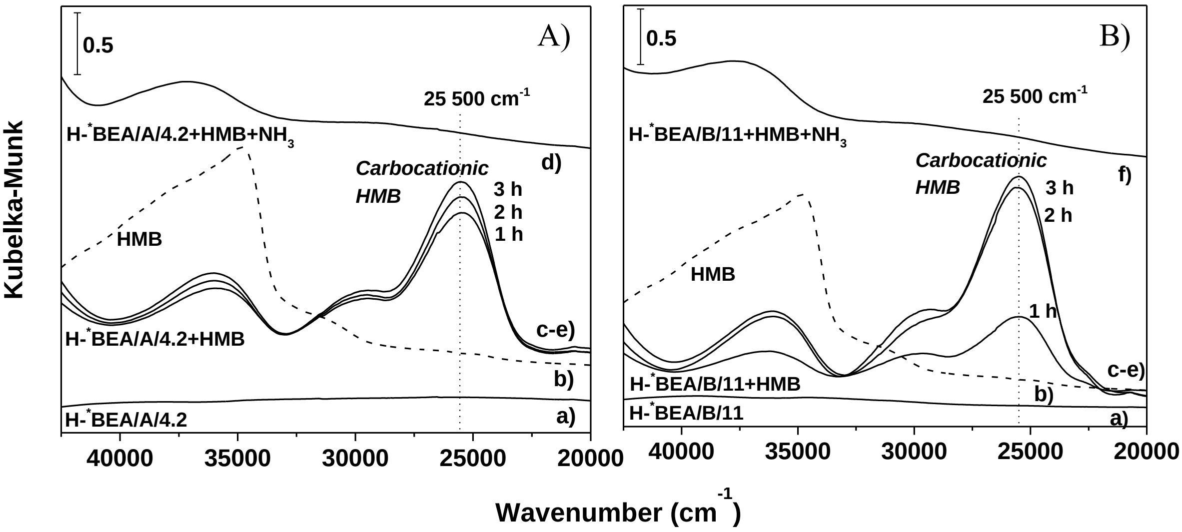

Figure 30. UV-vis spectra of carbocations formed by protonization of hexamethylbenzene (HMB) in A) Al-rich and B) Si-rich H-*BEA zeolites. Spectra of a) zeolites dehydrated at 500 °C, b) solid HMB, c-e) zeolite after interaction with HMB at 150 °C for 1, 2 and 3 h, respectively, and d) after subsequent interaction with NH_3.

The ability of the Brønsted hydroxyls to protonate hexene, the essential step in the isomerization reaction (Step II in Figure 1), is controlled by interplay of the concentration and strength of the acidic centers and confinement of the hydrocarbon molecule in a constrained environment of the zeolite channels [20]. However, the protonation of hexene cannot be experimentally followed because of the unmeasurable hexene concentration under realistic reaction conditions and at higher concentrations due to the rapid oligomerization of the akenes and the formation of complex hydrocarbon molecules [110]. Therefore, the ability of Al-rich H-*BEA zeolite to form carbenium ions was analyzed using the hexamethylbenzene (HMB) molecule, whose protonation yields the relatively stable hexamethylbenzenium cation providing electronic transitions with characteristic spectral components in the range of UV-Vis light [111]. The UV-Vis spectra of HMB and carbocations formed by protonization of adsorbed hexamethylbenzene (HMB) in Al-rich and Si-rich H-*BEA zeolites are shown in Figure 30. The UV-Vis spectrum of neutral HMB exhibited a typical absorption band at 37 000 cm^{-1} characteristic of the π-electron system of the aromatic ring [112]. Adsorption of HMB in both Si- and Al-rich *BEA zeolites resulted in the appearance of an intense band with maximum at 25 500 cm^{-1} with a shoulder around 29 500 cm^{-1} corresponding to the formation of the hexamethylbenzenium cation [111, 113]. The spectra obtained for the two zeolites do not show significant differences in the positions and shapes of the high intensity bands of the carbenium ions and are very similar to those of protonated benzene in a superacidic solution [112]. The assignment of the bands to the hexamethylbenzenium cation was demonstrated experimentally by co-adsorption of ammonia, resulting in disappearance of the band at 25 500 cm^{-1} consistent with proton transfer between ammonia as a stronger base and the hexamethylbenzenium cation forming the ammonium ion and neutral HMB [46].

The negligible intensity of the internal silanol groups, the low signal of the OH groups bound to extra-framework and/or perturbed framework Al atoms and very high intensity of the structural bridging OH groups observed in the ^{1}H MAS NMR and FTIR spectra of Al-rich H-*BEA are consistent with non-defective crystalline structure with a high concentration of non-interacting (isolated) acid sites associated with tetrahedrally coordinated Al atoms in the zeolite framework. In Al-rich *BEA zeolites (Si/Al 4–5), the Al atoms are predominantly present in the Al-Si-Al sequences[81-82, 94, 114] with the concentrations of Al-Si-Al ranging from 40% to 100% of the total Al depending on their arrangement in rings or as long sequences [82]. It follows that the majority of the H^{+} ions in the H-*BEA/A/4.2 sample compensate the negative charge resulting from substitution of the framework Si(IV) by Al(III) in the Al-Si-Al sequences; however, the respective OH groups are reflected in the ^{1}H MAS NMR and FTIR spectra as non-interacting OH groups. Our previous ^{27}Al and ^{29}Si (CP) MAS NMR studies supplemented by FTIR of adsorbed d_3-acetonitrile and UV–Vis spectroscopy of Co(II) ions as probes of close Al atoms and further supported by DFT molecular dynamic calculations of the Co(II) sites in the *BEA zeolites revealed that these Al-Si-Al sequences in Al-rich *BEA zeolites are mostly located in the zeolite wall separating two channels and the Al atoms of the sequence thus face two channels (see Figure 31 and Ref. [82]). The negative charge of the framework originating from these sequences is balanced by two H^{+} ions located in different channels. Therefore the high concentration of Al atoms in the framework of Al-rich beta zeolites does not result in increased formation of interacting OH groups but the Al-Si-Al sequences forming the zeolite beta wall provide H^{+} sites like in a Si-rich zeolite but in significantly increased concentrations. The calculated deprotonation energies used as a measure of the acid strengths of the Brønsted sites corresponding to AlSiAl and AlSiSiAl sequences in Al- and Si-rich *BEA, respectively, reported in the previous study,[81] were in the range of differences in the deprotonation energy values among the protons associated with AlOHSi groups at individual T sites in the framework of *BEA zeolites. This is consistent with the small observed shift in the maxima of the band of bridging hydroxyl groups in the ^{1}H MAS NMR and FTIR spectra, and the similar protonating ability of HMB molecules. The pair of Al- and Si-rich H-*BEA zeolites thus represents unique material that allows elucidation of the effect of the close vicinity of non-interacting acidic protons on activation of a hydrocarbon molecule in acid-catalyzed reactions over zeolite catalysts, moreover, in the three-dimensional channel system with 12-MR openings providing easy intra-crystalline diffusion of reactants and products.

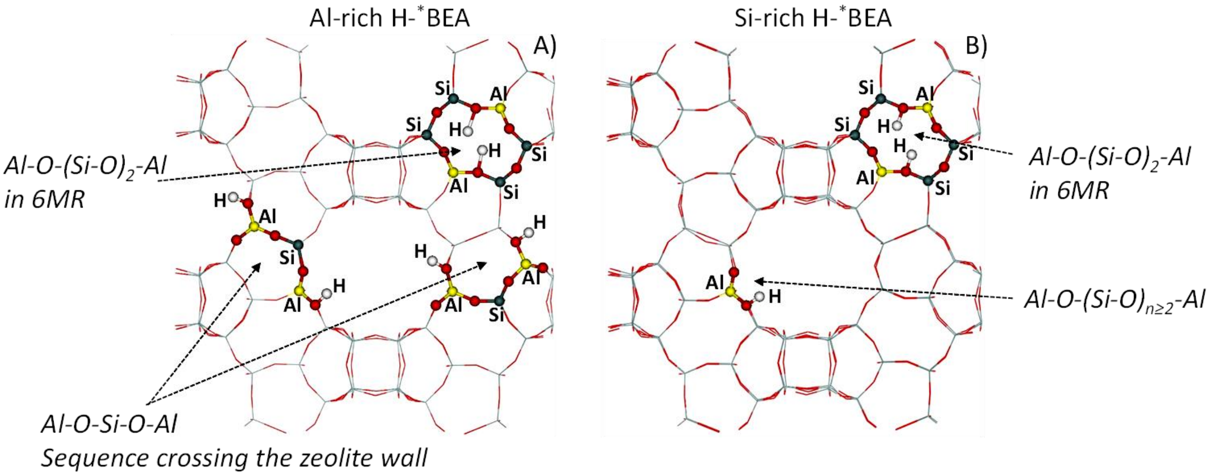

Figure 31. Schematic representations of the main Al-O-(SiO)$_n$-Al sequences in A) Al-rich and B) Si-rich H-*BEA zeolites. H$^+$ compensates the charge mainly from Al-O-Si-O-Al sequences in Al-rich H-*BEA whereas the closest Al atoms form an Al-O-(SiO)$_2$-Al sequence in Si-rich H-*BEA. The Al-O-Si-O-Al sequences cross the zeolite wall and the corresponding H$^+$ are located in two different channels in Al-rich H-*BEA. Oxygens in red.

4.3.1.2 Effect of density of acid sites Al-rich zeolite on hydroisomerization of n-hexane

Figure 32 depicts the yields of branched hexanes and low molecular products as a function of temperature and Arrhenius plots for hydroisomerization of *n*-hexane over Al- and Si-rich Pt/H-*BEA zeolites. The high concentration of close strongly acidic sites in Al-rich *BEA led to a greatly improved yield of branched isomers with very low yield of undesired C_1-C_4 products compared Si-rich *BEA zeolites over the entire temperature range from 150 to 225 °C. The high density of Brønsted sites facilitated dramatically increased conversion of *n*-hexane to *iso*-hexane from 5.9 to 35.5% practically without formation of side-products (0.2% yield of C_1-C_4) at 175 °C (Table 10). More than twice higher TOF calculated per total concentration of Al for Al-rich *BEA clearly shows the substantially higher specific activity of the active sites. The remarkable improvement in the catalytic performance is reflected in the lower apparent activation energy of 104.2 vs. 118.9 kJ.mol^{-1} obtained from the Arrhenius plots for Al- and Si-rich *BEA, respectively, in accordance with the higher specific activity of the active sites. The six-fold higher reaction rate, higher TOF and the lower apparent activation energy by ca. 15 kJ.mol^{-1} for Al-rich *BEA zeolite clearly indicate a synergistic effect of the high concentration and close proximity of the OH groups [46].

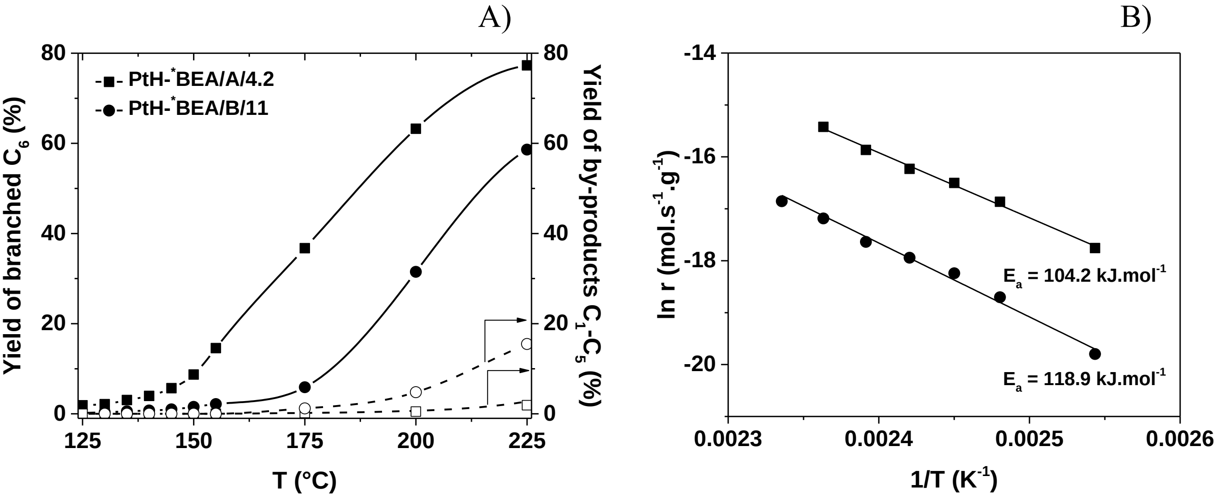

Figure 32. Hydroisomerization of *n*-hexane over Al-rich *BEA (PtH-*BEA/A/4.2) compared with Si-rich *BEA zeolite (PtH-*BEA/B/11). A) Effect of temperature on the yields of branched C_6 isomers and C_1-C_5 by-products and B) Arrhenius plot. *Reaction conditions: WHSV 0.25 h^{-1}, molar ratio H_2/n-C_6 79, atmospheric pressure.*

4.3.2 Implication of enhanced activity of Al-rich zeolites in hydroisomerization of *n*-hexane

It is well established that mordenite zeolites with strongly acidic bridging Si-OH-Al sites are the most active and selective among all the types of investigated zeolitic hydroisomerization catalysts [4, 20, 25, 77-78, 115]. However, considerably lower activity of mordenite zeolites compared to chlorinated alumina necessitates isomerization at higher temperatures leading to unfavorable thermodynamic equilibrium for branched isomers. An essential solution of the problem lies in significant enhancement of the isomerization activity that enables reaching high conversions at lower temperatures in a favorable area of the thermodynamic equilibrium. The remarkable increase in the yield of branched isomers and an increase in the selectivity for the desired products limiting cracking reactions over Al-rich Pt/H-*BEA enables a shift of the operation window to lower temperatures. To analyze the potential of the Al-rich *BEA zeolite as an environmentally sustainable low/medium temperature hydroisomerization catalyst, the activity, selectivity and durability of Al-rich Pt/H-*BEA were compared with state-of-the-art microporous and micro-mesoporous mordenite zeolites under model reaction conditions and also the relevant conditions of the hydroisomerization process, i.e. at elevated pressure and at high concentrations of *n*-hexane in the reaction stream. The yields of branched hexane isomers and C_1-C_5 by-products as a function of temperature at low pressures of *n*-hexane compared for Al-rich Pt/H-*BEA/A/4.2 and microporous and micro-mesoporous Pt/H-mordenite zeolites are shown in Figure 33. The distribution of the formed mono-branched isomers (2-methylpentane and 3-methylpentane) and di-branched isomers (2,2-dimethylbutane and 2,3-dimethyl butane) is listed in Table 10. The yield of branched isomers was approximately 7 times higher (at 175 °C) over Al-rich *BEA than over MOR, while the yield of C_1-C_5 by-products was comparable or lower to that over mordenite catalysts. The performance of the mordenite catalysts was comparable to Si-rich *BEA catalysts.

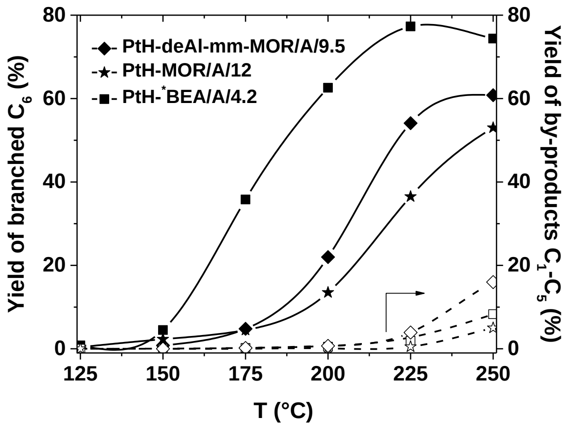

Figure 33. Comparison of Al-rich *BEA (PtH-*BEA/A/4.2) with microporous PtH-MOR/A/12 and partially dealuminated micro-mesoporous PtH- deAl-mm-MOR/A/9.5 zeolites in hydroisomerization of *n*-hexane. Effect of temperature on the yields of branched C_6 isomers and C_1-C_5 by-products. *Reaction conditions: WHSV 0.25* h^{-1}*, molar ratio* $H_2/n\text{-}C_6$ *79, atmospheric pressure.*

Table 12. The yields of branched hexane isomers and lower molecular weight by-products for hydroisomerization of *n*-hexane analyzed under process-like conditions.

	PtH-*BEA/A/4.2		PtH-*BEA/B/11		PtH-MOR/A/12		PtH-deAl-mm-MOR/A/9.5	
	200 °C	215 °C	200 °C	215 °C	200 °C	215 °C	200 °C	215 °C
$y_{\Sigma iso\text{-}C6}$ (%)	51.1	76.8	12.1	31.8	10.1	25.4	10.5	28.1
$y_{2MP+3MP}$ (%)	44.8	62.1	11.9	29.1	8.8	21.8	9.5	24.5
$y_{2,2DMB}$ (%)	1.5	6.7	0.08	1.5	0.32	1	0.95	0.95
$y_{2,3DMB}$ (%)	4.8	8	0.2	1.2	0.93	2.6	0.86	2.67
$y_{\text{by-products } C1\text{-}C4}$ (%)	0.11	2.0	10.7	26.7	0.58	1.3	0.65	1.7

Reaction conditions: WHSV 0.7 h^{-1}*, molar ratio* $H_2/n\text{-}C_6$ *6, pressure 10 bar.*

The performance characteristics of Al-rich Pt/H-*BEA compared to Si-rich Pt/H-*BEA and MOR zeolites under elevated pressure and at high concentration of hexane in the hydrogen stream relevant to the catalytic processes are listed in Table 12.

A threefold increase in the concentration of the active sites and the synergetic effect clearly resulted in the desired increase in activity and selectivity. The Al-rich Pt/H-*BEA/A/4.2 gives an isomer yield of 51.1% at a temperature of 200 °C, whereas the Si-rich Pt/H-zeolites lead to isomers yields from 10.1 to 12.1% at the same temperature. Stable values of the yields of isomers ~77% and by-products ~1.2% as a function of time-on-stream were obtained at 215 °C for 72 h that indicates stability of the Al-rich Pt/H-*BEA (Figure 34). It is clear that the unique density and distribution of the strongly acidic sites are ultimately connected with catalytic performance highly exceeding that of state-of-the-art Si-rich zeolite catalysts. There is no evidence in the scientific literature that the strength of the acidity of the Al-rich H-*BEA zeolite is significantly weakened due to its high aluminum content, at least with respect to acid-catalysed transformations of hydrocarbons. On the contrary, acid-catalysed reactions requiring strongly acidic centers like alkylation and hydroamination of aromatics [81, 116], and cracking and hydrocracking of aromatics and alkanes [81, 92, 94] are substantially improved over Al-rich H-*BEA exceeding significantly the Si-rich H-*BEA zeolites. Thus, the Al-rich H-*BEA provides the unique concentration of strongly acidic sites in the three-dimensional channel system with 12-MR openings. Such density of the acid sites is not available in zeolites with the three-dimensional channel system with 10-MR openings, e.g. ZSM-5 structural topology, due to the absence of a synthesis procedure for the preparation of zeolite with molar Si/Al ratio <10. Al-rich H-*BEA is also advantageous to USY zeolites, wherein the protonic sites are mutually affected due to the presence of Al-Si-Al sequences in the framework and exhibit much lower acid strengths [117]. The three-dimensional channel system with 12-MR openings of Al-rich H-*BEA is also a significant advantage over traditional mordenite based isomerization catalysts where the pseudo-monodimensional channel structure and the restricted accessibility of acid sites located in 8-MR channels limit the efficiency of the catalytic process by mass transfer effects [25].

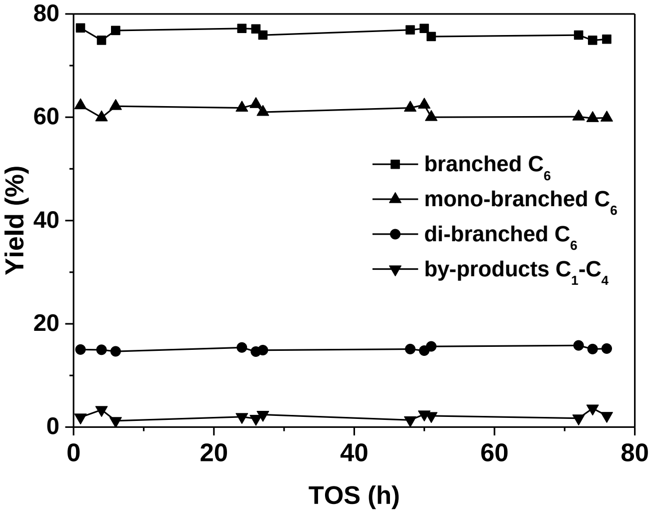

Figure 34. Dependence of the yield of branched hexane isomers and C_1-C_4 by-products on time-on-stream in hydroisomerization of *n*-hexane over Al-rich *BEA (PtH-*BEA/A/4.2). *Reaction conditions: Temperature 215 °C, WHSV 0.7* h^{-1}*, molar ratio* H_2/n-C_6 *6, pressure 10 bar.*

The reduced apparent activation energy and increased TOF for Al-rich H-*BEA zeolite indicate only a partial contribution of the increased concentration of protonic sites to the overall enhancement of the catalytic properties and therefore another factor associated with the close proximity of the active sites plays an important role. Conversely, there are no spectroscopic signatures of significantly different acidic characteristics in the Al-rich beta zeolite. Because the enhancement of the strength of the acid groups has not been observed, the increase in specific activity of close non-interacting OH groups must be accompanied with another specific synergistic effect. Effects of the proximity of Brønsted and Lewis sites [118], the arrangement of acid centers influencing the entropy of the system or an interaction of one molecule with two close centers could possibly affect the overall catalytic process. However, we can not rule out that the overall increase in specific activity is given by contributions from others synergistic effects. The analysis of effects of the proximity of acid sites on reaction mechanism of skeletal isomerization of alkanes needs to be accessed in further studies to obtain full comprehending the consequences of the specific structure.

4.4 Effect of shape selectivity in hierarchical zeolites

This study was performed to analyse the shape selectivity of zeolites with well-developed mesoporous surface in hydroisomerization of *n*-hexane as a representative acid-catalysed transformation of hydrocarbons. The objective of this study was not a detailed analysis of the specific activity and structure of the active acid sites on a molecular level in micromesoporous zeolites, or an analysis and understanding of mechanism and entropy and enthalpy changes during a catalytic reaction, but rather to evaluate the effect of a micromesoporous structure obtained by common methods on the shape selectivity. The initial intuition was that the shape selectivity of zeolites, depending on how reactant/transient state/product fit the spatially defined local reaction environments, will be altered by the non-shape-selective reactions on the surface of mesopores with an open reaction environment lacking the molecular confinement. However, a careful analysis of the relationships between the variation in the microporous/mesoporous zeolitic structures and the distribution of the individual reaction products has taught us that the shape selectivity of zeolites is predominantly controlled by acid sites in the microporous channels with steric constraints and tight confines of reactant molecules regardless of the presence of a well-developed secondary mesoporous structure.

4.4.1 Structure of microporous and mesoporous zeolites

Table 13 lists the microporous and micromesoporous zeolites of ZSM-5 and MOR structures and microporous *BEA and USY (faujasite) zeolites prepared for analysis of the effect of the secondary mesoporous structure on the shape selectivity. Microporous parent zeolites of -ZSM-5, MOR and *BEA structures of a similar Si/Al ratio ~15, denoted as ZSM-5/A/15, MOR/A/12 and *BEA/B/11, respectively, supplemented by zeolites *BEA/A/4.2 (Si/Al 4.2) and USY/6 (Si/Al = 6) were used to reflect the effects of zeolite structure on the catalytic properties enabling comparison of the shape selectivity for various dimensions of the channel systems and differing in the secondary mesoporosity. Three ZSM-5 zeolites (ZSM-5/B/25, ZSM-5/C/25, and ZSM-5/D/22.5) with a similar molar Si/Al ratio of about 23 but largely differing in the crystal size from 50 to 5000 nm (Table 1 and Table 13) were used to analyse the possible effects of textural parameters on the structure of prepared micromesoporous analogues and to analyse the effect of the external surface of microporous zeolites.

Table 13. Characteristics of the microporous ZSM-5, MOR, *BEA and USY and micromesoporous ZSM-5 and MOR zeolites.

Sample	Si/Al^a	C_B ^{b}	C_L ^{b}	Crystal size ^{c} (nm)	V_{tot} (P/P_0~0.8) (cm^3. g^{-1})	V_{MI} ^{d} (cm^3. g^{-1})	V_{MESO} ^{e} (cm^3. g^{-1})	S_{EXT} ^{d} (m^2. g^{-1})
ZSM-5/A/15	15	0.42	0.25	30 - 150	0.22	0.16	0.06	46
mm-ZSM-5/A-F/10.2	10.2	0.19	0.32	30 - 150	0.32	0.10	0.22	182
mm-ZSM-5/A-F/6.9	6.9	0.13	0.44	30 - 150	0.31	0.09	0.22	194
ZSM-5/B/25	25	0.46	0.10	50 - 200	0.21	0.15	0.06	45
mm-ZSM-5/B-F/15.9	15.9	0.30	0.35	50 - 150	0.28	0.14	0.14	121
mm-ZSM-5/B-F/12.9	12.9	0.24	0.27	20-150	0.29	0.16	0.13	107
ZSM-5/C/25	25	0.36	0.09	200 - 600	0.21	0.17	0.04	30
mm-ZSM-5/C-F/15.1	15.1	0.32	0.37	50-300	0.30	0.14	0.16	143
ZSM-5/D/22.5	22.5			2500 x 5000	0.14	0.13	0.01	9
mm-ZSM-5/D-F/13.4	13.4	0.27	0.14	2500 - 5000	0.23	0.12	0.11	94
MOR/A/12	12.1	1.06	0.12	50-500	0.24	0.19	0.05	42
mm-deAl-MOR/A/9.5	9.5	0.55	0.20	50-500	0.25	0.13	0.12	114
deAl-mm-deAl-MOR/A/13.5	13.5	0.43	0.45	50-500	0.26	0.19	0.09	88
***BEA/A/4.2**	4.2	1.8	0.22	100-800	-	0.24	-	12
***BEA/B/11**	11.3	0.63	0.32	20-140	-	0.19	-	66
USY/6	6	-	-	300-1000	-	0.33	-	51

^{a} *from chemical analysis*
^{b} *concentrations of acid Brønsted and Lewis sites, respectively, from FTIR spectra of adsorbed d3-acetonitrile*
^{c} *from SEM micrographs;* ^{d} *estimated from BdB t-plot method;* ^{e} *Vmeso = Vtotal - Vmicro*

The secondary mesoporosity was introduced into the ZSM-5 (Table 3 and Table 13) and mordenite zeolites (Table 2 and Table 13) by desilication and dealumination methods using post-synthesis alkaline, alkaline-acid [41, 46], acid-alkaline-acid [41, 46], and fluorination-alkaline [44] leaching to obtain zeolites with a wide range of mesoporous volume and various mesopore sizes [43].

Figure 35 shows the results of standard characterization methods including X-ray powder diffraction (Figure 35C), N_2 adsorption at the temperature of liquid nitrogen (Figure 35B), SEM and HR-TEM (Figure 35A), and FTIR measurements (Figure 35D, E, F) for representative comparison microporous parent ZSM-5/D/22.5 zeolite and its micromesoporous analogue mm-ZSM-5/D-F/13.4 zeolite. Details of the structural analysis for others materials are shown in Figure 36, Figure 37, Figure 38, Figure 39, Figure 41 and summarized in Table 13. The intensities and patterns of the X-ray diffraction lines for all the microporous and mesoporous zeolites are characteristic of the well-developed crystalline structure irrespective of the zeolite topology (Figure 35C and Figure 36A) without the presence of amorphous or impurity phases.

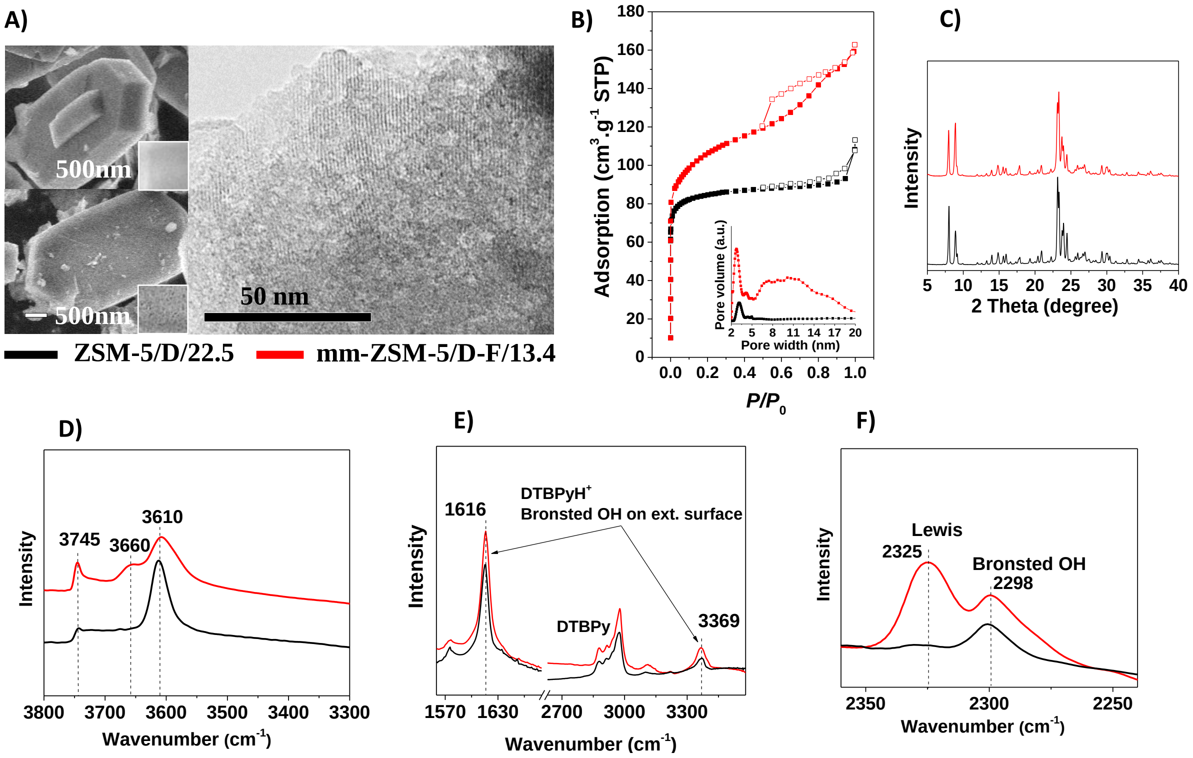

Figure 35. Structural analysis of ZSM-5/D/22.5 and mm-ZSM-5/D-F/13.4 showing characteristic features of microporous and micromesoporous zeolites, respectively. The structural analysis for other zeolites used in the study is shown in the supplementary materials and summarized in table 1. A) SEM and TEM images, B) N_2-adsorption isotherms at 77 K, C) X-ray powder diffraction (XRD) patterns and D) FTIR spectra in the region of OH stretching vibrations and of adsorbed E) 2,6-ditertbutylpyridine and F) d_3-acetonitrile.

Introduction of secondary mesoporosity was manifested in slightly broader reflections due to a decrease in the size of the crystalline domains. Comparison of the SEM and HR-TEM images of zeolites before and after the post-synthesis treatments clearly shows the formation of mesopores and the lattice fringes confirm the preservation of the crystalline structure (Figure 35A, Figure 37, Figure 38). The adsorption isotherms of N_2 on the parent zeolites exhibit sorption at low relative pressures and similar adsorption/desorption branches without hysteresis loops, characteristic of microporous structure without a significant volume in intracrystalline mesopores (Figure 35B and Figure 39).

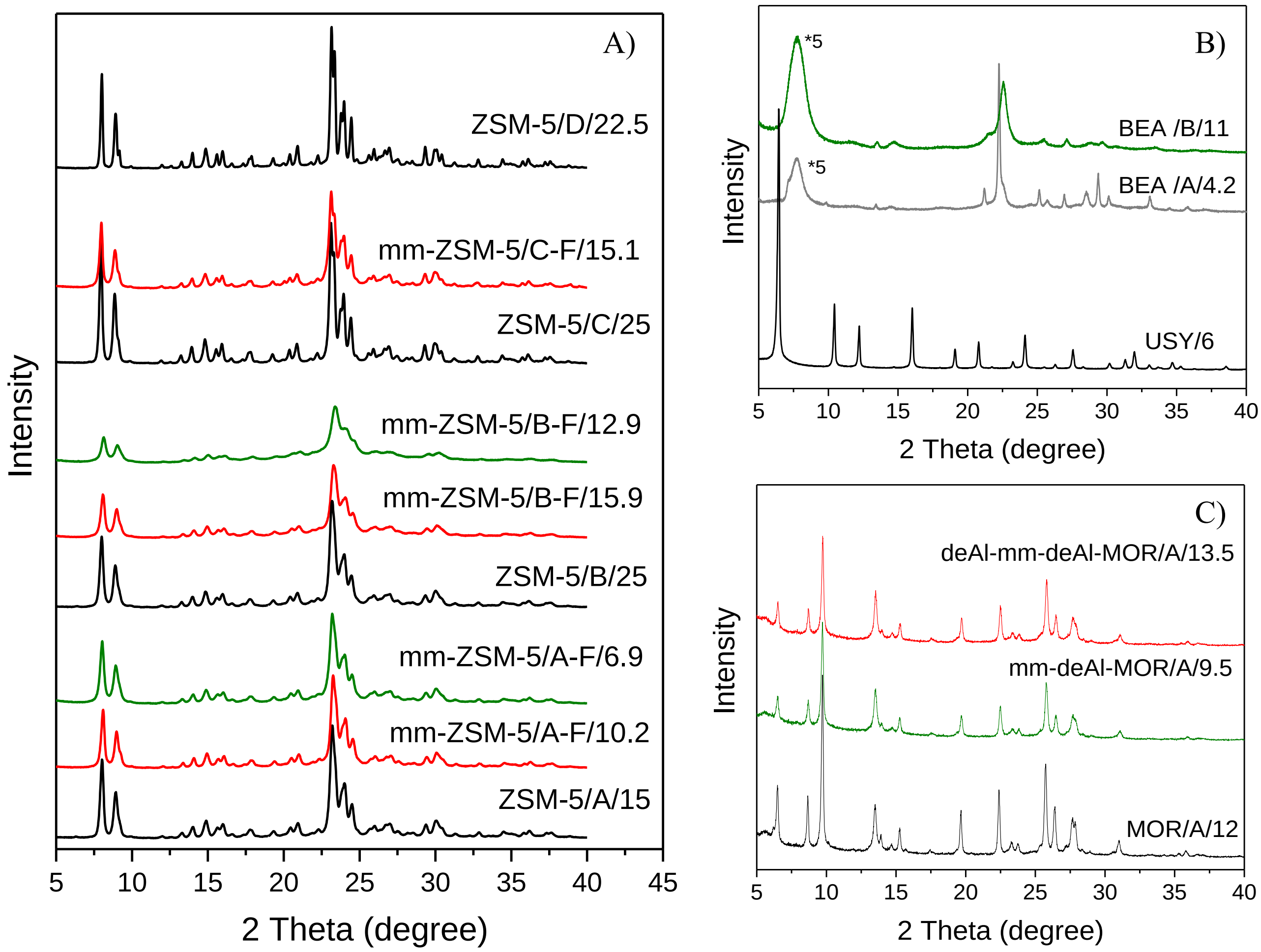

Figure 36. XRD patterns of microporous and micromesoporous zeolites. A) Series of microporous ZSM-5 and their micro-mesoporous analogues, B) microporous *BEA and USY zeolites, and C) series of microporous MOR and its micro-mesoporous analogues.

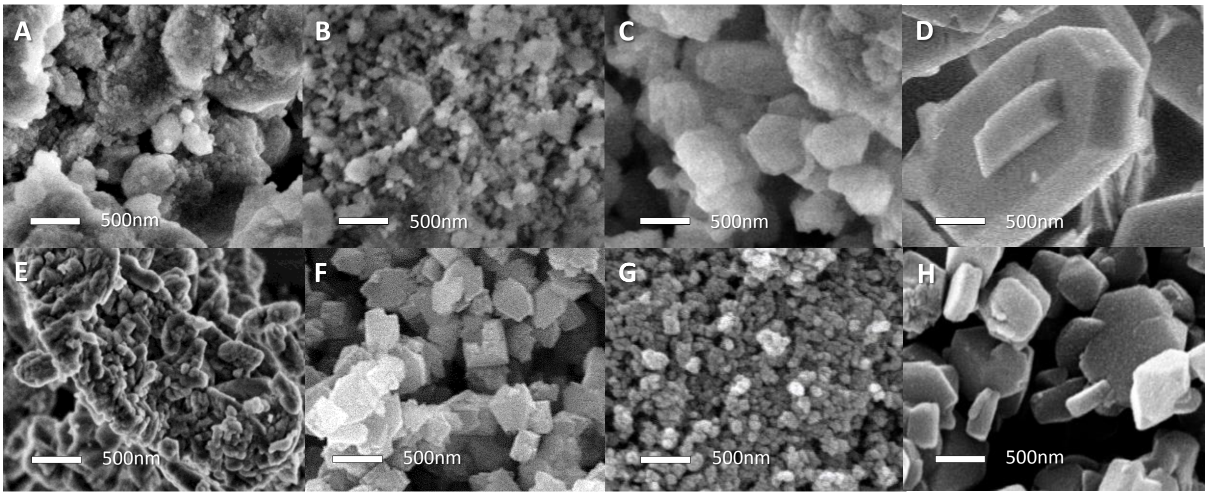

Figure 37. SEM of parent microporous zeolites: A) ZSM-5/A15, B) ZSM-5/B25, C) ZSM-5/C25, D) ZSM-5/D22.5, E) MOR/A/12, F) *BEA/A/4.2, G) *BEA/B/11, and H) USY/6.

The microporous volumes and the calculated specific areas of the external surface of the parent zeolites correspond to well-developed crystalline structures and the size of zeolite crystals, respectively (Table 13). The adsorption isotherms of all the zeolites prepared by post-synthesis alkaline−acid [41, 46], acid−alkaline−acid [41, 46], and fluorination−alkaline [44] treatments (Figure 35B and Figure 39) show the adsorptions from very low to higher relative pressures with typical hysteresis loops characteristic of the micromesoporous structure. The mesoporosity is characterized by cavities from about 3 to 20 nm in size and mesoporous volumes from 0.09 to 0.22 $cm^3.g^{-1}$, depending on the structure of the parent zeolite and the conditions employed in the post-synthesis treatments (Table 13). The prepared micromesoporous ZSM-5 (Table 3) exhibits a wide range of mesoporous volumes from 0.11 to 0.22 $cm^3.g^{-1}$ with a relatively narrow mesopore size distribution of about 3-4 nm for mm-ZSM-5/B-F/12.9 and a broad mesoporous size distribution from 3 to 20 nm for the mm-ZSM-5/A-F/10.2 and mm-ZSM-5/C-F/15.1 samples. mm-deAl-MOR/A/9.5 prepared by alkaline-acid treatment is characterised by mesopores with typical sizes in the range 6 – 10 nm and mesoporous volume of 0.12 $cm^3.g^{-1}$. The acid-alkaline-acid treatment (Figure 4, series II) resulted in a mesoporous volume of 0.09 $cm^3.g^{-1}$ and smaller mesopores about 4 – 6 nm in size. The sequential alkaline-acid leaching treatments of mordenites (Figure 4, serie I) was shown to be important for the formation of micromesoporous mordenite zeolites with active acid sites in an environment of unrestricted microporous channels, as shown in our previous studies [41].

Comparison of the FTIR spectra of dehydrated microporous and mesoporous zeolites in the region of OH stretching vibrations (Figure 35D and Figure 41A, C, E) and of adsorbed d_3-acetonitrile and 2,6-ditertbutylpyridine (DTBPy) (Figure 35E and Figure 40) showed spectral features typical for changes in the structure caused by desilication and mild dealumination [43].

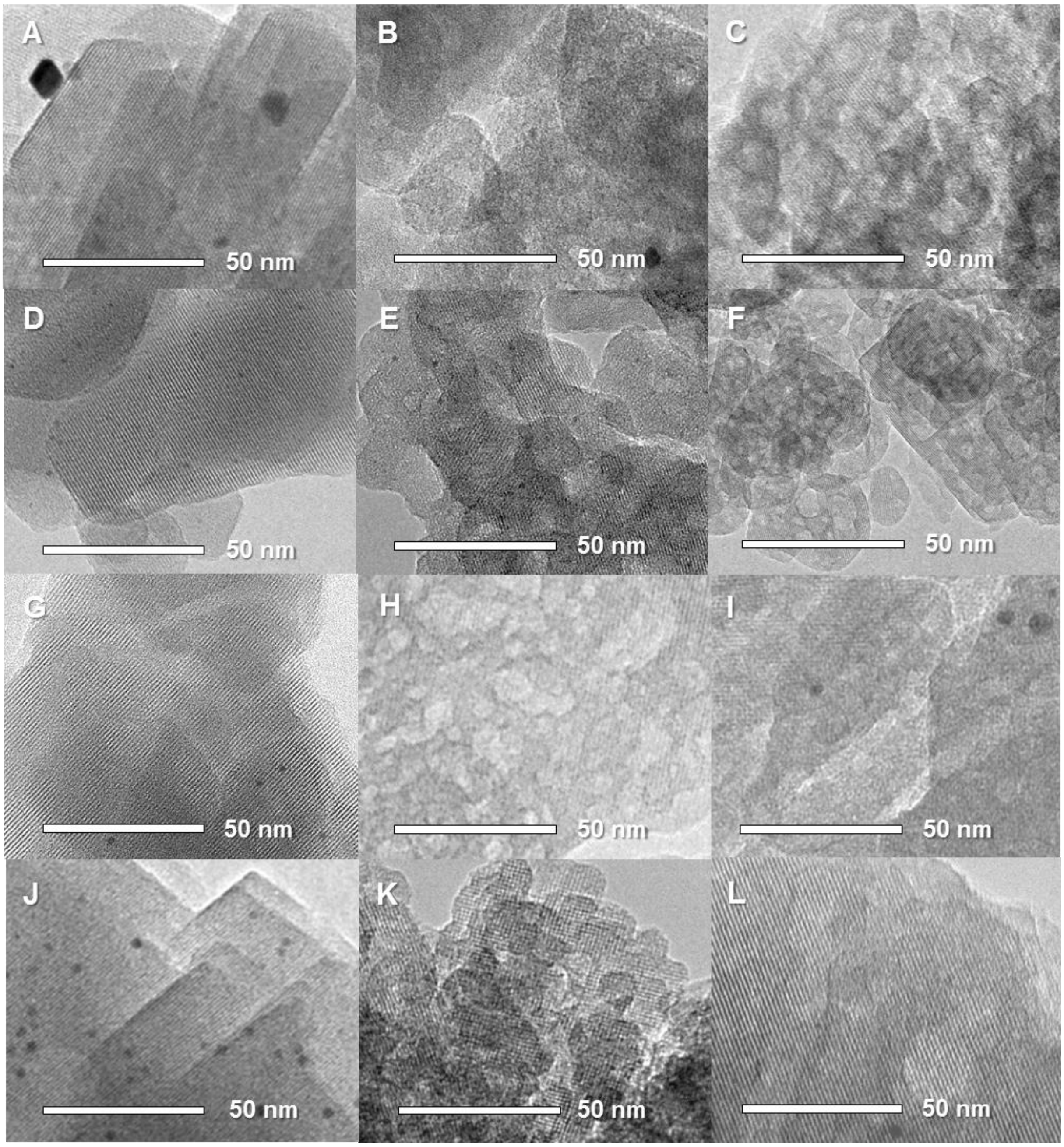

Figure 38. TEM of microporous and micromesoporous zeolites: A) ZSM-5/A15, B) mm-ZSM-5/A-F/10.2, C) mm-ZSM-5/A-F/6.9, D) ZSM-5/C/25, E) mm-ZSM-5/C-F/15.1, F) mm-ZSM-5/C/ G) MOR/A/12, H) mm-deAl-MOR/A/9.5, I) deAl- mm-deAl-MOR/A/13.5 J) BEA/A/4.2, K) BEA/B/11, and L) USY/6.

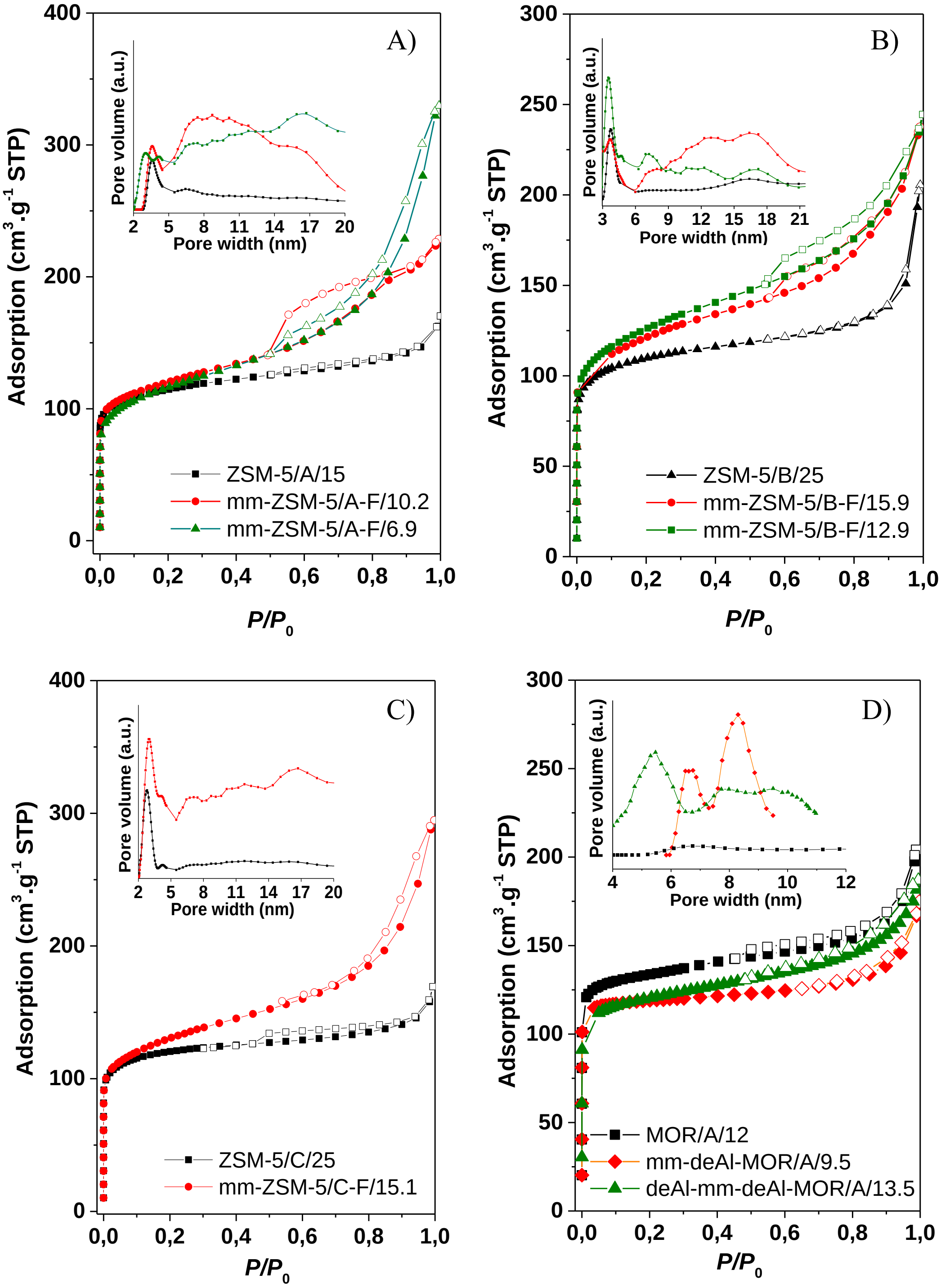

Figure 39. Nitrogen adsorption (solid symbols) and desorption (open symbols) at 77 K and pore size distribution on microporous and micro-mesoporous zeolites prepared by fluorination and sequential alkaline and acid treatments for A) Series of ZSM-5/A, B) Series of ZSM-5/B, C) Series of ZSM-5/C, and D) Series of MOR.

The spectra of both micromesoporous ZSM-5 and MOR zeolites exhibit: i) an increase in the intensity of the internal and external silanol groups reflected in the bands at 3727 and 3745 cm^{-1} (Figure 41A, C, E), respectively, typical of the extension of the external surface area and the formation of internal defects [79], ii) the formation of additional spectral components of low intensity at 3650–3670 cm^{-1} associated with OH groups bound to extra-framework and/or perturbed framework Al atoms (Figure 41A, C, E) , and iii) a decrease in the intensity of the OH stretching vibrations at 3610 cm^{-1} (Figure 41A, C, E) indicating a decrease in the content of non-interacting Brønsted acid groups. Analysis of the absorption bands in the stretching mode of ν(C≡N) for adsorbed d_3-acetonitrile (Figure 41B, D, F) showed a decrease in the intensity at 2298 cm^{-1} of the d_3-acetonitrile adsorbed on the Brønsted acid sites [79] to about half and an increase in the intensity of the bands at 2235 cm^{-1} due to the interaction of d_3-acetonitrile with the Lewis sites [79], indicating an increase in the ratio of Lewis/Brønsted sites. The spectra of adsorbed DTBPy on micromesoporous ZSM-zeolites (Figure 35E and Figure 40) showed an increase in the intensity of the bands at 1615 and 3368 cm^{-1} due to the N-H vibration and the ring vibration of $DTBPyH^+$, respectively, interacting with the acid sites on the external surface and in the pore mouth region of the ZSM-5 zeolites [119-120].

The structural analysis (Table 13) showed that the alkaline leaching of fluorinated ZSM-5 zeolites and the alkaline-acid and acid-alkaline-acid alkaline post-synthesis treatments of the mordenite zeolite enabled controlled extraction of both Al and Si atoms and formation of a well-developed mesoporous structure providing series of micromesoporous zeolites with various degrees of secondary mesoporosity and contents of acid sites [43].

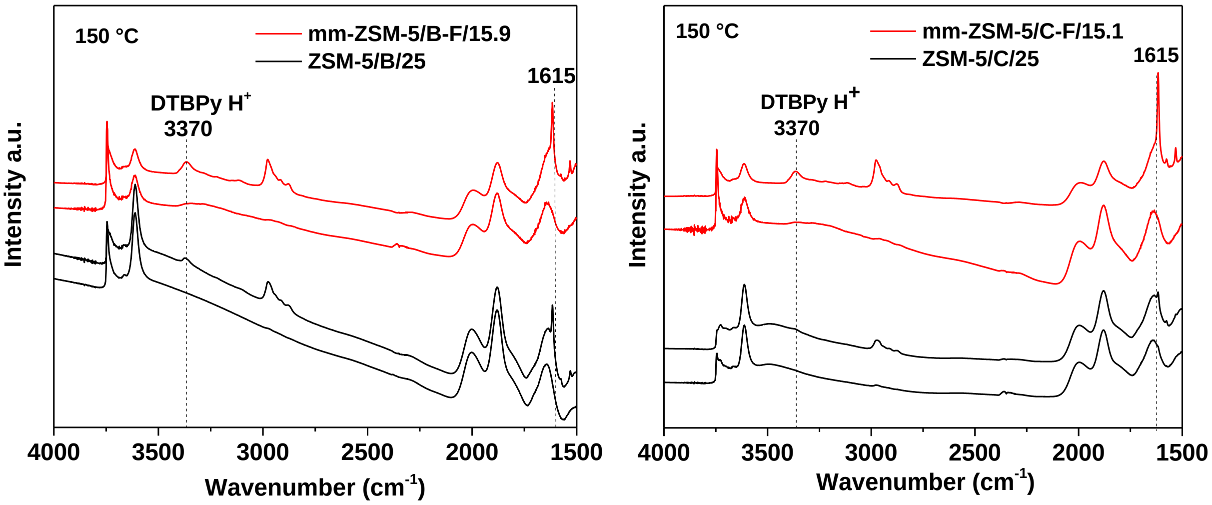

Figure 40. FTIR spectra of microporous and micro-mesoporous ZSM-5 before and after adsorption of DTBPy.

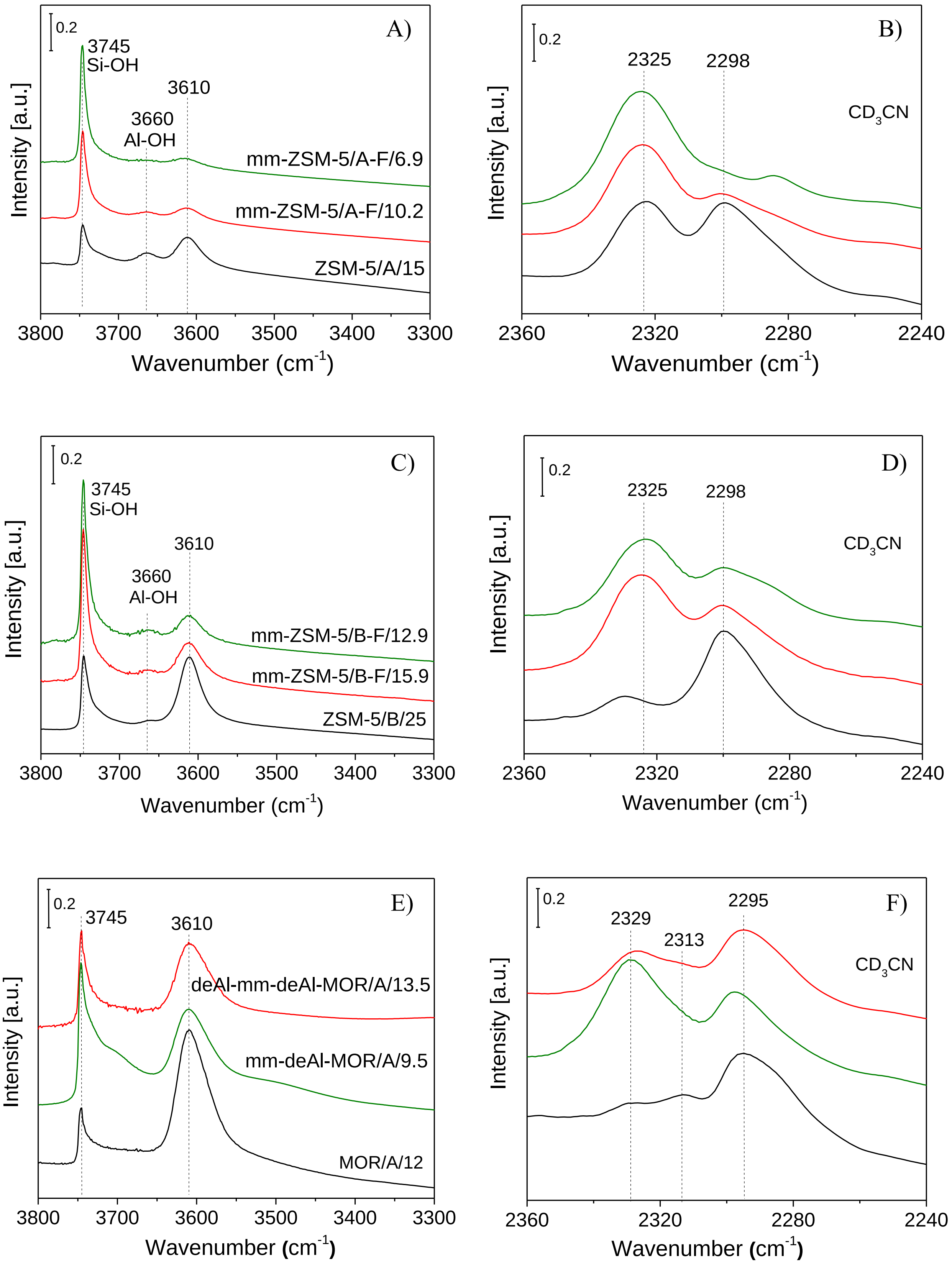

Figure 41. FTIR spectra in the OH stretching region (A, C, and E) and adsorbed d_3-acetonitrile (B, D, and F) for microporous and micro-mesoporous zeolites. A, B) Series of ZSM-5/A; C, D) Series of ZSM-5/B; and E, F) Series of MOR.

4.4.2 Hydroisomerization of *n*-hexane

4.4.2.1 Effect of reactant confinement in microporous and micromesoporous zeolites

Figure 42A compares the reaction rates in the hydroisomerization over Pt/H-ZSM-5 and Pt/H-*BEA zeolites whose microporous structures consist of intersecting three-dimensional (3D) channels with 10-ring openings (approx. 0.51 nm x 0.55 nm and 0.53 nm x 0.56 nm) and 12-ring openings (approx. 0.66 nm x 0.67 nm and 0.56 nm x 0.58 nm), for ZSM-5 and *BEA, respectively. As the both zeolites exhibit similar framework compositions (Si/Al ~ 15) and corresponding concentrations of Brønsted acid sites, they differ mainly in the size of the pore openings and the internal reaction space in the vicinity of the acidic centres given by the channel dimensions. To enable the evaluation of the effect of reactant confinement on the reaction rate of *n*-hexane to 2-methyl- and 3-methylpentanes, the kinetics were determined at conversions well below 10%, where the formation of di-branched hexane isomers and lower molecular weight by-products was negligible for both zeolites. The reaction rates of conversion of *n*-hexane to 2-methyl- and 3-methylpentanes and turn-over-frequency values per Brønsted acid sites for ZSM-5 zeolite are significantly higher than those over *BEA zeolite. The Arrhenius plots of the logarithm of the reaction rate yield linear dependences and apparent activation energies of 117 and 160 kJ.mol^{-1} for ZSM-5 and *BEA (Figure 42A), respectively, reflecting the higher specific activity of ZSM-5 zeolite. It has been well described in the literature that the spatially defined local reaction environments in the zeolite channel control the confinement of a reactant molecule, the corresponding adsorption enthalpy and the entropy of the system, influencing the formation and stabilization of transition states [121-122]. Chiang et al. [20] showed that the variation in reactant confinement in the individual pore structures in the tight 8-ring channels in comparison with that in the 12-ring channels significantly alters the activity in hydroisomerization of *n*-hexane, yielding a much higher reaction rate in the tight 8-ring channels. Consistently, Gounder and Iglesia [123] showed that the turnover rates increase and the apparent activation energies decrease with an increase in the enthalpies of adsorption, due to tighter confinement in 8-ring compared to 10-ring and 12-ring channels also in monomolecular cracking and dehydrogenation of linear alkanes. In accordance with these reports, the apparent activation energy decreased for the ZSM-5 compared to the *BEA catalyst by the difference in the adsorption enthalpies of *n*-hexane (~ 40 kJ.mol^{-1}) [124] in the 10-ring vs. 12-ring channels (Figure 42A).

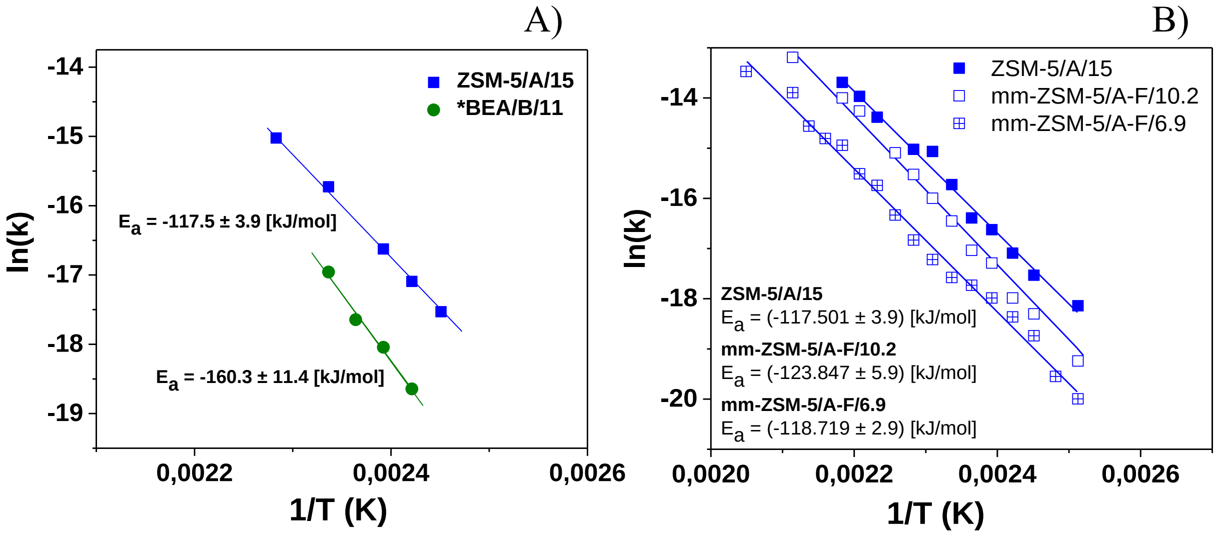

Figure 42. The Arrhenius plots for hydroisomerization of *n*-hexane over Pt/H zeolites. A) The effect of the channel structure on the activity of zeolites (3D 10-ring vs. 3D 12-ring for ZSM-5 and *BEA, respectively) with comparable Si/Al. B) Negligible effect of the presence of secondary mesoporosity in ZSM-5 zeolites on the apparent activation energy.

Figure 42B shows the Arrhenius plots for hydroisomerization of *n*-hexane over the microporous Pt/H-ZSM-5/A zeolite and its micromesoporous analogues. The reaction rates were calculated for low conversions of *n*-hexane and high selectivity for 2-methyl- and 3-methylpentanes (>99%), low selectivity for di-branched hexane isomers (<0.5%), and negligible selectivity for lower molecular weight by-products (<0.1%). The apparent activation energies obtained from the Arrhenius plots for both microporous and micromesoporous ZSM-5 zeolites are close to 120 kJ.mol^{-1}, in agreement with those reported in the literature for microporous ZSM-5 [125]. This shows a negligible effect of the presence of the secondary mesoporosity in ZSM-5 zeolites on the apparent activation energy. The lower concentration of the Brønsted acidic sites in mm-ZSM-5/A-F/10.2 and mm-ZSM-5/A-F/6.9 compared to ZSM-5/A/15 (Table 13) is reflected in the smaller intercepts in the Arrhenius plots.

4.4.2.2 Effect of channel structure and presence of mesoporosity in zeolites on the shape selectivity

The yields of di-branched hexane isomers depending on the total yield of all the branched isomers on microporous ZSM-5, *BEA and faujasite are shown in Figure 44A. The series of microporous ZSM-5 zeolites (Table 3) are highly selective in the formation of the mono-branched isomers ($y_{\text{di-branched C6}} \leq 1.5\%$) because the molecular dimensions of 2,2- and 2,3-dimethylbutanes slightly exceed the internal voids of the 10-ring channel system, imposing a strong product shape selectivity effect (Figure 43).

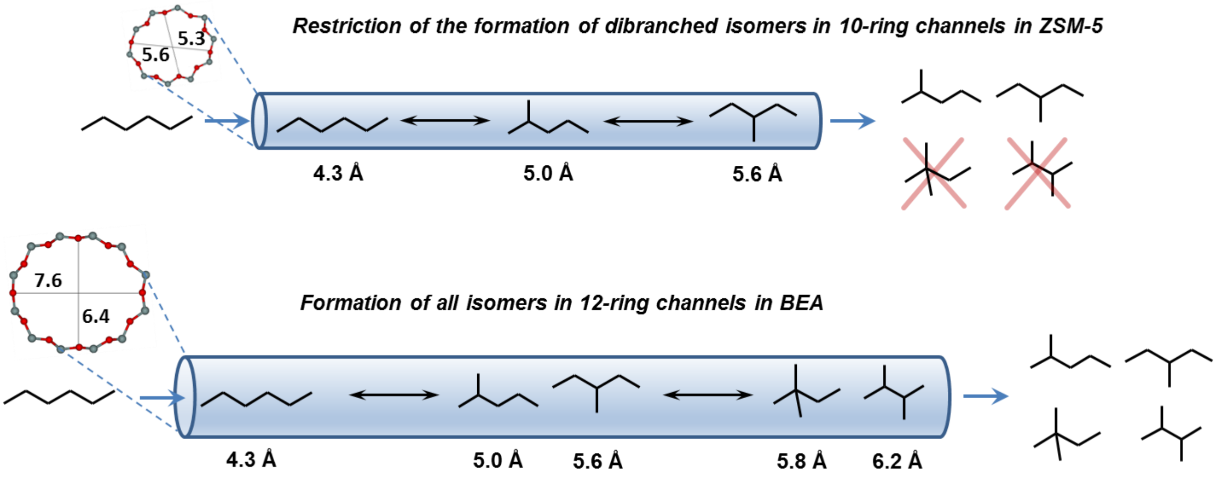

Figure 43. Illustration of the size-shape-selectivity of zeolitic channels in the skeletal isomerization of *n*-hexane. A) The size of the 10-ring channel openings (~5.5 Å × ~5.5 Å) limits the formation and diffusion of 2,2-dimethybutane and 2,3-dimethylbutane molecules with kinetic diameters of 5.8 Å and 6.2 Å, respectively. B) The size of the 12-ring channel openings allows the formation and fast diffusion of all the hexane isomers.

The formation of branched hexanes is reduced in the 10-ring channels approximately according to their diffusion coefficients, where adding each methyl branch lowers the diffusion 1-2 orders of magnitude relative to the linear alkane [126]. Poursaeidesfahani et al. [127] recently showed by a combining simulations and experiments that mono-branched alkanes are selectively formed over ZSM-5 due to product shape selectivity and transition state shape selectivity does not participate in the catalytic process. The high yields of di-branched isomers over *BEA and faujasite (Figure 44A) show that a small increase in the size of channels from 10-ring to 12-ring openings mitigates the shape selectivity effects and the mono- and di-branched isomers can be formed. The yield of di-branched isomers is about ten times higher for *BEA and faujasite than for ZSM-5 and increases with the total yield, as it is consecutive to the formation of monobranched isomers (Supplement 1). The results indicate that hydroisomerization is a reaction which is very sensitive to changes in the spatial arrangement of the local reaction space and accurately detects the degree of the shape selectivity of zeolites [43].

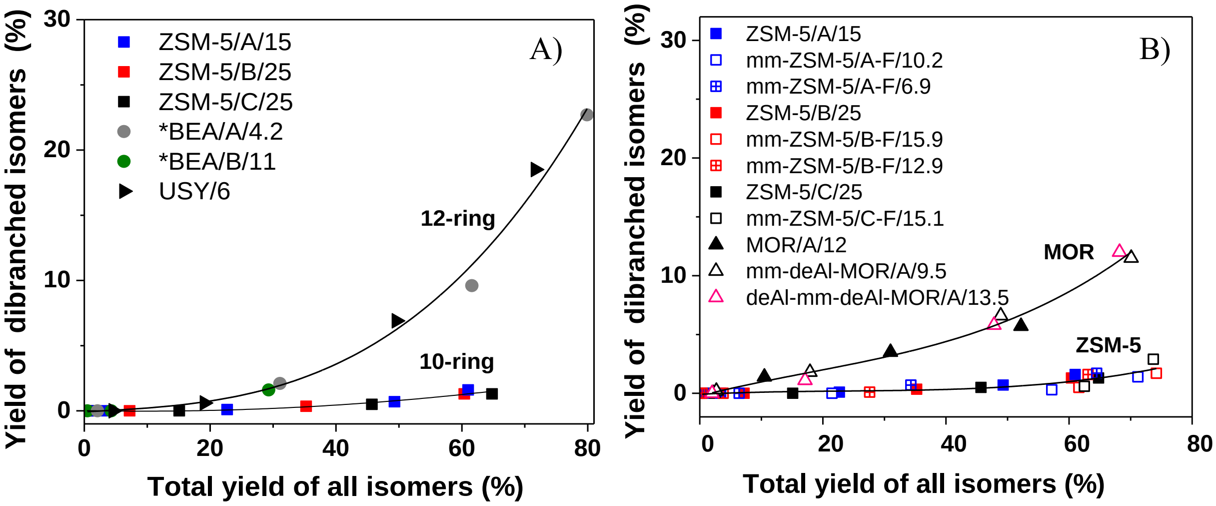

Figure 44. The effect of the size-shape-selectivity on the yield of di-branched isomers in hydroisomerization of *n*-hexane over A) microporous and B) micromesoporous Pt/H-zeolites. A) Zeolites with 12-ring channels (*BEA, USY) yield significantly more di-branched isomers compared to the 10-ring channel zeolite (ZSM-5). B) The same trend in the yield of di-branched isomers for a series of microporous and micro-mesoporous zeolites (Pt/H-ZSM-5 and Pt/H-MOR) shows the absence of the effect of the secondary mesoporosity on the shape-selectivity.

Figure 44B shows the yields of di-branched hexane isomers depending on the total yield of all the branched isomers for the series of microporous and micromesoporous ZSM-5 and MOR zeolites. It is obvious that the distribution of isomers is completely unaffected by the presence or absence of the secondary mesoporous structure. The reaction of hydroisomerization of *n*-hexane over both microporous and micromesoporous ZSM-5 is highly selective in the mono-branched isomers. The shape selectivity of all the micromesoporous ZSM-5 samples is thus fully preserved without the formation of an increased amount of the di-branched hexanes at the expense of mono-branched hexanes (Figure 45A). Comparison of the obtained yields of di-branched hexanes for microporous and micromesoporous mordenites (Figure 44B) also does not exhibit any clear differences. Thus the transformation of *n*-hexane into the mono- and di-branched isomers depends on how the hydrocarbon molecules fit the zeolitic channel in the microporous part of the micromesoporous structure irrespective of the presence of a large surface area of the mesopores, in principal forming an extension of the external surface of the zeolitic crystal. To rule out the explanation that the acidic centres on the mesoporous surface differ from the acid centres on a regular external surface of microporous zeolites due to the preparation process, we also analysed the hydroisomerization of *n*-hexane over a series of microporous ZSM-5

(Figure 45B) fundamentally differing in crystal size (from 50 nm to 5 000 nm), yielding very different external surface areas (Table 13). The identical yields of the mono- and di-branched isomers obtained on all the catalysts clearly show that the acid sites on the external surface do not contribute to the overall isomerization reaction. The formation of individual isomers is thus exclusively controlled by the reactions in the shape-selective environment in the inert voids of the microporous channels [43].

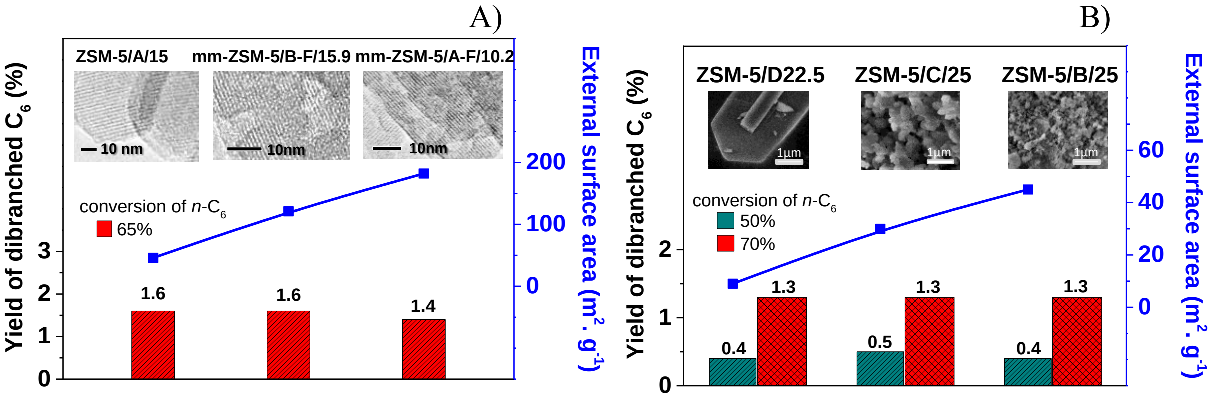

Figure 45. Demonstration of the absence of the effect of the external surface on the formation of di-branched hexane isomers in the hydroisomerization of *n*-hexane over Pt/H-ZSM-5 zeolites. Yield of di-branched isomers for A) micromesoporous ZSM-5 zeolites with various degrees of secondary mesoporosity compared to the total yield of all isomers ($y_{\mathrm{iso+diisohexane}}$) ~ 65% and B) microporous ZSM-5 zeolites largely differing in their crystal sizes at $y_{\mathrm{iso+diisohexane}}$ ~50 and ~65 %.

The presence of acid sites on the external surface is believed to significantly affect the shape selectivity of ZSM-5 zeolites mainly in the isomerization of *o*-xylene [128]; however, recent studies indicate that control of the pore-opening size of ZSM-5 zeolites by their post-synthesis modifications is the decisive factor for the shape selectivity in the acid-catalysed transformation of hydrocarbons, as shown for the selective formation of p-xylene by disproportionation of toluene [129] or Diels–Alder reaction of furan and olefins [130].

The acid strength of Brønsted sites in zeolites is significantly weaker compared to superacids [131-132] and concurrent interaction of the reactant molecule with the acid site and the confinement in the channels of zeolites is necessary for the occurrence of catalytic reactions requiring strongly acidic sites on an open reaction surface [131]. In general, the apparent activation energies decrease monotonously and the reaction rates increase exponentially with an increase in the adsorption enthalpy associated with lateral interactions of an alkane molecule in a zeolite channel [133-137]. The contributions of the interaction of *n*-C_6 molecules with Brønsted acid sites is ~ 10 kJ.mol^{-1} while the van der Waals interactions between *n*-C_6

molecules and the inert walls in 10-ring and 12-ring channels are ~72 and ~48 kJ.mol^{-1}, respectively [124]. Based on comparison of these contributions, it is obvious that the interaction of the hydrocarbon molecule in the confined reaction space with the inner walls of the zeolite channels is an important factor controlling the apparent activation energy of isomerization and the corresponding reaction rate, while the presence of strongly acidic active sites is a necessary condition for the occurrence of the reaction. The reactant confinement and the strong van der Waals interactions in the interior of the zeolitic channels enable acid-catalysed reactions with rates exceeding by several orders of magnitude the reaction rates over acid sites located on the open space of amorphous aluminosilicates [138]. The concurrent interaction of the reactant molecule with the acid sites and the lateral interaction with the walls of the zeolite channels are thus responsible for the isomerization reaction. This is in agreement with the experimental results obtained for *BEA, showing that the less confined acid sites in 12-ring yield a reaction characterized by higher apparent activation energy and lower specific activity, as has also been reported for a variety of zeolitic structures differing in the channel dimensions [74]. In contrast to superacids, where the reaction rate of *n*-hexane skeletal isomerization is predominantly controlled by the acid strength of the acid sites located in unconfined space [139], the dominant factors controlling the reaction over the microporous as well as micromesoporous zeolites are determined by guest−host van der Waals interactions. As the highest activity is obtained with ZSM-5, which has smaller pores than *BEA (see Figure 43), we rule out that differences are caused by entropy changes. Simplified energy diagrams for the acid-catalysed reaction steps of the isomerization of *n*-hexane over micromesoporous zeolites and the functionality of the Brønsted acid sites in different environments are illustrated in Figure 46. The preserved shape selectivity of the micromesoporous zeolites, at least for the reaction studied, clearly show that the advantages of the large surface of mesopores like higher reaction rates for diffusion-limited reactions [41], slower deactivation caused by blocking of the channel openings [29], and shorter residence time in channels improving the selectivity in subsequent reactions [79] can be fully exploited without loss of the shape selectivity. These advantages of hierarchical zeolites have already been demonstrated for a variety of relevant reactions where the shape selectivity effects are essential [36].

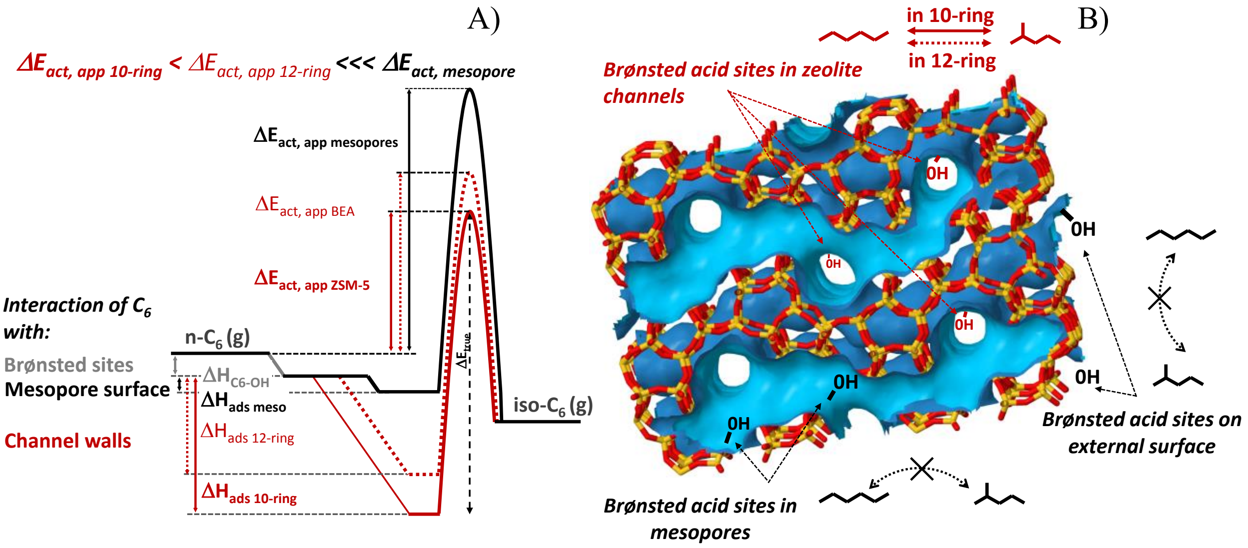

Figure 46. Illustration of the effect of confinement of the hydrocarbon molecule in the zeolite channels on the hydroisomerization of *n*-hexane over micro-mesoporous zeolites. A) The interaction of a C_6 molecule in the confined reaction space of the zeolite channels is the controlling factor decreasing the apparent activation energy. B) The reaction rate over Brønsted acid sites located in the 10-ring is increased compared to the 12-ring channels and the isomerization is negligible in the open reaction environment on the mesopores and exterior of the zeolite crystals.

4.5 Effect of Pt on hydroisomerization of *n*-hexane

The mechanism of the hydroisomerization of *n*-hexane over Pt/H-zeolites (Figure 1) consists of dehydrogenation of *n*-hexane to *n*-hexene on metallic platinum, skeletal isomerization of the formed *n*-hexene into *iso*-hexene via a cyclopropyl intermediate on a Brønsted acid site and re-hydrogenation of the *iso*-hexene to *iso*-hexane [2-7]. The dehydrogenation and hydrogenation reactions are performed in the presence of a sufficient amount of well-dispersed metallic platinum in thermodynamic equilibrium and the acid-catalysed reaction steps control the isomerization [5, 74, 140]. We showed in our studies on hydroisomerization of *n*-hexane over microporous Pt/*BEA and Pt/H-USY [46] and micromesoporous Pt/H-MOR [41, 46] and Pt/H-ZSM-5 [43] zeolites that the dehydrogenation-hydrogenation reactions at a metal loading ~ 1.5 wt. % Pt under the employed reaction conditions (high H_2/*n*-hexane ratio) do not limit the overall alkane hydroisomerization. This is consistent with Ribeiro et al. [140] and Van de Runstraat [74], who demonstrated that the hydrogenation-dehydrogenation reactions are much faster than the skeletal isomerization on acid centres over a variety of Pt/H-zeolites metal loading of ~ 1.5 wt. % Pt. Platinum was introduced into all the zeolitic samples (Table 2 and Table 3) by a standard procedure and its dispersion and the metallic form were confirmed using HR-TEM and a CO sorption followed by FTIR spectroscopy (Figure 47).

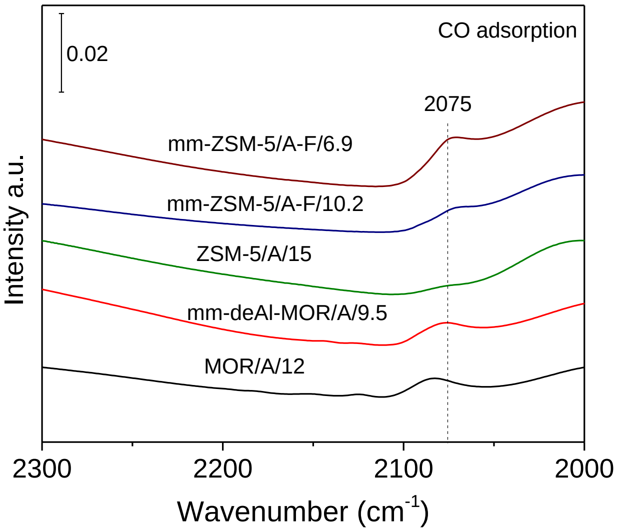

Figure 47. FTIR spectra of CO adsorbed on the microporous and micromesoporous Pt/H-ZSM-5 and Pt/H-MOR zeolites reduced by hydrogen at 250 °C.

The FTIR spectra of CO sorption on reduced Pt/H-zeolites monitored at RT exhibited a characteristic band for the stretching mode of linearly adsorbed CO on the reduced Pt^0 in metallic clusters of 1-20 nm in size [141-142]. The absence of a significant absorption intensity at about at 2180 - 2130 cm^{-1} characteristic of adsorbed CO on Pt^{2+} ions or $Pt_n^{\delta+}$ clusters [141-142] charge-balanced by the zeolite framework, confirms the reduced form of platinum without the presence of a significant amount of platinum ions in the cationic sites. Well-dispersed platinum clusters with a wide distribution of particle sizes ~1-15 nm located on the surface of the zeolite crystals were also observed in the HR-TEM images of all the prepared samples (Figure 38). The incorporation of mesoporosity can lead to the alteration in the proximity between metallic sites (sites for dehydrogenation-hydrogenation) and acid sites (sites for isomerization). The effect of the “distance” between these two types of active sites and its influence on this sequential reaction was recently assessed for Pt/H-mordenite zeolites in our recent studies [41-42, 46]. The effect of nanoscale proximity was recently analysed in detail by Zecevic et al. [143]. The yields of the individual isomers were practically identical for mordenite zeolites with both close and distant Pt^0 and H^+ centres [46].

That the hydrogenation-dehydrogenation function of the platinum clusters present in the mm-deAl-MOR/A/9.5 and deAl-mm-deAl-MOR/A/13 does not limit the acid-catalysed isomerization was demonstrated in our previous study [41]. The sufficient concentration of functional clusters of metallic platinum available in the bifunctional Pt/H-zeolites thus enables analysis of the essential features of the isomerization reaction catalysed by the Brønsted acid sites.

5 CONCLUSION

Doctoral thesis was devoted to the study of hydroisomerization reaction of *n*-hexane which is one of the most important catalytic reactions for production of automotive fuels. The hydroisomerization of C_6, focusing on the transformation of linear C_6 alkanes into the branched isomers with suficiently high octane number, was analysed over hierarchical micromesoporous zeolites, supermicroporous zeolites and microporous zeolites with various densities of active sites. The zeolites were prepared by hydrothermal synthesis and post-synthesis methods using combinations of desilication, dealumination or fluorination.

The critical function of the micromesoporous structure and the concentration and accessibility of Brønsted sites for hydroisomerization of linear hexane was elucidated by using three series of micro-mesoporous mordenite zeolites differing in their mesoporosity and concentration and the accessibility of acid sites (Chapter 4.1). The hydroisomerization of *n*-hexane over microporous Pt/H-mordenite is limited by mass transfer effects due to the low accessibility of acid sites in 8-ring channels structure. The introduction of secondary mesoporosity into mordenite using the alkaline-acid, acid-alkaline-acid, and fluorination-alkaline postsynthesis treatments effectively shortens the length of the 12-ring main channels, opens the side 8-ring channel-pockets, provides the high concentration of Brønsted sites and enhances the accessibility of the acid sites for hexane molecules. The shortening of the main 12-ring channels and a larger number of channel openings provide an increase in the selectivity limits the nonselective subsequent cracking reactions and consequently increases the yield of the desired products at higher temperatures. The micro-mesoporous mordenite structure with the Brønsted sites in the environment of the micropores and accessible through mesopores alleviates the limitations of transport of molecules to/from the active site, resulting in a significant increase in the catalyst efficiency and improvements in the selectivity in skeletal hydroisomerization of *n*-hexane.

It was demonstrated that the simultaneous extraction of Al and Si from the Al-rich MOR framework using fluorination-alkaline-acid treatment leads to high micropore volume (up to 0.25 $cm^3.g^{-1}$), enlargement of the micropores (with mean diameter of about 7.5 Å) and interconnection of the channels (Chapter 4.2). The re-organization of the mono-dimensional channel system of the MOR zeolite into a three-dimensional supermicroporous zeolite structure with connectivity of the pore network providing good accessibility to the acid sites allows the preparation of catalytic materials providing strongly enhanced hydroisomerization properties. These findings highlight the essential role of the 3D supermicroporous structure in the catalytic activity, selectivity of the transformation of *n*-hexane into the corresponding branched isomers without excessive participation of consecutive cracking reactions, and long-term catalytic stability. In general, the concept provides opportunities for the creation of accessible Brønsted and Lewis active sites in Al-rich zeolites for diffusion-restricted reactions.

The role of the density of the acidic protons for hydroisomeroization of *n*-hexane was elucidated using the H-forms of the beta zeolites with a very high concentration of aluminum (Si/Al $\geq$ 4) with highly predominant tetrahedrally coordinated Al atoms in the framework (Chapter 4.3). Analysis of the relationships between the density and distribution of strongly acidic sites and *n*-hexane isomerization identified a specific arrangement of Brønsted acid sites directing the reaction toward higher reaction rates. A high density of strongly acidic non-interacting close OH groups in the Al-rich H-*BEA zeolite (Si/Al ~ 4) lowers the activation barrier in the isomerization reaction and results in multiplying the reaction rates by a factor of six compared to the hitherto most active Si-rich zeolite catalysts. The arrangement of Brønsted acid sites is unique for the Al-rich H-*BEA zeolite and is given by the arrangement of Al atoms in the Al-Si-Al sequences charge-balanced by two H^+ ions located in different zeolite channels. In conclusion, the achievement of the high concentration of non-interacting acidic protons in the zeolite catalyst allowed a significant increase in the isomerization activity and a shift of the operation temperature window into the thermodynamically more favourable region for desired di-branched isomers.

Hydroisomerization of *n*-hexane is very sensitive to changes in the spatial arrangement of the reaction environment and accurately detects the degree of the shape selectivity of zeolites. The formation of di-branched hexane isomers is hindered in ZSM-5 as their molecular dimensions exceed the internal voids of the 10-ring channels imposing strong the product shape selectivity. An increase in the size of the channels from 10-ring to 12-ring openings mitigates the shape-selectivity effects and the mono- and di-branched isomers can be formed with high yields over *BEA and faujasite. The analysis of the hydroisomerization over a series of micromesoporous ZSM-5 zeolites with various degrees of well-developed mesoporous structures as well as over microporous ZSM-5 differing largely in the external surface showed selective formation of the mono-branched isomers regardless of the presence or absence of the mesoporous structure. The spatial confinement of reactants in the internal voids of the zeolitic channel is thus essential for the course of the isomerization reaction and acid sites on the external surface (or mesoporous surface) does not contribute significantly to the catalytic reaction. Thus, the product-shape selectivity of micromesoporous zeolites is virtually unaffected and the advantages of the presence of the secondary mesoporous structure can be fully exploited for tailoring of functionality in the catalytic proces (Chapter 4.4).

REFERENCES

1. Shakun, A. N.; Fedorova, M. L., Isomerization of light gasoline fractions: The efficiency of different catalysts and technologies. *Catalysis in Industry* **2014,** *6* (4), 298-306.
2. Iglesia, E.; Barton, D. G.; Soled, S. L.; Miseo, S.; Baumgartner, J. E.; Gates, W. E.; Fuentes, G. A.; Meitzner, G. D., Selective isomerization of alkanes on supported tungsten oxide acids. In *Stud. Surf. Sci. Catal*, 1996; Vol. 101 A, pp 533-542.
3. Iglesia, E.; Soled, S. L.; Kramer, G. M., Isomerization of Alkanes on Sulfated Zirconia: Promotion by Pt and by Adamantyl Hydride Transfer Species. *Journal of Catalysis* **1993,** *144* (1), 238-253.
4. Chica, A.; Corma, A., Hydroisomerization of pentane, hexane, and heptane for improving the octane number of gasoline. *J. Catal.* **1999,** *187* (1), 167-176.
5. Ono, Y., A survey of the mechanism in catalytic isomerization of alkanes. *Catal Today* **2003,** *81* (1), 3-16.
6. Macht, J.; Carr, R. T.; Iglesia, E., Consequences of Acid Strength for Isomerization and Elimination Catalysis on Solid Acids. *J. Am. Chem. Soc.* **2009,** *131* (18), 6554-6565.
7. Roldán, R.; Romero, F. J.; Jiménez-Sanchidrián, C.; Marinas, J. M.; Gómez, J. P., Influence of acidity and pore geometry on the product distribution in the hydroisomerization of light paraffins on zeolites. *Appl. Catal., A* **2005,** *288* (1–2), 104-115.
8. Gora, L.; Jansen, J. C., Hydroisomerization of C6 with a zeolite membrane reactor. *J. Catal.* **2005,** *230* (2), 269-281.
9. Weyda, H.; Köhler, E., Modern refining concepts - An update on naphtha-isomerization to modern gasoline manufacture. *Catal Today* **2003,** *81* (1), 51-55.
10. Vermeiren, W.; Gilson, J.-P., Impact of Zeolites on the Petroleum and Petrochemical Industry. *Topics in Catalysis* **2009,** *52* (9), 1131-1161.
11. Kramer, G. J.; Vansanten, R. A.; Emeis, C. A.; Nowak, A. K., UNDERSTANDING THE ACID BEHAVIOR OF ZEOLITES FROM THEORY AND EXPERIMENT. *Nature* **1993,** *363* (6429), 529-531.
12. Jones, A. J.; Zones, S. I.; Iglesia, E., Implications of Transition State Confinement within Small Voids for Acid Catalysis. *The Journal of Physical Chemistry C* **2014,** *118* (31), 17787-17800.
13. Smit, B.; Maesen, T. L. M., Towards a molecular understanding of shape selectivity. *Nature* **2008,** *451* (7179), 671-678.

14. Haag, W. O.; Lago, R. M.; Weisz, P. B., THE ACTIVE-SITE OF ACIDIC ALUMINOSILICATE CATALYSTS. *Nature* **1984,** *309* (5969), 589-591.

15. Corma, A.; Fornes, V.; Pergher, S. B.; Maesen, T. L. M.; Buglass, J. G., Delaminated zeolite precursors as selective acidic catalysts. *Nature* **1998,** *396*, 353.

16. Haag, W. O.; Lago, R. M.; Weisz, P. B., The active site of acidic aluminosilicate catalysts. *Nature* **1984,** *309*, 589.

17. Weisz, P. B.; Frilette, V. J., INTRACRYSTALLINE AND MOLECULAR-SHAPE-SELECTIVE CATALYSIS BY ZEOLITE SALTS. *The Journal of Physical Chemistry* **1960,** *64* (3), 382-382.

18. Loëwenstein, W., *Am. Mineral.* **1954,** *39*, 92-96.

19. Zones, S. I., Translating new materials discoveries in zeolite research to commercial manufacture. *Microporous and Mesoporous Materials* **2011,** *144* (1-3), 1-8.

20. Chiang, H.; Bhan, A., Catalytic consequences of hydroxyl group location on the kinetics of n-hexane hydroisomerization over acidic zeolites. *J. Catal.* **2011,** *283* (1), 98-107.

21. Van Laak, A. N. C.; Sagala, S. L.; Zecevic, J.; Friedrich, H.; De Jongh, P. E.; De Jong, K. P., Mesoporous mordenites obtained by sequential acid and alkaline treatments - Catalysts for cumene production with enhanced accessibility. *J. Catal.* **2010,** *276* (1), 170-180.

22. Centi, G.; Perathoner, S., Creating and mastering nano-objects to design advanced catalytic materials. *Coord. Chem. Rev.* **2011,** *255* (13-14), 1480-1498.

23. Groen, J. C.; Zhu, W.; Brouwer, S.; Huynink, S. J.; Kapteijn, F.; Moulijn, J. A.; Pérez-Ramírez, J., Direct demonstration of enhanced diffusion in mesoporous ZSM-5 zeolite obtained via controlled desilication. *J. Am. Chem. Soc.* **2007,** *129* (2), 355-360.

24. Gobin, O. C.; Reitmeier, S. J.; Jentys, A.; Lercher, J. A., Role of the surface modification on the transport of hexane isomers in ZSM-5. *J. Phys. Chem. C* **2011,** *115* (4), 1171-1179.

25. Tromp, M.; van Bokhoven, J. A.; Garriga Oostenbrink, M. T.; Bitter, J. H.; de Jong, K. P.; Koningsberger, D. C., Influence of the Generation of Mesopores on the Hydroisomerization Activity and Selectivity of n-Hexane over Pt/Mordenite. *J. Catal.* **2000,** *190* (2), 209-214.

26. Beyerlein, R. A.; Choi-Feng, C.; Hall, J. B.; Huggins, B. J.; Ray, G. J., Effect of steaming on the defect structure and acid catalysis of protonated zeolites. *Topics in Catalysis* **1997,** *4* (1), 27-42.

27. Corma, A.; Fornes, V.; Melo, F.; Pérez-Pariente, J., *Zeolite Beta: Structure, Activity, and Selectivity for Catalytic Cracking*. 1988; Vol. 375, p 49-63.

28. Steijns, M.; Froment, G. F., Hydroisomerization and Hydrocracking. 3. Kinetic Analysis of Rate Data for n-Decane and n-Dodecane. *Industrial and Engineering Chemistry Product Research and Development* **1981,** *20* (4), 660-668.

29. Choi, M.; Na, K.; Kim, J.; Sakamoto, Y.; Terasaki, O.; Ryoo, R., Stable single-unit-cell nanosheets of zeolite MFI as active and long-lived catalysts. *Nature* **2009,** *461* (7261), 246-U120.

30. Corma, A.; Díaz-Cabãas, M. J.; Jordá, J. L.; Martínez, C.; Moliner, M., High-throughput synthesis and catalytic properties of a molecular sieve with 18- and 10-member rings. *Nature* **2006,** *443* (7113), 842-845.

31. Fan, W.; Snyder, M. A.; Kumar, S.; Lee, P. S.; Yoo, W. C.; McCormick, A. V.; Lee Penn, R.; Stein, A.; Tsapatsis, M., Hierarchical nanofabrication of microporous crystals with ordered mesoporosity. *Nature Materials* **2008,** *7* (12), 984-991.

32. Jacobsen, C. J. H.; Madsen, C.; Houzvicka, J.; Schmidt, I.; Carlsson, A., Mesoporous zeolite single crystals [2]. *Journal of the American Chemical Society* **2000,** *122* (29), 7116-7117.

33. Park, D. H.; Kim, S. S.; Wang, H.; Pinnavaia, T. J.; Papapetrou, M. C.; Lappas, A. A.; Triantafyllidis, K. S., Selective petroleum refining over a zeolite catalyst with small intracrystal mesopores. *Angew. Chem.* **2009,** *48* (41), 7645-7648.

34. Groen, J. C.; Moulijn, J. A.; Perez-Ramirez, J., Desilication: On the controlled generation of mesoporosity in MFI zeolites. *J. Mater. Chem.* **2006,** *16* (22), 2121-2131.

35. Pérez-Ramírez, J., Zeolite nanosystems: Imagination has no limits. *Nature Chemistry* **2012,** *4* (4), 250-251.

36. Hartmann, M., Hierarchical zeolites: A proven strategy to combine shape selectivity with efficient mass transport. *Angewandte Chemie - International Edition* **2004,** *43* (44), 5880-5882.

37. Wang, Y.; Sun, Y.; Lancelot, C.; Lamonier, C.; Morin, J. C.; Revel, B.; Delevoye, L.; Rives, A., Effect of post treatment on the local structure of hierarchical Beta prepared by desilication and the catalytic performance in Friedel-Crafts alkylation. *Microporous and Mesoporous Materials* **2015,** *206* (C), 42-51.

38. Sazama, P.; Sobalik, Z.; Dedecek, J.; Jakubec, I.; Parvulescu, V.; Bastl, Z.; Rathousky, J.; Jirglova, H., Enhancement of Activity and Selectivity in Acid-Catalyzed Reactions by Dealuminated Hierarchical Zeolites. *Angewandte Chemie-International Edition* **2013,** *52* (7), 2038-2041.

39. Bjørgen, M.; Joensen, F.; Spangsberg Holm, M.; Olsbye, U.; Lillerud, K. P.; Svelle, S., Methanol to gasoline over zeolite H-ZSM-5: Improved catalyst performance by treatment with NaOH. *Applied Catalysis A: General* **2008,** *345* (1), 43-50.

40. Moller, K.; Bein, T., Mesoporosity - a new dimension for zeolites. *Chemical Society Reviews* **2013,** *42* (9), 3689-3707.

41. Pastvova, J.; Kaucky, D.; Moravkova, J.; Rathousky, J.; Sklenak, S.; Vorokhta, M.; Brabec, L.; Pilar, R.; Jakubec, I.; Tabor, E.; Klein, P.; Sazama, P., Effect of Enhanced Accessibility of Acid Sites in Micromesoporous Mordenite Zeolites on Hydroisomerization of n-Hexane. *Acs Catalysis* **2017,** *7* (9), 5781-5795.

42. Pastvova, J.; Pilar, R.; Moravkova, J.; Kaucky, D.; Rathousky, J.; Sklenak, S.; Sazama, P., Tailoring the structure and acid site accessibility of mordenite zeolite for hydroisomerisation of n-hexane. *Applied Catalysis A: General* **2018,** *562*, 159-172.

43. Sazama, P.; Pastvova, J.; Kaucky, D.; Moravkova, J.; Rathousky, J.; Jakubec, I.; Sadovska, G., Does hierarchical structure affect the shape selectivity of zeolites? Example of transformation of n-hexane in hydroisomerization. *Journal of Catalysis* **2018,** *364*, 262-270.

44. Yu, L. L.; Huang, S. J.; Miao, S.; Chen, F. C.; Zhang, S.; Liu, Z. N.; Xie, S. J.; Xu, L. Y., A Facile Top-Down Protocol for Postsynthesis Modification of Hierarchical Aluminum-Rich MFI Zeolites. *Chemistry-a European Journal* **2015,** *21* (3), 1048-1054.

45. Wichterlova, B.; Tvaruzkova, Z.; Sobalik, Z.; Sarv, P., Determination and properties of acid sites in H-ferrierite: A comparison of ferrierite and MFI structures. *Microporous Mesoporous Mater.* **1998,** *24* (4-6), 223-233.

46. Sazama, P.; Kaucky, D.; Moravkova, J.; Pilar, R.; Klein, P.; Pastvova, J.; Tabor, E.; Sklenak, S.; Jakubec, I.; Mokrzycki, L., Superior activity of non-interacting close acidic protons in Al-rich Pt/H-*BEA zeolite in isomerization of n-hexane. *Applied Catalysis a-General* **2017,** *533*, 28-37.

47. Eder, F.; Stockenhuber, M.; Lercher, J. A., Bronsted acid site and pore controlled siting of alkane sorption in acidic molecular sieves. *J. Phys. Chem. B* **1997,** *101* (27), 5414-5419.

48. Zholobenko, V. L.; Makarova, M. A.; Dwyer, J., Inhomogeneity of Brönsted acid sites in H-mordenite. *J. Phys. Chem.* **1993,** *97* (22), 5962-5964.

49. Bordiga, S.; Lamberti, C.; Geobaldo, F.; Zecchina, A.; Palomino, G. T.; Arean, C. O., Fourier-transform infrared study of CO adsorbed at 77 K on H-mordenite and alkali-metal-exchanged mordenites. *Langmuir* **1995,** *11* (2), 527-533.

50. Wakabayashi, F.; Kondo, J.; Wada, A.; Domen, K.; Hirose, C., FT-IR studies of the interaction between zeolitic hydroxyl groups and small molecules. 1. Adsorption of nitrogen on H-mordenite at low temperature. *J. Phys. Chem.* **1993,** *97* (41), 10761-10768.

51. Alberti, A., Location of Brønsted sites in mordenite. *Zeolites* **1997,** *19* (5), 411-415.

52. Viswanadham, N.; Kumar, M., Effect of dealumination severity on the pore size distribution of mordenite. *Microporous and Mesoporous Mater.* **2006,** *92* (1-3), 31-37.

53. Lietz, G.; Schnabel, K. H.; Peuker, C.; Gross, T.; Storek, W.; Volter, J., Modifications of H-ZSM-5 Catalysts by NaOH Treatment. *J. Catal.* **1994,** *148* (2), 562-568.

54. Remy, M. J.; Stanica, D.; Poncelet, G.; Feijen, E. J. P.; Grobet, P. J.; Martens, J. A.; Jacobs, P. A., Dealuminated H-Y zeolites: Relation between physicochemical properties and catalytic activity in heptane and decane isomerization. *J. Phys. Chem.* **1996,** *100* (30), 12440-12447.

55. Chen, T. H.; Wouters, B.; Grobet, P., Distorted tetrahedral coordinated aluminum in calcined mordenite identified by nutation and 2D ²⁷Al MQMAS NMR spectroscopy. *Chem. J. Internet* **2000,** *2* (4), 7-13.

56. Chen, T. H.; Wouters, B. H.; Grobet, P. J., Aluminium coordinations in zeolite mordenite by ²⁷Al multiple quantum mas NMR spectroscopy. *Eur. J. Inorg. Chem.* **2000,** (2), 281-285.

57. Wouters, B. H.; Chen, T.; Grobet, P. J., Steaming of zeolite Y: formation of transient Al species. *Journal of Physical Chemistry B* **2001,** *105* (6), 1135-1139.

58. Chen, J.; Chen, T.; Guan, N.; Wang, J., Dealumination process of zeolite omega monitored by ²⁷Al 3QMAS NMR spectroscopy. *Catal Today* **2004,** *93-95*, 627-630.

59. Samoson, A.; Lippmaa, E.; Engelhardt, G.; Lohse, U.; Jerschkewitz, H. G., Quantitative high-resolution 27Al NMR: tetrahedral non-framework aluminium in hydrothermally treated zeolites. *Chem. Phys. Lett.* **1987,** *134* (6), 589-592.

60. Sayed, M. B.; Kydd, R. A.; Cooney, R. P., A Fourier-transform infrared spectral study of H-ZSM-5 surface sites and reactivity sequences in methanol conversion. *J. Catal.* **1984,** *88* (1), 137-149.

61. Kustov, L. M.; Kazansky, V. B.; Beran, S.; Kubelkova, L.; Jiru, P., Adsorption of carbon monoxide on ZSM-5 zeolites. Infrared spectroscopic study and quantum-chemical calculations. *J. Phys. Chem.* **1987,** *91* (20), 5247-5251.

62. Fritz, P. O.; Lunsford, J. H., The effect of sodium poisoning on dealuminated Y-type zeolites. *J. Catal.* **1989,** *118* (1), 85-98.

63. Groen, J. C.; Jansen, J. C.; Moulijn, J. A.; Pérez-Ramírez, J., Optimal aluminum-assisted mesoporosity development in MFI zeolites by desilication. *J. Phys. Chem. B* **2004,** *108* (35), 13062-13065.

64. Svelle, S.; Sommer, L.; Barbera, K.; Vennestrøm, P. N. R.; Olsbye, U.; Lillerud, K. P.; Bordiga, S.; Pan, Y. H.; Beato, P., How defects and crystal morphology control the effects of desilication. *Catal Today* **2011,** *168* (1), 38-47.

65. Giudici, R.; Kouwenhoven, H. W.; Prins, R., Comparison of nitric and oxalic acid in the dealumination of mordenite. *Appl. Catal., A* **2000,** *203* (1), 101-110.

66. Van Geem, P. C.; Scholle, K. F. M. G. J.; Van Der Velden, G. P. M.; Veeman, W. S., Study of the transformation of small-port into large-port mordenite by magic angle spinning NMR and infrared spectroscopy. *J. Phys. Chem.* **1988,** *92* (6), 1585-1589.

67. Muller, M.; Harvey, G.; Prins, R., Comparison of the dealumination of zeolites beta, mordenite, ZSM-5 and ferrierite by thermal treatment, leaching with oxalic acid and treatment with SiCl4 by H-1, Si-29 and Al-27 MAS NMR. *Microporous and Mesoporous Mater.* **2000,** *34* (2), 135-147.

68. Silaghi, M.-C.; Chizallet, C.; Sauer, J.; Raybaud, P., Dealumination mechanisms of zeolites and extra-framework aluminum confinement. *J. Catal.* **2016,** *339*, 242-255.

69. Milina, M.; Mitchell, S.; Crivelli, P.; Cooke, D.; Pérez-Ramírez, J., Mesopore quality determines the lifetime of hierarchically structured zeolite catalysts. *Nat. Commun.* **2014,** *5*, 3922.

70. Reitmeier, S. J.; Gobin, O. C.; Jentys, A.; Lercher, J. A., Enhancement of sorption processes in the zeolite H-ZSM5 by postsynthetic surface modification. *Angew. Chem., Int. Ed.* **2009,** *48* (3), 533-538.

71. Monteiro, R.; Ania, C. O.; Rocha, J.; Carvalho, A. P.; Martins, A., Catalytic behavior of alkali-treated Pt/HMOR in n-hexane hydroisomerization. *Applied Catalysis A: General* **2014,** *476*, 148-157.

72. Leng, K.; Wang, Y.; Hou, C.; Lancelot, C.; Lamonier, C.; Rives, A.; Sun, Y., Enhancement of catalytic performance in the benzylation of benzene with benzyl alcohol over hierarchical mordenite. *Journal of Catalysis* **2013,** *306*, 100-108.

73. Nesterenko, N. S.; Thibault-Starzyk, F.; Montouillout, V.; Yuschenko, V. V.; Fernandez, C.; Gilson, J. P.; Fajula, F.; Ivanova, I. I., Accessibility of the acid sites in dealuminated small-port mordenites studied by FTIR of co-adsorbed alkylpyridines and CO. *Microporous Mesoporous Mater.* **2004,** *71* (1–3), 157-166.

74. Van De Runstraat, A.; Kamp, J. A.; Stobbelaar, P. J.; Van Grondelle, J.; Krijnen, S.; Van Santen, R. A., Kinetics of hydro-isomerization of n-hexane over platinum containing zeolites. *J. Catal.* **1997,** *171* (1), 77-84.

75. Haag, W. O.; Lago, R. M.; Weisz, P. B., Transport and reactivity of hydrocarbon molecules in a shape-selective zeolite. *Faraday Discuss. Chem. Soc.* **1981,** *72*, 317-330.

76. Groen, J. C.; Moulijn, J. A.; Perez-Ramirez, J., Desilication: on the controlled generation of mesoporosity in MFI zeolites. *Journal of Materials Chemistry* **2006,** *16* (22), 2121-2131.

77. Viswanadham, N.; Dixit, L.; Gupta, J. K.; Garg, M. O., Effect of acidity and porosity changes of dealuminated mordenites on n-hexane isomerization. *J. Mol. Catal. A Chem.* **2006,** *258* (1-2), 15-21.

78. Konnov, S. V.; Ivanova, I. I.; Ponomareva, O. A.; Zaikovskii, V. I., Hydroisomerization of n-alkanes over Pt-modified micro/mesoporous materials obtained by mordenite recrystallization. *Microporous Mesoporous Mater.* **2012,** *164*, 222-231.

79. Sazama, P.; Wichterlova, B.; Dedecek, J.; Tvaruzkova, Z.; Musilova, Z.; Palumbo, L.; Sklenak, S.; Gonsiorova, O., FTIR and 27Al MAS NMR analysis of the effect of framework Al- and Si-defects in micro- and micro-mesoporous H-ZSM-5 on conversion of methanol to hydrocarbons. *Microporous and Mesoporous Materials* **2011,** *143* (1), 87-96.

80. Brus, J.; Kobera, L.; Schoefberger, W.; Urbanová, M.; Klein, P.; Sazama, P.; Tabor, E.; Sklenak, S.; Fishchuk, A. V.; Dědeček, J., Structure of framework aluminum lewis sites and perturbed aluminum atoms in zeolites as determined by 27Al{1H} REDOR (3Q) MAS NMR spectroscopy and DFT/molecular mechanics. *Angew. Chem. Int. Ed.* **2015,** *54* (2), 541-545.

81. Sazama, P.; Wichterlova, B.; Sklenak, S.; Parvulescu, V. I.; Candu, N.; Sadovska, G.; Dedecek, J.; Klein, P.; Pashkova, V.; Stastny, P., Acid and redox activity of template-free Al-rich H-BEA* and Fe-BEA* zeolites. *J. Catal.* **2014,** *318* (0), 22-33.

82. Sazama, P.; Tabor, E.; Klein, P.; Wichterlova, B.; Sklenak, S.; Mokrzycki, L.; Pashkkova, V.; Ogura, M.; Dedecek, J., Al-rich beta zeolites. Distribution of Al atoms in the framework and related protonic and metal-ion species. *J. Catal.* **2016,** *333*, 102-114.

83. Van Bokhoven, J. A.; Koningsberger, D. C.; Kunkeler, P.; Van Bekkum, H.; Kentgens, A. P. M., Stepwise dealumination of zeolite Beta at specific T-sites observed with 27Al MAS and 27Al MQ MAS NMR. *Journal of the American Chemical Society* **2000,** *122* (51), 12842-12847.

84. Silaghi, M.-C.; Chizallet, C.; Sauer, J.; Raybaud, P., Dealumination mechanisms of zeolites and extra-framework aluminum confinement. *Journal of Catalysis* **2016,** *339*, 242-255.

85. Meier, W. M., The Crystal Structure Of Mordenite (Ptilolite). *Zeitschrift fur Kristallographie - New Crystal Structures* **1961,** *115* (5-6), 439-450.

86. Yang, S.; Yu, C.; Yu, L.; Miao, S.; Zou, M.; Jin, C.; Zhang, D.; Xu, L.; Huang, S., Bridging Dealumination and Desilication for the Synthesis of Hierarchical MFI Zeolites. *Angewandte Chemie International Edition* **2017,** *56* (41), 12553-12556.

87. Xie, B.; Song, J.; Ren, L.; Ji, Y.; Li, J.; Xiao, F. S., Organotemplate-free and fast route for synthesizing beta zeolite. *Chem. Mater.* **2008,** *20* (14), 4533-4535.

88. Shanjiao, K.; Tao, D.; Qiang, L.; Aijun, D.; Yanying, Z.; Huifang, P., Preparation and application of zeolite beta with super-low SiO2/Al2O3 ratio. *J. Porous Mater.* **2008,** *15* (2), 159-162.

89. Majano, G.; Delmotte, L.; Valtchev, V.; Mintova, S., Al-rich zeolite beta by seeding in the absence of organic template. *Chem. Mater.* **2009,** *21* (18), 4184-4191.

90. Kamimura, Y.; Chaikittisilp, W.; Itabashi, K.; Shimojima, A.; Okubo, T., Critical Factors in the Seed-Assisted Synthesis of Zeolite Beta and "Green Beta" from OSDA-Free Na+-Aluminosilicate Gels. *Chem. - Asian J.* **2010,** *5* (10), 2182-2191.

91. Kamimura, Y.; Tanahashi, S.; Itabashi, K.; Sugawara, A.; Wakihara, T.; Shimojima, A.; Okubo, T., Crystallization behavior of zeolite beta in OSDA-free, seed-assisted synthesis. *J. Phys. Chem. C* **2011,** *115* (3), 744-750.

92. Xie, B.; Zhang, H.; Yang, C.; Liu, S.; Ren, L.; Zhang, L.; Meng, X.; Yilmaz, B.; Muller, U.; Xiao, F.-S., Seed-directed synthesis of zeolites with enhanced performance in the absence of organic templates. *Chem. Commun. (Cambridge, U. K.)* **2011,** *47* (13), 3945-3947.

93. Itabashi, K.; Kamimura, Y.; Iyoki, K.; Shimojima, A.; Okubo, T., A Working Hypothesis for Broadening Framework Types of Zeolites in Seed-Assisted Synthesis without Organic Structure-Directing Agent. *J. Am. Chem. Soc.* **2012,** *134* (28), 11542-11549.

94. De Baerdemaeker, T.; Yilmaz, B.; Muller, U.; Feyen, M.; Xiao, F. S.; Zhang, W.; Tatsumi, T.; Gies, H.; Bao, X.; De Vos, D., Catalytic applications of OSDA-free Beta zeolite. *J. Catal.* **2013,** *308*, 73-81.

95. Zhang, H.; Xie, B.; Meng, X.; Mueller, U.; Yilmaz, B.; Feyen, M.; Maurer, S.; Gies, H.; Tatsumi, T.; Bao, X.; Zhang, W.; De Vos, D.; Xiao, F.-S., Rational synthesis of Beta zeolite with improved quality by decreasing crystallization temperature in organotemplate-free route. *Microporous Mesoporous Mater.* **2013,** *180*, 123-129.

96. Kubota, Y.; Itabashi, K.; Inagaki, S.; Nishita, Y.; Komatsu, R.; Tsuboi, Y.; Shinoda, S.; Okubo, T., Effective fabrication of catalysts from large-pore, multidimensional zeolites synthesized without using organic structure-directing agents. *Chem. Mater.* **2014,** *26* (2), 1250-1259.

97. Zheng, B.; Wan, Y.; Yang, W.; Ling, F.; Xie, H.; Fang, X.; Guo, H., Mechanism of seeding in hydrothermal synthesis of zeolite Beta with organic structure-directing agent-free gel. *Chin. J. Catal.* **2014,** *35* (11), 1800-1810.

98. Borade, R. B.; Clearfield, A., Synthesis of beta zeolite with high levels of tetrahedral aluminium. *Chem. Commun. (Cambridge, U. K.)* **1996,** (5), 625-626.

99. Muller, M.; Harvey, G.; Prins, R., Comparison of the dealumination of zeolites beta, mordenite, ZSM-5 and ferrierite by thermal treatment, leaching with oxalic acid and treatment with SiCl4 by H-1, Si-29 and Al-27 MAS NMR. *Microporous Mesoporous Mater.* **2000,** *34* (2), 135-147.

100. Huo, H.; Peng, L.; Gan, Z.; Grey, C. P., Solid-State MAS NMR Studies of Bronsted Acid Sites in Zeolite H-Mordenite. *J. Am. Chem. Soc.* **2012,** *134* (23), 9708-9720.

101. Strodel, P.; Neyman, K. M.; Knozinger, H.; Rosch, N., ACIDIC PROPERTIES OF AL , GA AND FE ISOMORPHOUSLY SUBSTITUTED ZEOLITES - DENSITY-FUNCTIONAL MODEL CLUSTER STUDY OF THE COMPLEXES WITH A PROBE CO MOLECULE. *Chem. Phys. Lett.* **1995,** *240* (5-6), 547-552.

102. Sigl, M.; Ernst, S.; Weitkamp, J.; Knozinger, H., Characterization of the acid properties of Al -, Ga - and Fe -HZSM-5 by low-temperature FTIR spectroscopy of adsorbed dihydrogen and ethylbenzene disproportionation. *Catal. Lett.* **1997,** *45* (1-2), 27-33.

103. Kiricsi, I.; Flego, C.; Pazzuconi, G.; Parker, W. O.; Millini, R.; Perego, C.; Bellussi, G., PROGRESS TOWARD UNDERSTANDING ZEOLITE-BETA ACIDITY - AN IR AND AL-27 NMR SPECTROSCOPIC STUDY. *J. Phys. Chem.* **1994,** *98* (17), 4627-4634.

104. Bourgeat-Lami, E.; Massiani, P.; Di Renzo, F.; Espiau, P.; Fajula, F.; Des Courieres, T., Study of the state of aluminium in zeolite-Î¿. *Appl. Catal.* **1991,** *72* (1), 139-152.

105. Beck, L. W.; Haw, J. F., Multinuclear NMR studies reveal a complex acid function for zeolite Beta. *J. Phys. Chem.* **1995,** *99* (4), 1076-1079.

106. De Menorval, L. C.; Buckermann, W.; Figueras, F.; Fajula, F., Influence of adsorbed molecules on the configuration of framework aluminum atoms in acidic zeolite-Î¿. A 27Al MAS NMR study. *J. Phys. Chem.* **1996,** *100* (2), 465-467.

107. Kunkeler, P. J.; Zuurdeeg, B. J.; Van Der Waal, J. C.; Van Bokhoven, J. A.; Koningsberger, D. C.; Van Bekkum, H., Zeolite Beta: The relationship between calcination procedure, aluminum configuration, and Lewis acidity. *J. Catal.* **1998,** *180* (2), 234-244.

108. Kuehl, G. H.; Timken, H. K. C., Acid sites in zeolite Beta: Effects of ammonium exchange and steaming. *Microporous Mesoporous Mater.* **2000,** *35-36*, 521-532.

109. Penzien, J.; Abraham, A.; Van Bokhoven, J. A.; Jentys, A.; Muller, T. E.; Sievers, C.; Lercher, J. A., Generation and Characterization of Well-Defined Zn2+ Lewis Acid Sites in Ion Exchanged Zeolite BEA. *J. Phys. Chem. B* **2004,** *108* (13), 4116-4126.

110. Anderson, J. R.; Chang, Y. F.; Western, R. J., Retained and desorbed products from reaction of 1-hexene over H-ZSM5 zeolite: Routes to coke precursors. *J. Catal.* **1989,** *118* (2), 466-482.

111. Bjørgen, M.; Bonino, F.; Kolboe, S.; Lillerud, K. P.; Zecchina, A.; Bordiga, S., Spectroscopic Evidence for a Persistent Benzenium Cation in Zeolite H-Beta. *J. Am. Chem. Soc.* **2003,** *125* (51), 15863-15868.

112. Ma, M.; Johnson, K. E., Carbocation formation by selected hydrocarbons in trimethylsulfonium bromide-AlCl3/AlBr3-HBr ambient temperature molten salts. *J. Am. Chem. Soc.* **1995,** *117* (5), 1508-1513.

113. Hemelsoet, K.; Qian, Q.; De Meyer, T.; De Wispelaere, K.; De Sterck, B.; Weckhuysen, B. M.; Waroquier, M.; Van Speybroeck, V., Identification of intermediates in zeolite-catalyzed reactions by in situ UV/Vis microspectroscopy and a complementary set of molecular simulations. *Chem. - Eur. J.* **2013,** *19* (49), 16595-16606.

114. Sazama, P.; Mokrzycki, L.; Wichterlova, B.; Vondrova, A.; Pilar, R.; Dedecek, J.; Sklenak, S.; Tabor, E., Unprecedented propane-SCR-NOx activity over template-free synthesized Al-rich Co-BEA* zeolite. *J. Catal.* **2015,** *332*, 201-211.

115. Chao, K. J.; Wu, H. C.; Leu, L. J., Hydroisomerization of light normal paraffins over series of platinum-loaded mordenite and beta catalysts. *Appl. Catal., A* **1996,** *143* (2), 223-243.

116. Yilmaz, B.; Muller, U.; Feyen, M.; Maurer, S.; Zhang, H.; Meng, X.; Xiao, F. S.; Bao, X.; Zhang, W.; Imai, H.; Yokoi, T.; Tatsumi, T.; Gies, H.; De Baerdemaeker, T.; De Vos, D., A new catalyst platform: Zeolite Beta from template-free synthesis. *Catal. Sci. Technol.* **2013,** *3* (10), 2580-2586.

117. Wang, N.; Zhang, M.; Yu, Y., Distribution of aluminum and its influence on the acid strength of Y zeolite. *Microporous Mesoporous Mater.* **2013,** *169*, 47-53.

118. Van Bokhoven, J. A.; Williams, B. A.; Ji, W.; Koningsberger, D. C.; Kung, H. H.; Miller, J. T., Observation of a compensation relation for monomolecular alkane cracking by zeolites: The dominant role of reactant sorption. *J. Catal.* **2004,** *224* (1), 50-59.

119. Zheng, S.; Heydenrych, H. R.; Jentys, A.; Lercher, J. A., Influence of Surface Modification on the Acid Site Distribution of HZSM-5. *The Journal of Physical Chemistry B* **2002,** *106* (37), 9552-9558.

120. Corma, A.; Fornés, V.; Forni, L.; Márquez, F.; Martínez-Triguero, J.; Moscotti, D., 2,6-Di-Tert-Butyl-Pyridine as a Probe Molecule to Measure External Acidity of Zeolites. *Journal of Catalysis* **1998,** *179* (2), 451-458.

121. Gounder, R.; Iglesia, E., Effects of partial confinement on the specificity of monomolecular alkane reactions for acid sites in side pockets of mordenite. *Angewandte Chemie - International Edition* **2010,** *49* (4), 808-811.

122. Bhan, A.; Iglesia, E., A link between reactivity and local structure in acid catalysis on zeolites. *Acc. Chem. Res.* **2008,** *41* (4), 559-567.

123. Gounder, R.; Iglesia, E., Catalytic consequences of spatial constraints and acid site location for monomolecular alkane activation on zeolites. *Journal of the American Chemical Society* **2009,** *131* (5), 1958-1971.

124. Eder, F.; Lercher, J. A., Alkane sorption in molecular sieves: The contribution of ordering, intermolecular interactions, and sorption on Brønsted acid sites. *Zeolites* **1997,** *18* (1), 75-81.

125. van de Runstraat, A.; van Grondelle, J.; van Santen, R. A., Microkinetics Modeling of the Hydroisomerization of n-Hexane. *Industrial & Engineering Chemistry Research* **1997,** *36* (8), 3116-3125.

126. Webb, E. B.; Grest, G. S.; Mondello, M., Intracrystalline Diffusion of Linear and Branched Alkanes in the Zeolites TON, EUO, and MFI. *The Journal of Physical Chemistry B* **1999,** *103* (24), 4949-4959.

127. Poursaeidesfahani, A.; de Lange, M. F.; Khodadadian, F.; Dubbeldam, D.; Rigutto, M.; Nair, N.; Vlugt, T. J. H., Product shape selectivity of MFI-type, MEL-type, and BEA-type zeolites in the catalytic hydroconversion of heptane. *Journal of Catalysis* **2017,** *353*, 54-62.

128. Fernandez, C.; Stan, I.; Gilson, J. P.; Thomas, K.; Vicente, A.; Bonilla, A.; Pérez-Ramírez, J., Hierarchical ZSM-5 zeolites in shape-selective xylene isomerization: Role of mesoporosity and acid site speciation. *Chem. Eur. J.* **2010,** *16* (21), 6224-6233.

129. Mitsuyoshi, D.; Kuroiwa, K.; Kataoka, Y.; Nakagawa, T.; Kosaka, M.; Nakamura, K.; Suganuma, S.; Araki, Y.; Katada, N., Shape selectivity in toluene disproportionation into

para-xylene generated by chemical vapor deposition of tetramethoxysilane on MFI zeolite catalyst. *Microporous and Mesoporous Materials* **2017,** *242*, 118-126.

130. Cheng, Y.-T.; Wang, Z.; Gilbert, C. J.; Fan, W.; Huber, G. W., Production of p-Xylene from Biomass by Catalytic Fast Pyrolysis Using ZSM-5 Catalysts with Reduced Pore Openings. *Angewandte Chemie International Edition* **2012,** *51* (44), 11097-11100.

131. Haw, J. F., Zeolite acid strength and reaction mechanisms in catalysis. *Physical Chemistry Chemical Physics* **2002,** *4* (22), 5431-5441.

132. Xu, T.; Kob, N.; Drago, R. S.; Nicholas, J. B.; Haw, J. F., A solid acid catalyst at the threshold of superacid strength: NMR, calorimetry, and density functional theory studies of silica-supported aluminum chloride. *Journal of the American Chemical Society* **1997,** *119* (50), 12231-12239.

133. Katada, N.; Suzuki, K.; Noda, T.; Miyatani, W.; Taniguchi, F.; Niwa, M., Correlation of the cracking activity with solid acidity and adsorption property on zeolites. *Applied Catalysis A: General* **2010,** *373* (1–2), 208-213.

134. Haag, W. O., Catalysis by Zeolites - Science and Technology. In *Studies in Surface Science and Catalysis*, 1994; Vol. 84, pp 1375-1394.

135. Kotrel, S.; Knözinger, H.; Gates, B. C., The Haag-Dessau mechanism of protolytic cracking of alkanes. *Microporous and Mesoporous Materials* **2000,** *35-36*, 11-20.

136. Narbeshuber, T. F.; Vinek, H.; Lercher, J. A., Monomolecular Conversion of Light Alkanes over H-ZSM-5. *Journal of Catalysis* **1995,** *157* (2), 388-395.

137. Wei, J., Adsorption and cracking of n-alkanes over ZSM-5: Negative activation energy of reaction. *Chemical Engineering Science* **1996,** *51* (11), 2995-2999.

138. Musselwhite, N.; Na, K.; Sabyrov, K.; Alayoglu, S.; Somorjai, G. A., Mesoporous Aluminosilicate Catalysts for the Selective Isomerization of n-Hexane: The Roles of Surface Acidity and Platinum Metal. *Journal of the American Chemical Society* **2015,** *137* (32), 10231-10237.

139. Knaeble, W.; Carr, R. T.; Iglesia, E., Mechanistic interpretation of the effects of acid strength on alkane isomerization turnover rates and selectivity. *Journal of Catalysis* **2014,** *319*, 283-296.

140. Ribeiro, F.; Marcilly, C.; Guisnet, M., Hydroisomerization of n-hexane on platinum zeolites: I. Kinetic study of the reaction on platinum/Y-zeolite catalysts: Influence of the platinum content. *Journal of Catalysis* **1982,** *78* (2), 267-274.

141. Stakheev, A. Y.; Shpiro, E. S.; Tkachenko, O. P.; Jaeger, N. I.; Schulz-Ekloff, G., Evidence for monatomic platinum species in H-ZSM-5 from FTIR spectroscopy of chemisorbed CO. *Journal of Catalysis* **1997,** *169* (1), 382-388.

142. Kubanek, P.; Schmidt, H. W.; Spliethoff, B.; Schüth, F., Parallel IR spectroscopic characterization of CO chemisorption on Pt loaded zeolites. *Microporous and Mesoporous Materials* **2005,** *77* (1), 89-96.

143. Zecevic, J.; Vanbutsele, G.; De Jong, K. P.; Martens, J. A., Nanoscale intimacy in bifunctional catalysts for selective conversion of hydrocarbons. *Nature* **2015,** *528* (7581), 245-254.

SYMBOLS

Å	ångström
Al_{EX}	extraframework aluminium
BEA	beta zeolite
BdB	Broekhoff-de Boer *t*-plot
C_{Al}	total concentration of aluminium in zeolite
C_B	concentration of Brønsted sites in zeolite
CD_3CN	d_3-acetonitrile
C_L	concentration of Lewis sites in zeolite
C_5	*n*-heptane
C_6	*n*-hexane
DTBPy	2,6-diterbuttylpyridine
FAU	faujasite zeolite
FER	ferrierite zeolite
GHSV	gas hourly space velocity
Pt^{0}, $Pt^{2+,}$ $Pt_n^{\delta+}$	forms of platinum in zeolite
RT	room temperature
S_{EXT}	external surface area
Si/Al	molar ratio of silicon and aluminium
TOF	turnover frequency
TOS	time-on-stream
USY	ultrastabilized Y zeolite
V_{MESO}	volume of mesopores in zeolite
V_{MI}	volume of micropores in zeolite
V_{tot}	total volume of pores in zeolite
WHSV	weight hourly space velocity
ZSM-5	Zeolite Socony Mobil–5
8-MR, 10-MR, 12MR	8, 10, 12 – membered rings of zeolite

PUBLISHING ACTIVITIES

- Skowerski, K.; Pastva, J.; Czarnocki, S. J.; Janoscova, J. *Org. Process Res. Dev.* **2015**, *19* (7), 872–877.

- Petr Sazama, Dalibor Kaucky, Jaroslava Moravkova, Radim Pilar, Petr Klein, Jana Pastvova, Edyta Tabor, Stepan Sklenak, Ivo Jakubec, Lukasz Mokrzycki; *Applied Catalysis A*: *General*, **2017,** 533, 28–37.

- Jana Pastvova, Dalibor Kaucky, Jaroslava Moravkova, Jiri Rathousky, Stepan Sklenak, Maryna Vorokhta, Libor Brabec, Radim Pilar, Ivo Jakubec, Edyta Tabor, Petr Klein, Petr Sazama; *ACS Catal.*, **2017**, 7, 5781–5795.

- Petr Sazama, Jana Pastvova, Dalibor Kaucky, Jaroslava Moravkova, Jiri Rathousky, Ivo Jakubec, Galina Sadovska; *Journal of Catalysis*, **2018**, 364, 262–270.

- Jana Pastvova, Radim Pilar, Jaroslava Moravkova, Dalibor Kaucky, Jiri Rathousky, Stepan Sklenak, Petr Sazama; *Applied Catalysis A, General*, **2018**, 562, 159–172.

- Petr Sazama, Jana Pastvova, Cristina Rizescu, Alina Tirsoaga, Vasile I. Parvulescu, Hermenegildo Garcia, Libor Kobera, Jürgen Seidel, Jiri Rathousky, Petr Klein, Ivan Jirka, Jaroslava Moravkova, Vaclav Blechta; *ACS Catal.*, **2018**, 8, 1779−1789.

- V době 21. 9. - 18. 12. 2015 jsem absolvovala stáž na univerzitě ve Freibergu v Německu (Institute of Physical Chemistry of the TU Bergakademie Freiberg). Pro tuto stáž mi bylo uděleno stipendium z DAAD. Garantem odborné stáže byl Dr. Jürgen Seidel.

- Patent CZ307177, 2018:
  J. Moravkova, D. Kaucky, J. Pastvova, P. Sazama: Katalyzátor pro hydroizomerizaci alkanů C4-C7, jeho příprava a použití (Catalyst for hydroizomerizaci alkanes C_4-C_7, its preparation and use)

CONFERENCE ABROAD

- ZMPC 2015 (International Symposium on Zeolite and Microporous Crystals); 28.6 - 2. 7. 2015; Sapporo, convention center, Japan; Preparation of 3D porous nanocarbon materials using USY zeolite as a hard template; autoři: **Jana Janošcová**, Petr Sazama, Jiří Rathouský, Libor Brabec, Galina Sádovská

- CIS6 (6th Czech-Italian-Spanish Conference on Molecular Sieves and Catalysis); 14. – 17. 6. 2015; Amantea, Itálie; Micro-mesoporous zeolites with tailored structure and distribution of active sites for hydroisomerization of linear C_5-C_6 alkanes; autoři: **Jana Janoscova**, Dalibor Kaucky, Edyta Tabor, Alena Vondrova, Jiri Rathousky, Petr Klein, Petr Sazama

- CIS6 (6th Czech-Italian-Spanish Conference on Molecular Sieves and Catalysis); 14. – 17. 6. 2015; Amantea, Itálie; Experimental overview of catalysts for HT-DEN$_2$O; autoři: G. Sadovská, P. Sazama, Z. Sobalík, E. Tabor, A. Vondrová, M. Bernauer, **J. Janošcová**

- CIS6 (6th Czech-Italian-Spanish Conference on Molecular Sieves and Catalysis); 14. – 17. 6. 2015; Amantea, Itálie; Modeling of high temperature DEN$_2$O laboratory scale reactor; autoři: M. Bernauer, G. Sádovská, P. Sazama, Z. Sobalík, E. Tabor, A. Vondrová**, J. Janošcová**, B. Bernauer

- CIS6 (6th Czech-Italian-Spanish Conference on Molecular Sieves and Catalysis); 14. – 17. 6. 2015; Amantea, Itálie; Enhancement of density of active sites and reaction rates for acid and redox catalysed reactions over zeolite catalysts; autoři: P. Sazama, **J. Janošcová**, L. Mokrzycki, V I. Parvulescu, E. Tabor, A. Vondrová, D. Kaucký, P. Klein

- ZMPC 2015 (International Symposium on Zeolite and Microporous Crystals); 28.6 - 2. 7. 2015; Sapporo, convention center, Japan; Unprecedented Acid and Redox Activity of Template-free Al-rich BEA Zeolite; autoři: Petr Sazama, Lukasz Mokrzycki, Blanka Wichterlová, Galina Sadovská, Vasile I. Parvulescu, Jiří Dědeček, **Jana Janošcová**, Petr Klein

- AMMM 6th Symposium (6th International Symposium on Advanced Micro and Mesoporous Materials); 6. - 9. 9. 2015; Burgas, Bulharsko; Hydroisomerization of Hexane over Micro-mesoporous Zeolites with Tailored structure and Distribution of Active Sites; autoři: Dalibor Kaucký**, Jana Janošcová**, Edyta Tabor, Jiří Rathouský, Petr Klein, Petr Sazama

- 18th IZC (International Zeolite Conference); 19. - 24. 6. 2016, Rio de Janeiro, Brazílie
  Název: Preparation of hierarchical mordenite zeolites with tailored texture and accessibility of acid sites
  Autoři: **Jana Pastvová,** Jaroslava Morávková, Dalibor Kaucký, Jiří Rathouský, Ivo Jakubec, Petr Sazama

- 18th IZC (International Zeolite Conference); 19. - 24. 6. 2016, Rio de Janeiro, Brazílie
  Název posteru: Hydroisomerization of n-hexane over micro-mesoporous zeolites
  Autoři: Dalibor Kaucký, Jaroslava Morávková, **Jana Pastvová (Janošcová),** Petr Klein, Edyta Tabor, Petr Sazama

- 18th IZC (International Zeolite Conference); 19. - 24. 6. 2016, Rio de Janeiro, Brazílie
  Název přednášky: Dramatic improvement of n-hexane hydroisomerization over zeolites with mutual close vicinity and high accessibility of strongly acidic centers
  Autoři: Jaroslava Morávková, Dalibor Kaucký, **Jana Pastvová**, Alena Vondrová, Edyta Tabor, Radim Pilař, Petr Sazama

- 13th European Congress on Catalysis (EUROPACAT 2017); 27. – 31. 8. 2017, Florencie, Itálie
  Název přednášky: Synthesis and structural analysis of micro-mesoporous mordenite with tailored structure and accessibility of active sites
  Autoři: **Jana Pastvová,** Dalibor Kaucký, Jaroslava Morávková, Jiří Rathouský, Ivo Jakubec, Petr Klein, Libor Brabec, Petr Sazama

- 13th European Congress on Catalysis (EUROPACAT 2017); 27. – 31. 8. 2017, Florencie, Itálie
  Název přednášky: Enhancement of hydroisomerization activity by high density of well-accessible acid sites in zeolites
  Autoři: Jaroslava Morávková, Dalibor Kaucký, **Jana Pastvová**, Edyta Tabor, Radim Pilař, Jiří Rathouský, Petr Klein, Ivo Jakubec, Petr Sazama

- 13th European Congress on Catalysis (EUROPACAT 2017); 27. – 31. 8. 2017, Florencie, Itálie
  Název přednášky: Hydro-isomerization of n-hexane over fluoridation-route prepared hierarchical micro-mesoporous zeolites
  Autoři: Dalibor Kaucký, **Jana Pastvová (Janošcová),** Petr Klein, Jaroslava Morávková, Jiří Rathouský, Edyta Tabor, Petr Sazama

- 10th International Conference on Environmental Catalysis & the 3rd International Symposium on Catalytic Science and Technology in Sustainable Energy and Environment; 22. – 26. 9. 2018, Tianjin China
  Název: Superior activity of Al-rich Pt/H-*BEA zeolites in hydroisomerization of *n*-hexane
  Autoři: Jaroslava Moravkova, Radim Pilar, Dalibor Kaucky, Jana Pastvova, Petr Sazama

- 8th Tokyo Conference on Advanced Catalytic Science and Technology (TOCAT8) and International Symposium on Zeolites and Microporous Crystals; 5. - 10. 8. 2018, Yokohama, Japan
  Název: Enhanced functionality of Al-rich zeolite beta catalysts in industrially relevant acid- and redox-catalysed reactions
  Autoři: Petr Sazama, Radim Pilar, Vasile Parvulescu, Galina Sadovska, Jaroslava Moravkova, Dalibor Kaucky, Jana Pastvova, Stepan Sklenak, Alena Vondrova

- 8th Tokyo Conference on Advanced Catalytic Science and Technology (TOCAT8) and International Symposium on Zeolites and Microporous Crystals; 5. - 10. 8. 2018, Yokohama, Japan
  Název: Controlled synthesis of the Al-rich zeolites of *BEA structure
  Autoři: Radim Pilar, Galina Sadovska, Dalibor Kaucky, Jana Pastvova, Petr Sazama

HOME CONFERENCE

- 12th Pannonian Symposium on Catalysis; 16. – 20. 9. 2014; zámek Třešť, ČR; Synthesis of 3D porous nanocarbon with defined structure; **Jana Janoscová**, Petr Sazama, Jiří Rathouský, Alena Vondrová, Petr Klein, Dalibor Kaucký

- 12th Pannonian Symposium on Catalysis; 16. – 20. 9. 2014; zámek Třešť, ČR; Enhancement of activity and selectivity in acid-catalyzed reactions by dealuminated hierarchical zeolites; autoři: Petr Sazama, Zdenek Sobalík, Petr Klein, Dalibor Kaucký, Milan Bernauer, Ivo Jakubec, Vasile Parvulescu, **Jana Janoscová**, Jiří Rathouský, Alena Vondrová

- Seminář studentů ÚFCH JH 2015; 4. – 6. 5. 2015; KC AV ČR Liblice; Synthesis of micro-mesoporous materials with defined structure; autoři: **J. Janoscová**;

- 47th Symposium on Catalysis; 2. – 4. 11. 2015, ÚFCH JH AV ČR, Praha
  Název přednášky: Hydroisomerization of hexane over micro-mesoporous MOR and ZSM-5 zeolites
  Autoři: Dalibor Kaucký, **Jana Pastvová (Janoscová),** Jiří Rathouský, Jaroslava Morávková, Petr Klein, Petr Sazama

- Seminář studentů ÚFCH JH 2016; 10. – 11. 5. 2016; KC AV ČR Liblice; Preparation of hierarchical mordenite zeolites; autoři: **Jana Pastvová**

- 48th Symposium on Catalysis; 7. – 9. 11. 2016, ÚFCH JH AV ČR, Praha
  Název přednášky: Synthesis of hierarchical mordenite by postsynthesis modification using flourination
  Autoři: **Jana Pastvová,** Dalibor Kaucký, Jaroslava Morávková, Jiří Rathouský, Petr Klein, Petr Sazama

- 48th Symposium on Catalysis; 7. – 9. 11. 2016, ÚFCH JH AV ČR, Praha
  Název přednášky: Enhanced hydroisomerization activity of non-interacting close acidic protons in Al-rich Pt/H-*BEA zeolite
  Autoři: Jaroslava Morávková, Dalibor Kaucký, Radim Pilař, Štěpán Sklenák, **Jana Pastvová**, Barbara Supronowicz, Lukasz Mokrzycki, Petr Klein, Edyta Tabor, Petr Sazama

- 49th Symposium on Catalysis; 6. – 7. 11. 2017, ÚFCH JH AV ČR, Praha
  Název přednášky: Micromesoporous mordenites with tailored structure and accessibility of active sites

autoři: **Jana Pastvová**, Jaroslava Morávková, Dalibor Kaucký, Jiří Rathouský, Ivo Jakubec, Petr Klein, Libor Brabec, Petr Sazama

- 49th Symposium on Catalysis; 6. – 7. 11. 2017, ÚFCH JH AV ČR, Praha
  Název přednášky: Hydroisomerization activity of hierarchical micromesoporous zeolites obtained by fluoridation-route
  autoři: Dalibor Kaucký, **Jana Pastvová**, Jaroslava Morávková, Edyta Tabor, Petr Sazama
- 49th Symposium on Catalysis; 6. – 7. 11. 2017, ÚFCH JH AV ČR, Praha
  Název přednášky: Hydroisomerization activity enhancement via high density of well-accessible acid sites in zeolites
  autoři: Jaroslava Morávková, Dalibor Kaucký, **Jana Pastvová**, Edyta Tabor, Radim Pilař, Jiří Rathouský, Petr Klein, Ivo Jakubec, Petr Sazama

SUPPLEMENT

Supplement 1 The yields of branched hexane isomers for hydroisomerization of *n*-hexane over microporous and micromesoporous Pt/H-zeolites.

ZSM-5/A

T (°C)	2,2-iso	2,3-iso	2-iso	3-iso	di-branch	mono-	all iso-
125	0.0	0.0	0.2	0.4	0.0	0.6	0.6
150	0.0	0.0	2.1	1.3	0.0	3.4	3.4
175	0.0	0.1	9.7	12.9	0.1	22.6	22.7
200	0.0	0.7	14.1	34.5	0.7	48.6	49.3
225	0.0	1.6	13.8	45.6	1.6	59.4	61.0

ZSM-5/A-meso-1

T (°C)	2,2-iso	2,3-iso	2-iso	3-iso	di-branch	mono-	all iso-
175	0.0	0.0	9.8	11.7	0.0	21.5	21.5
200	0.0	0.3	14.4	42.5	0.3	56.9	57.2
225	0.0	1.4	14.2	55.6	1.4	69.8	71.2

ZSM-5/A-meso-2

T (°C)	2,2-iso	2,3-iso	2-iso	3-iso	di-branch	mono-	all iso-
175	0.0	0.0	3.7	2.7	0.0	6.4	6.4
200	0.0	0.7	11.9	21.7	0.7	33.6	34.3
225	0.1	1.6	14.4	48.4	1.7	62.8	64.5

ZSM-5/B

T (°C)	2,2-iso	2,3-iso	2-iso	3-iso	di-branch	mono-	all iso-
150	0.0	0.0	0.2	0.2	0.0	0.4	0.4
175	0.0	0.0	4.2	3.0	0.0	7.2	7.2
200	0.0	0.4	9.4	25.4	0.4	34.8	35.2
225	0.0	1.3	11.5	47.6	1.3	59.1	60.4

ZSM-5/B-meso-1

T (°C)	2,2-iso	2,3-iso	2-iso	3-iso	di-branch	mono-	all iso-
200	0.0	0.5	15.4	45.7	0.5	61.1	61.6
225	0.0	1.7	15.2	57.3	1.7	72.5	74.2

ZSM-5/B-meso-2

T (°C)	2,2-iso	2,3-iso	2-iso	3-iso	di-branch	mono-	all iso-
125	0.0	0.0	0.0	0.0	0.0	0.0	0.0
150	0.0	0.0	0.2	0.2	0.0	0.4	0.4
175	0.0	0.0	2.3	1.5	0.0	3.8	3.8
200	0.0	0.1	11.8	15.7	0.1	27.5	27.6
225	0.0	1.6	14.6	46.9	1.6	61.5	63.1

ZSM-5/C

T (°C)	2,2-iso	2,3-iso	2-iso	3-iso	di-branch	mono-	all iso-
150	0.0	0.0	1.0	0.6	0.0	1.6	1.6
175	0.0	0.0	7.4	7.7	0.0	15.1	15.1
200	0.1	0.4	11.6	33.6	0.5	45.2	45.7
225	0.1	1.2	12.1	51.4	1.3	63.5	64.8

ZSM-5/C-meso-1

T (°C)	2,2-iso	2,3-iso	2-iso	3-iso	di-branch	mono-	all iso-
200	0.0	0.6	15.3	46.6	0.6	61.9	62.5
225	0.3	2.6	15.8	55.0	2.9	70.8	73.7

ZSM-5/D

T (°C)	2,2-iso	2,3-iso	2-iso	3-iso	di-branch	mono-	all iso-
150	0.0	0.0	0.0	0.0	0.0	0.0	0.0
175	0.0	0.0	1.7	1.7	0.0	3.4	3.4
200	0.0	0.0	8.7	7.7	0.0	16.4	16.4
225	0.0	0.4	13.1	31.1	0.4	44.2	44.6

ZSM-5/D-meso-1

T (°C)	2,2-iso	2,3-iso	2-iso	3-iso	di-branch	mono-	all iso-
125	0.0	0.0	0.0	0.0	0.0	0.0	0.0
150	0.0	0.0	1.2	0.4	0.0	1.6	1.6
175	0.0	0.0	9.1	9.0	0.0	18.1	18.1
200	0.0	0.3	15.4	36.3	0.3	51.7	52.0
225	0.0	0.9	14.1	50.3	0.9	64.4	65.3

MOR

T (°C)	2,2-iso	2,3-iso	2-iso	3-iso	di-branch	mono-	all iso-
175	0.0	0.0	1.1	1.1	0.0	2.2	2.2
200	0.0	1.4	4.7	4.4	1.4	9.1	10.5
225	0.7	2.8	8.9	18.6	3.5	27.5	31.0
250	1.4	4.3	11.8	34.7	5.7	46.5	52.2

MOR-meso-1

T (°C)	2,2-iso	2,3-iso	2-iso	3-iso	di-branch	mono-	all iso-
175	0.0	0.2	1.3	1.2	0.2	2.5	2.7
200	0.0	1.8	5.9	10.2	1.8	16.1	17.9
225	1.3	5.3	9.6	32.7	6.6	42.3	48.9
250	4.9	6.6	11.9	46.7	11.5	58.6	70.1

MOR-meso-2

T (°C)	2,2-iso	2,3-iso	2-iso	3-iso	di-branch	mono-	all iso-
175	0.0	0.0	1.1	0.9	0.0	2.0	2.0
200	0.0	1.1	6.7	9.3	1.1	16.0	17.1
225	1.3	4.5	8.2	33.8	5.8	42.0	47.8
250	5.2	6.8	12.1	44.1	12.0	56.2	68.2

BEA/A

T (°C)	2,2-iso	2,3-iso	2-iso	3-iso	di-branch	mono-	all iso-
150	0.0	0.0	1.2	0.9	0.0	2.1	2.1
175	0.7	1.4	10.4	18.6	2.1	29.0	31.1
200	5.6	4.0	13.0	39.0	9.6	52.0	61.6
225	16.1	6.6	13.4	43.8	22.7	57.2	79.9

BEA/B

T (°C)	2,2-iso	2,3-iso	2-iso	3-iso	di-branch	mono-	all iso-
150	0.0	0.0	0.3	0.2	0.0	0.5	0.5
175	0.0	0.0	2.5	1.8	0.0	4.3	4.3
200	0.7	0.9	8.4	19.3	1.6	27.7	29.3

USY

T (°C)	2,2-iso	2,3-iso	2-iso	3-iso	di-branch	mono-	all iso-
200	0.0	0.0	2.4	2.2	0.0	4.6	4.6
225	0.2	0.4	5.6	12.9	0.6	18.5	19.1
250	4.4	2.5	8.9	33.8	6.9	42.7	49.6
275	13.0	5.5	10.9	42.3	18.5	53.2	71.7